UNIVERSITÀ DEGLI STUDI DI NAPOLI "FEDERICO II"

FACOLTÀ D'INGEGNERIA

DOTTORATO DI RICERCA IN "INGEGNERIA AEROSPAZIALE, NAVALE E DELLA QUALITA'" – XXIV CICLO

SETTORE SCIENTIFICO DISCIPLINARE ING-IND 05: IMPIANTI E SISTEMI AEROSPAZIALI

METHODS AND SYSTEMS FOR ESTIMATION OF SHAPE-CHANGES APPLICABLE TO NAVIGATION AND CONTROL OF FLEXIBLE AEROSPACE VEHICLES

ING. VINCENZO ROSARIO BARANIELLO

TUTOR: CH.MO PROF. ING. MICHELE GRASSI
CO-TUTOR: ING. FEDERICO CORRARO

COORDINATORE: CH.MO PROF. ING. ANTONIO MOCCIA

Rem tene, verba sequentur
(Marco Porzio Catone)

(Grasp the words,
the subject will follow)

(Sii padrone del concetto,
le parole seguiranno)

Table of Contents

List of Figures

Acknowledgements

Abstract

Weight reduction has always represented an important factor in the design of aerospace structures and actually this tendency is increasing.

New materials, as composite materials, and new structural solutions have been proposed in recent years in order to reduce weights and improve the performances.

Lightweight structures and large wingspans induce an increment of deformations because of a detriment in the structural stiffness.

In this thesis the impact of structural flexibility on guidance, navigation and control disciplines will be discussed and some innovative solutions will be proposed in order to overcome limits of traditional rigid-body dynamic models.

The main effect of structural flexibility is an aircraft shape change in presence of maneuvers or gust.

Concerning shape changes estimation, in this work two innovative solutions are presented:

o extension of integrated navigation algorithms to flexible aircraft taking into account the flexible motions (shape changes);

o an algorithm for estimation of the shape changes alone, to be used, for example, in a load alleviation system.

A specific sensor setup has been associated to each one of these two proposals. In the case of integrated navigation, GPS and inertial sensors are used to estimate the rigid and flexible states (the word "rigid state" denotes at least position, speed and attitude, the word "flexible state" denotes some variables used to describe elastic motions), while for the determination of the shape changes alone, inertial sensors are associated with a video-based system.

This last point also represents an innovative solution.

The need for estimation of shape changes, independently by the rigid state, is justified by the consideration that for some classes of aircrafts, structural flexibility has not a big effect on navigation (estimation of navigation parameters is not strongly affected by the flexible state, essentially because of navigation sensors accuracy which is lower than the magnitude of elastic motions). The knowledge of shape changes is however required in load or gust alleviation techniques or for other applications, as for example the correction of the output provided by particular sensors installed onboard the aircraft.

In this work a simulation model of an aircraft, including elastic dynamic, will be presented, discussing the hypotheses on which it is based. This simulation model will be used to verify the performances of the proposed systems, but, above all, to analyze the main factors influencing the algorithms for shape changes estimation within gust or load control systems.

Acronyms

ADB	AeroDatabase
ADGPS	Attitude Derived GPS
CIRA	Italian Aerospace Research Center
DoF	Degree of Freedom
DOP	Dilution of Precision
DCM	Direct Cosine Matrix
ECEF	Earth Centered Earth Fixed
ECI	Earth Centered Inertial
EKF	Extended Kalman Filter
EoM	Equations of Motion
FEM	Finite Element Method
GDOP	Geometric Dilution of Precision
GN&C	Guidance, Navigation & Control
GPS	Global Positioning System
HALE	High Attitude Long Endurance
INS	Inertial Navigation Systems
ISR	Intelligence, Surveillance and Reconnaissance
JAXA	Japanese Aerospace Exploration Agency
MTI	Massachusetts Institute of Technology
r.f	Reference Frame
PRO.RA	National Program for Aerospace Researches
UAV	Unmanned Aerial Vehicle

Introduction

The weight reduction has always represented an important factor in the design of aerospace structures and actually this tendency is increasing.

New materials, as composite materials, and new structural solutions have been proposed in recent years in order to reduce weight and improve the performances.

Lightweight structures and large wingspans induce an increment of deformations because of a detriment in the structure stiffness.

In the aeronautical field, this issue is particularly relevant for the category of HALE vehicles (High Attitude Long Endurance Vehicle), which have lightweight structures and large wingspans [1].

An important example of high flexure wings was the NASA HELIOS aircraft, which during its last flight showed wing tip displacements of about 15 feet.

In general for HALE aircrafts, the ratio between wingtip displacements and semi wing span, assumes values comprised in the range 0.15 to 0.30 [2][3]. Considering that, for this class of aircrafts, semi-wings may typically reach an extension of 100 feet or more, wingtip displacements could reach the order of magnitude of several dozens of feet.

The potential missions of HALE vehicles are environmental/military observations and, more in general, communications (the aircrafts are used as relay stations).

HALE UAVs are mainly employed to provide near real time, high resolution intelligence, surveillance and reconnaissance imagery (ISR), to do that, these vehicles are equipped with dedicated sensors and instrumentations.

The great advantage offered by these vehicles, respect to satellites, is the possibility to make operations of maintenance, moreover they offer greater resolution due to their position nearer to the Earth surface.

They are generally electrically powered, thus they can continuously fly for months.

The program PRO.RA HAPD realized by the CIRA had the aim to analyze the potentialities and the design constraints of HALE aircrafts.
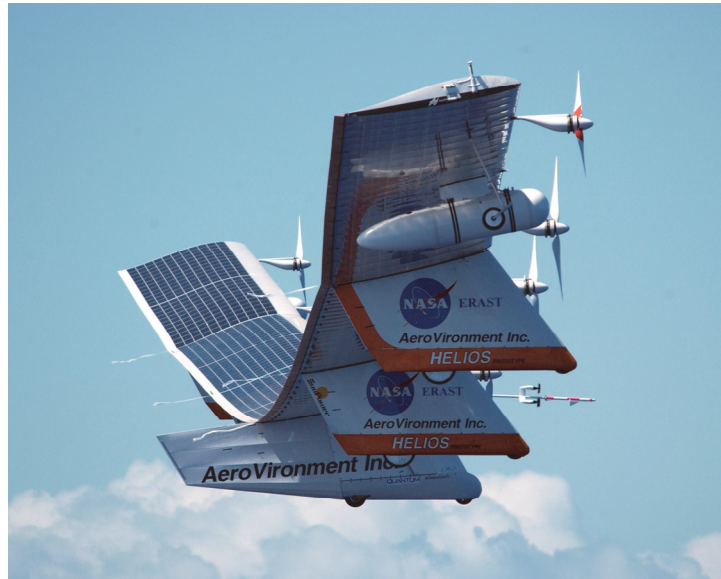
Figure I NASA Helios Aircraft

The problem of structural elasticity is not limited to HALE aircrafts, but concerns also new commercial aircrafts.

Figure II Boeing 787 wing deformation in several load conditions.

For modern wide-body commercial aircrafts, as for example the B787, the value of maximum wing flexure reported in literature is about 20 feet at the ultimate load, and 10 feet during normal flight operations [4].

In the next years, the concept of weight reduction will be more and more important, because it is associated to a more general concept of environmental friendly aircraft, which shall have limited noise emissions and fuel consumption.

The results of several studies, most of them realized by European aircraft manufacturers in collaboration with the research centers, on new configurations have shown that blended wing-

body tailless configuration is the better one [5] if associated with techniques of active control and load alleviation.

Some programs of the NASA also concern techniques and methods for current shape estimation in the field of structural monitoring and active control.

Both these modern control techniques benefit of the knowledge of the aircraft actual shape.

Figure III ACFA 2020 blended wing-body aircraft design

In the spatial environment, motions due to structural flexibility assume great importance due to the absence of air which can act as damper. The knowledge of the actual shape, essentially for control purposes, is important for systems requiring fine precision pointing as telecommunications satellites, which present large structural bending modes because of flexible arrays and fuel slosh [6].

The knowledge of the true structural shape is also required for applications in which two or more systems interact between them (spatial docking or in-flight refueling).

There are also some interesting scientific publications realized by MTI and JAXA scientists concerning shape change estimation for large space structures based on measurements provided by image or range sensors installed on robots, external to the space structure, and some accelerometers placed, instead, on it.

These solutions are justified by the assumption that, in next future, maintenance of space structures will be assigned to robots, which require exact knowledge of structure shape in order to interact with it [7][8].

For missiles and launchers, the problem of structural flexibility is directly connected with the design of the control system.

Using feedback signals provided by suitable sensors, a control system elaborates commands for the actuators of the control devices. The output of these sensors depends mainly by rigid motions but it is influenced also from the flexible ones (this is generally true for all types of flexible structures not only missiles or launchers).

The actuators of the control devices apply forces to the structure, feeding energy at different frequencies including the resonant ones.

Because of very low structural damping in missiles and launchers structures, it could happen that more energy is fed than dissipated [9].

This phenomenon is increased by aerodynamic forces because structural deflections increase aerodynamic loads, which cause new deflections. This is obviously an unstable mechanism, if not controlled.

In conclusion, for flexible structures, knowledge of shape changes is required essentially for four reasons:

1. health monitoring of the structure,

2. navigation and control purposes (Active Control Technologies),

3. determination of exact position and attitude of onboard sensors to increase the accuracy of their measurements,

4. flow control techniques. These techniques are becoming more integrated with flight control. They involve unsteady flow and flexible wings [6].

This thesis has been organized as follows. In the next chapter, the innovative contributions of this work will be briefly described. Further details will be presented in the other chapters.

In Chapter 1 an analysis of issues related to navigation of flexible aircrafts is provided. This chapter includes an overview of the *state of the art* navigation methods and systems for flexible, and "not-flexible", aircrafts, with an analysis of advantages and limitations of the proposed approaches. A method for estimation of navigation parameters and shape change is proposed, providing its detailed mathematical description and its fundamental equations. In Chapter 2 the problem of estimation of shape change is individually treated. In this case a specific solution is also proposed. In Chapter 3 a load alleviation system based on the setup and estimation algorithm presented in Chapter 2 is proposed. Finally in Chapter 4 some numerical and experimental results, related to systems proposed in previous chapters, will be analyzed.

Introduction to Innovative Aspects

The activities of this doctorate have concerned the analysis of the effects of structural flexibility on aircrafts Guidance, Navigation and Control.

The main consequence of flexibility is inapplicability of a rigid body model for flight mechanics analyses and for the design of navigation and control algorithms, because the typical 6 dof model is not more appropriate to describe the motion of flexible vehicles (above all for large vehicles).

The main difference between a flexible body model and rigid body one is the description of the elastic deflections of the structure, including more state variables.

In flexible structures, rigid and elastic motions could be frequencially coupled present, with the consequence that they cannot be considered separately within the analyses of flight dynamic and mechanic.

From the perspective of sensors (for example inertial sensors and GPS), a designer of a GN&C system shall take in account the influence of flexible motions on measurements, if their frequency content is included in the sensors band.

Furthermore, if inertial sensors and GPS antenna are separated by a certain distance, it could be not fixed but time variable, because of distortions due to flexibility. In the case of exact co-installation of both GPS antenna and inertial a lever arm could be generated because of the vehicle elastic behavior.

The exact knowledge of the distances between the sensors assumes great importance for systems like ADGPS based on several antennas and on carrier phase measurements or Gyro-free INS.

Concerning navigation algorithms, the most widely used system is generally composed by an IMU and a GPS, whose measurements are elaborated using a Kalman Filter.

In this field, *State of the Art* solutions generally neglect effects of shape changes on measurements and equations used in navigation algorithms.

A little number of proposals for navigation of flexible aircrafts has been proposed in recent years. These solutions handle anyway simplified models, considering: one-dimensional or two-dimensional flexible motions, rigid motions decoupled from the flexible ones, simple structural elements whose modal decomposition is analytically known.

A new approach to navigation algorithms for flexible aircrafts will be presented in this thesis. It includes estimation of both: vehicle rigid state (position, velocity and attitude) and elastic

state (specifically, modal decomposition will be used to describe shape changes), so that it can be used for flexible vehicles.

With this approach, the following innovative aspects respect to the current state of the art techniques will be proposed:

- a complete modeling of flexible motions into navigation algorithms;
- coupling between rigid motions and elastic ones;
- mode shapes derived by FEM analysis;
- 3-D modeling of elastic motions;

In particular, two formulations, with the relative sensors setup, will be proposed.

One formulation is focused on shape change estimation within a navigation system, while the other one is more focused only on shape changes estimation.

Estimation of shape changes in a three dimensional space, allows to use the proposed algorithm not only for navigation of aircrafts but also for other vehicles.

Within integrated navigation system, GPS is proposed to detect flexible deflections.

A video-based system has been proposed for estimation of shape changes. This choice is justified by the accuracy of GPS, which is suitable for estimation of shape changes only if used with differential corrections or for very high magnitude deflections.

This is another innovative aspect because videometry has been proposed and applied with success only for determination of deflections in civil structures. In the aerospace field, videometry is applied only for wind tunnel tests or for in-flight tests but using a post flight analysis of data.

The application of a video system provides great accuracy in estimation of shape changes and, moreover, it represents a more compact system respect to strain gauges and optical fibers, which have also a more complicated maintenance.

Unlike actual videometry techniques requiring complex patterns, the use of LEDs as markers makes easier the image processing, allowing the real-time application of this system.

These aspects will be treated in more details in chapters 1 and 2.

Regarding control applications, Active Control Systems benefit from knowledge of certain parameters related to flexibility.

As already affirmed, this class of control systems includes load alleviation and gust alleviation techniques. These techniques are nowadays applied mainly for the following purposes: i) improving the handling and flying quality, ii) reducing the risk of structural failure and iii) increasing the operational life of an aerospace vehicle [6].

Active control techniques are actually based on the feedback of acceleration measurements or of other parameters related to rigid motion, as the attitude. These parameters represent a synthetic information but limited to a certain area or a certain point of the aircraft.

In this work, a control algorithm have been designed and coupled with the proposed shape changes estimation algorithm, in order to evaluate its performances but, above all, to evaluate the design parameters of the estimation algorithm which mainly influence these performances. These algorithms are generally based on the application, as feedback, of measurements which refer to rigid motion too (as for example the attitude).

Some authors have proposed to use, as feedback, some parameters related to aircraft flexible state, but they don't suggest how these parameters can be really calculated.

The application of some parameters describing the shape changes as feedback should allow to act directly on the mode shapes more excited by the solicitations, improving the overall performances of the control law.

1   Navigation Issues for Flexible Aircrafts

In this chapter the main issues related to navigation of flexible aircrafts will be described. *State of the art* solutions for navigation of flexible aircrafts will be examined, analyzing their advantages and limitations.

In order to overcome some of the actual limitations, a new algorithm for navigation of flexible aircrafts will be proposed.

Its mathematical formulation (in terms of non-linear and linearized equations) will be provided together with some reminds, wherever needed, concerning the theoretical background.

Moreover, some unconventional navigation systems will be discussed. This overview has essentially two purposes, the first one is to highlight the sensitivity of some navigation systems to structural flexibility, because of their particular configurations; the second one is to provide some ideas for future activities.

1.1   *State of the Art and Description of the Proposed Method*

The works realized by the group of Prof. J.Wagner represent the *State of the Art* solutions for estimation of aircraft shape changes within an integrated navigation system.

In [11] and [12] advanced sensor fusion strategies are proposed, including detection of elastic motions for navigation purposes.

The peculiar aspects of these works are:

1) modal decomposition used to describe flexible motions;

2) the wing modelled as a beam: this structural element has analytical closed form solution for mode shapes and generalized coordinates.

   The positioning of accelerometers or gyros, used to detect flexible structural deflections, is presented as a natural consequence of mode shapes knowledge. Knowing the interesting mode shapes (with a model reduction method) it is possible to place the sensors in points having greater predisposition to sense elastic motions;

3) the sensor setup is composed by an IMU, several accelerometers or gyros, two radar units and several extensometers. The measurements of these systems are used within an Extended Kalman Filter. Some simplifications are considered. The main IMU (located at the aircraft centre of gravity, in the fuselage, and used only for navigation purposes) is not influenced by elastic structural motions (rigid and elastic motions are

decoupled). Another interpretation of this assumption is that the IMU is placed in a nodal point. This is another critical point because positions of nodal points are known with a certain degree of approximation and generally nodal points for different mode shapes could not correspond.

4) as additional degrees of freedom, consequence of structure flexibility, this papers consider only motions along one axis and rotations around an axis orthogonal to the plane containing this axis and the longitudinal axis.

Neglecting the presence of elastic motions at aircraft center of gravity is particularly critic for two reasons: i) fuselage could not be considerable as a rigid body, especially when they present high length to diameter ratio, ii) IMU accelerometers and gyros, having great accuracy, can sense elastic accelerations and angular speeds (also because elastic motions could have a frequency content in the bandwidth of IMU sensors).

In [13] only motions along Z axis (Body Reference frame) are considered, even if it is clearly indicated that this is a simplification, because as affirmed in the paper "*an array on a flexible aircraft wing can move in two directions: fore and aft, up and down, and rotation around pitch axis*". Moreover, in [13] the deformations of the structure are considered known from off-line calculations, so a method, for the on-line estimation of actual aircraft shape, is not proposed.

Concerning the modelling of the wing, for more complex design solution (for example joined wing configuration) the model of beam could not be used, thus mode shapes could not have an analytic formulation. The structural design and verification of these structural configurations are nowadays realised using FEM (Finite Element Method), which together with flight tests provides information about mode shapes.

In the light of the previous considerations, the purpose of the doctorate activities has been the development of a more general modelling of flexible phenomena for shape changes determination alone or within integrated navigation systems.

Concerning this last point, the proposed solution includes the following innovative aspects:

1) *coupling of elastic motions with the rigid ones.*

In the real world elastic motions have a frequencial content in the same band of the rigid ones. Under this assumption the entire aircraft structure can be consider as a flexible body, including also the fuselage. The placement of main navigation sensors, as the IMU, is not limited to nodal points, but extended to the entire structure of the aircraft, providing more flexibility.

2) *flexible motions include deflections along three orthogonal axes and rotations along them.*

This choice generalizes the navigation equations and allows extension of this method to more complex structures and aircrafts.

3) *Application of mode shapes derived from FEM analysis*

This allows the application of this method also to complex structures, for which an analytic description of modal decomposition is not available.

4) *GPS used to detect flexible deflections*

This choice reduces the number of sensors to be installed onboard the aircraft. The accuracy of the GPS (determined by the operative mode) influences the magnitude of flexible motions which can be estimated.

Another solution for detect flexible deflections, based on videometry, will be proposed in chapter 2.

Some aspects of current state of the art techniques are considered still valid.

In particular the modal decomposition will be still used to describe flexible motions and some accelerometers distributed along the aircrafts will be considered in association with GPS or videometry in order to detect flexible motions.

The application of modal decomposition is also justified by the application of EKF procedure which works on linearized systems.

1.2   Survey on Navigation Sensors Architectures

The navigation systems and their corresponding algorithms, mainly influenced by the effects of structural flexibility, are discussed in this paragraph.

Concerning this subject, the accuracy of the navigation systems involving several sensors installed on the aircraft is strongly influenced by structural flexibility, because the relative distances between the different sensors of the system have to be known with great accuracy. Examples of such a kind of navigation systems are: i) the gyro-free INS, ii) ADGPS and, iii) more in general, multiple IMUs.

These systems will be briefly described inside this paragraph, highlighting the aspects for which the exact knowledge of the real shape (and consequently of the distances between the sensors) is essential to ensure the desired accuracy.

As it will be explained in the followings, longer distances among the various sensors provide greater accuracy in the measurements, but longer distances imply a greater influence of

flexibility. This aspect is particularly critic for ADGPS associated with an algorithm using carrier phase differences.

1.2.1 Attitude Derived GPS

The estimation of attitude based on GPS measurements (or observables) involves essentially two different procedures:

i) *direct attitude estimation, using directly GPS observables*;
ii) *integration of GPS measurements with INS measurements* (using a suitable sensor fusion algorithm) to improve the overall accuracy.

Concerning direct attitude estimation, several architectures have been proposed, based on single or multiple GPS antennas. In this first case estimation of attitude uses velocity measurements and it is based on some restrictive assumptions [14] and it has several limitations [15].

For configurations with multiple antennas, several algorithms have ben proposed in the specialized literature. They essentially differ for the applications of the different GPS observables or measurements.

The term "*GPS observables*" denotes all the information computed from basic receiver channels measurements, for example: pseudo-time, code pseudo-range and phase observables [16].

In order to achieve an accurate attitude estimation from relatively short baselines on a moving platform, the C/A code carrier phase measurements have to be used among the GPS observables, because they are the most accurate measurements [17].

GPS carrier phase measurements are affected by integer carrier phase ambiguity. Carrier phase ambiguity represents the unknown number of whole wavelengths of the carrier signal contained in an unbroken set of measurements from a single satellite at a single receiver. Determination of position or attitude (in a multiple GPS-Antenna configuration) using these measurements cannot disregard the correct determination of integer ambiguity, in fact the kernel of the most part of the proposed technique for GPS-derived attitude is the resolution of integer ambiguity problem.

Carrier phase measurements are generally not directly used for attitude determination, but the single or double differences between them (differential observations).

An accurate, but at the same time simple, description of differential observations is provided in [18]. In this work it is provided a quantitative indication of the global error present respectively in carrier phase measurements, in single differences and finally in double differences: considering also the effect of synchronization between different GPS receivers.

The double differences technique allows reducing the orbital and atmospheric errors, satellite and receiver clock errors but, on the other hand, increases the influence of receiver noises. This technique derives from DGPS, where double differences are computed from measurements between two different receivers, one of them located at a ground station and representing the reference or master receiver (*differential base*) and another one installed onboard (*differential rover or slave receiver*).

In a configuration with multiple GPS antennas used for attitude derivation, both the master and slave receivers are installed onboard the moving platform. If a single receiver is used to decode signals from all the distributed antennas, master and slave receivers are coincident.

Various techniques have been proposed to solve integer ambiguity problem, in [17] a short review of these techniques is presented. Even if this paper dates at the end of nineties, the basic principles for resolution of integer ambiguity are still valid.

The application of aiding sensors as magnetometer or other inertial sensors speeds up the process of correct integer ambiguity determination. The solution time, which is an important parameter in real-time applications, depends essentially on the type of algorithm, which is applied. In "*fixed baseline*" algorithms, in which the known baselines lengths between master and slave antennas are used as constraints to reduce integer ambiguity search space, the process is faster than the iterative ones (essentially recursive least-square), and depends on baselines lengths (it increases with longer baselines). As will be shown later, longer baselines provide more accurate attitude estimation, thus a trade-off analysis is required. Structural flexibility is in fact another limiting factor in the length of the baseline, because of baseline length variations which introduce uncertainty in integer ambiguity estimation.

More recent techniques propose to solve simultaneously the attitude and carrier phase integer ambiguity resolution.

Several algorithms have been developed for estimating vehicle's attitude using a multi-Antenna GPS as measurement system and their positions as GPS measurements.

Some of them are based on the knowledge of antenna positions in the body reference frame, while other ones don't use this information.

The first type of method provides a solution which is less affected by multipath on a single antenna, because the attitude is calculated with a best fit over all antennas positions.

In order to achieve high accuracy positioning, carrier phase measurements have to be used, solving integer carrier phase ambiguities.

In [19] some experimental results, obtained using a system composed by four GPS antennas (an antenna is used for redundancy) and a least square method with carrier phase measurements, are reported. The distances between the antennas range from 7 to 10 meters and the receivers have an output rate of 10 Hz. The GPS based attitude is compared with the attitude estimated integrating Ring Laser Gyro measurements (offering a level of accuracy of 0.02° for pitch and roll, and 0.08° for yaw). The main conclusion of this paper is that attitude can estimated with an accuracy of about 0.05° to 0.11° (after removal of wing elastic motions), if the positions of GPS Antennas are known with an accuracy of 1 cm.

Other papers, concerning experimental results of GPS attitude estimation, report an accuracy on attitude up to one tenths of degree [20].

The second configuration, presented in this paragraph, concerns the integration of a multiple GPS antennas system with an IMU using a sensor fusion algorithm. The main purpose of this technique is to guarantee the observability of attitude error, independently from the aircraft's motion and the configuration of sensors.

Standard single GPS/IMU integration algorithms show some defeats in attitude determination. These algorithms are typically based on a sensor architecture, in which GPS and IMU are placed close together (in order to eliminate any lever arm effect). This assumption leads to a reduction of algorithm complexity, but on the other hand, this configuration does not guarantee the observability of the attitude error.

Observability of the Attitude error is provided by GPS measurements only if a lever arm is present between GPS and IMU. Moreover, even if IMU and GPS are installed with a distance between them, the observability of attitude error depends also by the maneuver of the aircraft; consequently it could not be guaranteed during all flight phases. To increase or provide attitude error observability, in standard single GPS/IMU integration algorithms, a magnetometer can be introduced.

Two kinds of integration algorithms between systems with multiple GPS antennas and IMU are treated in literature. The substantial difference between them, is in the application of different GPS observables as aiding measurements. Some authors propose the direct use of

GPS derived attitude, while other ones propose the use of pseudo-ranges with their derivatives or directly positions/speeds.

In [21] it is proposed a navigation system suitable for a bomb. The proposed architecture is composed by four GPS antennas (placed according to the scheme of Figure IV) and a tactical-grade IMU. As aiding measurements the author proposes the GPS pseudo-ranges/pseudo-ranges rates and the GPS derived attitude. The sensor fusion algorithm consists in a Kalman Filter, whose prediction step works at 10 Hz, while the update step works at 1 Hz. Some numerical results from several MonteCarlo simulations are presented; the values of rms and standard deviation related to attitude estimation error are reported in Table 1. In this paper the baselines length is 0.7 m, while GPS derived attitude have an accuracy of 0.5°.
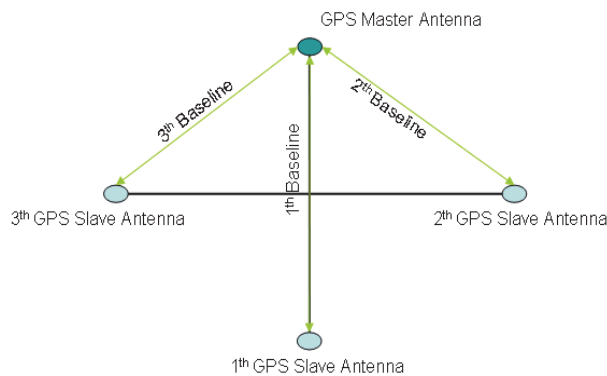
Figure IV GPS Antennas Configuration

	RMS	Standard deviation
Pitch (°)	1.3	0.6
Roll (°)	1.2	0.5
Heading (°)	1.0	0.5

Table 1 Attitude Error in Sang's paper (2004)

In [22] it is presented a comparison between four different GPS antennas configurations, using as parameter the accuracy of attitude estimation. This work concerns performances evaluation of different GPS Antennas configurations using a Kalman Filter sensor fusion algorithm. GPS pseudo-ranges and their derivatives are directly used as aiding measurements (there is not a calculation of GPS derived attitude).

The four configurations are in the order:

1.) a single antenna with a one meter lever arm;

2.) three antennas with one meter lever arm each one;

3.) a single antenna with a lever arm of 25 meters;

4.) three antennas with lever arms of 25 meters each one.

The indicated distances are referred to the IMU. With a single antenna, an increment of the lever arm length does not correspond to a greater accuracy in attitude estimation. The second configuration does not lead to a drastic change of the regular system performances because the lever arm has the same order of magnitude of GPS measurements error (about 1 meter). The last configuration leads to a notable accuracy improvement of the attitude estimation.

In [23] it is proposed to combine in a Kalman Filter the measurements provided by a triple GPS antenna system (with short baselines) with the output of a three single-axis gyroscopes (automotive grade), mounted in an orthogonal configuration. The purpose of this application is the realization of a low-cost AHRS for general aviation aircrafts. The high frequency gyroscopes measurements are used to provide attitude for navigation or control purposes, while GPS attitude, which has a lower data rate, is used for on-line calibration of gyroscopes. Experimental results have shown that the final accuracy of the algorithm is better than 0.2° for yaw, pitch and roll during normal operations, while the error reached, during GPS outages lasting 2 minutes, is less than 6°.

The important conclusion of this paper is that, using automotive gyroscopes (with a random walk factor of 180°/hr) it is possible to reach an accuracy comparable to tactical grade gyroscopes (random walk factor of 10°/hr), thanks to off-line and on-line calibration achieved with a multiple antenna GPS system. Moreover this application is based on an ultra-short baseline configuration, in which the three antennas are disposed in the vertices of an isosceles triangle, which sides have a length of 0.36 and 0.50 meters respectively. This configuration is suitable for reduction of wiring and flexural effects on GPS derived attitude measurements.

1.2.2 Multiple IMU

Using several IMUs arranged in a suitable configuration, it is also possible to obtain a better estimation of direct IMU measurements (i.e. angular speeds and linear accelerations), or of the derived navigation states variables (position and speed) as well as a more realistic statistical characterization of their noises.

In order to improve the accuracy of the measurements, inertial sensors shall be arranged in the same geometries proposed in [24] for FDI purposes. Specifically, skewed geometries are the better ones.

Skewed redundant IMUs are not so common in commerce, thus laboratories, interested in their application, generally assembly (starting from single IMUs) their devices in-house.

In literature several examples of systems for the reduction of sensor noise, based on redundancy of inertial sensors, have been reported. A combination of several inertial sensors

not only decreases measurement noise, but also offers a method to estimate their level during the processing [25]. This assumption is based on the consideration that we can obtain a better estimation of a certain quantity from n independent measurements, each one with variance σ_i^2 and weighting factor w_i. The standard deviation of this better estimation is given in Eq. (1).

$$\sigma_{\hat{x}} = \sqrt{\sum_{i=1}^{n} w_i^2 \sigma_i^2} = \frac{\sigma_x}{\sqrt{n}}$$

(1)

In [25] this theoretical noise reduction is experimentally verified for gyroscopes, integrating the measurements of four MEMS-IMUs gyros, each one with an estimated standard deviation of 0.0194 rad/sec. Standard deviation of the calculated angular speed is approximately reduced of 48% (0.0101 rad/sec) respect to the theoretical reduction of 50%.

In [26] it is investigated the integration of two independent IMUs, in order to increase measurements accuracy. The two single IMUs are arranged in a skewed configuration.

Their measurements can be combined according two approaches. The first one, defined "*approach in observation space*", consists in the generation of synthetic IMU measurements, i.e. starting from single IMUs outputs, generation of the measurements provided by an imaginary IMU placed at the center of a suitable reference frame (for example body reference frame for typical aeronautical applications), whose axes are aligned with the axes of the reference frame. The relative orientation between the two single IMUs must be known with high accuracy.
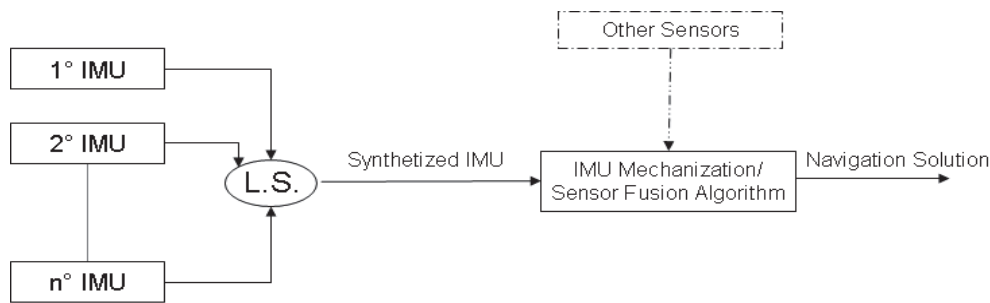
Figure V Synthetic IMU Mechanization approach for Navigation Solution

$$z = Cx + n$$

(2)

In the previous equation the column-vector z contains the measurements of n gyroscopes and m accelerometers (its length is $(n + m) \times 1$), C is a rectangular matrix transforming the measurements from body axes to actual sensor axes, x is a column vector containing angular speed and linear acceleration measured in the body reference frame (its length is 6 x 1) and finally n is an error term (noise, bias, etc..) with variance σ_n^2.

Because of measurements redundancy, we can obtain an estimation $\hat{x}$ of vector x, containing synthetic measurements (as previously defined) using a least-squares approach.

$$\hat{x} = C^* \tilde{z}$$

(3)

Where

$$C^* = \left(C^T \Sigma^{-1} C \right)^{-1} C^{-1} \Sigma^{-1}$$
$$\tilde{z} = z - n$$

(4)

In Eq. **(3)** and Eq.**(4)** C^* represents the pseudo-inverse of C matrix weighted with the covariance matrix Σ of IMU sensors, while $\tilde{z}$ is a column-vector containing raw measurements without error terms (these terms could be estimated through a calibration of the instruments).

The same approach is named in [25] "*Synthetic Mechanization Approach*".

Generally, sensors installed inside the single IMUs are similar each other, thus the inclusion of sensors covariance matrix in the estimation process does not introduce any further information, which could improve the quality of the estimation process.

The covariance of $\hat{x}$, $Cov(\hat{x})$, could be calculated as reported in Eq. (5), while the standard deviation σ_x as reported in Eq. (6).

$$Cov(\hat{x}) = \sigma_n^2 \cdot \left(C^T C \right)^{-1}$$

(5)

$$\sigma_x = \sigma_n \cdot GDOP$$

(6)

Where

$$GDOP = \sqrt{trace\left(C^T C \right)^{-1}}$$

(7)

The GDOP is an amplification factor of sensors noise, which depends on the number of sensors and their reciprocal arrangement. In [24] several systems, obtained varying the number and configuration of sensors, are analyzed and an indication of the relative GDOP is provided.

With this technique it is possible to obtain a realistic estimation of sensors noises and the covariance matrix for the synthetic IMU.

The second approach proposed in [25] and [26] is the "*geometrically-constrained mechanization*" or "*state-space approach*", according to the definition given in the first or in the second cited work.

This technique is based on the idea that direct estimation of navigation parameters can be accomplished using redundant measurements. To accomplish this task, we need to associate some mathematical expressions, representing geometrical constraints, to classical INS mechanization equations.
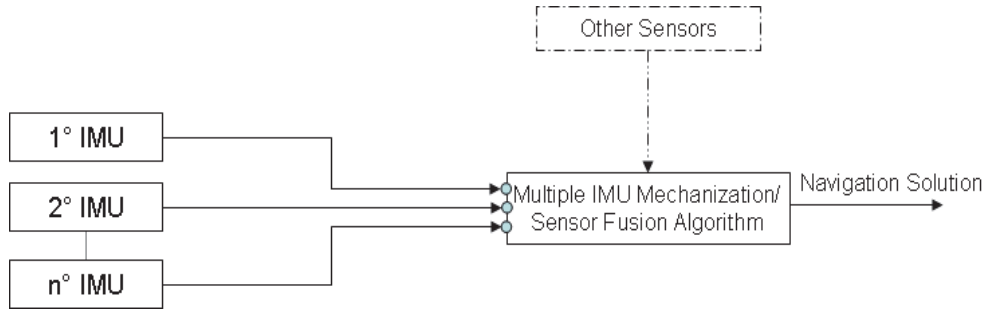
Figure VI. Geometrically-Constrained Mechanization

These further equations take in account that the relative orientation C_1^2 and the relative distance r_1^2 between the two single IMUs are fixed.

$$\dot{C}_1^2 = 0$$

$$\tag{8}$$

$$\dot{r}_1^2 = 0$$

$$\tag{9}$$

1.2.3 Gyro-free INS

The technology of MEMS accelerometers has reached high levels of miniaturization and accuracy, with extremely low costs; while the design and production of MEMS gyroscopes have not negligible costs. MEMS gyroscopes have, moreover, an accuracy significantly lower than RLG Gyroscope [27]. Accelerometers are more robust to work in environments with high accelerations, as for example the boost phase of gun-launched systems [28].

In the light of the previous considerations, some authors have proposed inertial navigation systems based only on accelerometers. Estimation algorithms for these systems have been also proposed. Generally these systems are named: *Gyro-Free IMU/INS*. In this paragraph, it will be provided a description of the physical concepts, on which these systems are based (essentially the measurement of angular speed and acceleration from linear accelerations). Some mechanization algorithms and an integration algorithm between GPS with Gyro-free INS will be also presented.

A generic i^{th} single-axis accelerometer positioned in a point at a distance λ_i from the vehicle's center of gravity (in the following, the position of a generic accelerometer in the inertial

reference frame will be indicated with the symbol R^I) is subject to different forms of acceleration. Under the assumption of rigid body; the total acceleration is sum of several contributions: inertial ($\ddot{R}^I$), tangential and centripetal acceleration [Eq.**(10)**].

$$f_i = \ddot{R}^I + \dot{\omega} \times \lambda_i + \omega \times (\omega \times \lambda_i) - g$$

(10)

Where $\dot{\omega}$ and ω represent respectively the angular acceleration and the angular speed of the body r.f. respect to the inertial r.f..

Placing several accelerometers in a suitable configuration and summating their outputs, it is possible to obtain a direct relation between angular acceleration $\dot{\omega}$ and measured linear accelerations f_i.

For a 6 d.o.f rigid body at least six single-axis accelerometers are necessary to solve the problem of angular and translational acceleration estimation, because we have six unknown quantities: the three angular speed and the three linear accelerations of body center of gravity respect to an inertial reference frame.

The application of this technique is based on the implicit assumption that accelerometers are able to sense tangential accelerations ($\dot{\omega} \times \lambda$).

MEMS accelerometers have typically a noise density of $0.05 \dfrac{mg}{\sqrt{Hz}}$ [29], which corresponds to a standard deviation of about $0.25 mg$ (with a 30 Hz bandwidth). Considering a lever arm length of 10 cm, in order to guarantee the compactness of the solution, the order of magnitude of the measurable angular acceleration is $0.018 \dfrac{rad}{\sec^2}$, this value is compatible with typical UAV maneuvers. As it is clear from the previous description, a longer lever-arm improves the quality of the measurement because it causes an improvement of the signal to noise ratio (considering a constant angular acceleration, the tangential acceleration increases with the lever-arm), however longer lever-arms introduce flexural motions, which have to be taken in account in the model.

In [30] the six single-axis accelerometers are placed on a cube face centers (whose sides have a generic length equal to *2 x l*) with the sensing direction along faces' diagonals.

The relation between angular acceleration $\dot{\omega}$, c.g. linear acceleration $\ddot{R}^I$ and linear accelerations measured by the six accelerometers f_i is reported in Eq. (11).

$$\begin{bmatrix} \dot{\omega} \\ \ddot{R}^I \end{bmatrix} = \frac{1}{2} \cdot \begin{bmatrix} \left(1/l\right) \cdot S \\ T \end{bmatrix} \begin{bmatrix} f_1 \\ f_2 \\ f_3 \\ f_4 \\ f_5 \\ f_6 \end{bmatrix} + \frac{1}{l} \cdot \begin{bmatrix} 0 \\ 0 \\ 0 \\ \omega_y \omega_z \\ \omega_x \omega_z \\ \omega_y \omega_x \end{bmatrix}$$

(11)

In Eq. (11) gravitational acceleration is neglected, anyway it is a simple further contribution to sum. Considering that this contribution consists in the components of gravitational acceleration along accelerometers sensing directions, pitch and roll angles appear explicitly in Eq. (11) .

For the proposed configuration, matrices S and T assume the values indicated in Eq. (12) and Eq. (13). In general the condition number of matrix $\left[\left(1/l\right) \cdot S \quad T \right]^T$ influences the quality of the solution and it could determine or strongly influence the accelerometers' configuration.

$$S = \frac{1}{\sqrt{2}} \cdot \begin{bmatrix} 1 & -1 & 0 & 0 & 1 & -1 \\ -1 & 0 & 1 & -1 & 0 & -1 \\ 0 & 1 & -1 & -1 & 1 & 0 \end{bmatrix}$$

(12)

$$T = \frac{1}{\sqrt{2}} \cdot \begin{bmatrix} 1 & 1 & 0 & 0 & -1 & -1 \\ 1 & 0 & 1 & -1 & 0 & 1 \\ 0 & 1 & 1 & 1 & 1 & 0 \end{bmatrix}$$

(13)
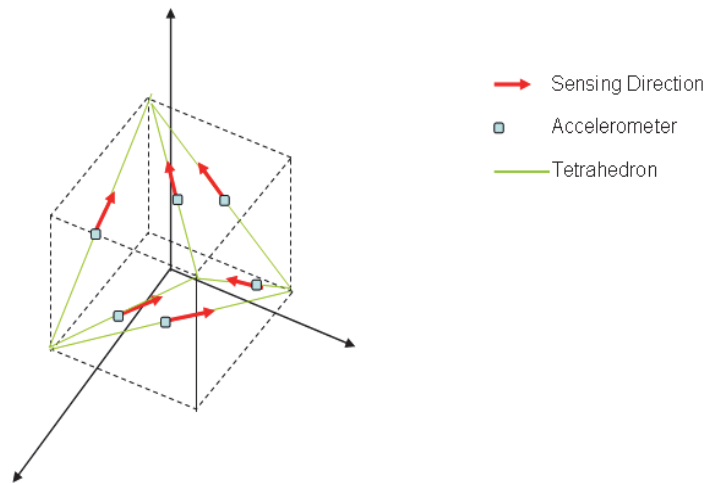
Figure VII. Chen's Accelerometers Configuration

To obtain angular speed through integration of angular acceleration, it is necessary to have an initial value for the angular speed $\omega(0)$. Initialization of Gyro-free INS is particularly critic for initial angular speed determination: there is a sign–indetermination problem. Using the accelerometers it is possible to estimate only angular acceleration (which will be null in a

static initial situation) or quadratic combinations of angular speeds (centripetal acceleration terms).

As we will see later, the sign-indetermination problem is also present in algorithms which directly estimate angular speed.

Linear and angular accelerations, calculated according to Eq. (11), represent the input variables for perturbed navigation equations to estimate position, speed and attitude.

The great problem of this configuration is its error growth. Considering a white noise error on angular accelerations, the corresponding errors on angular speed and angular position grow up proportionally to the time (for the angular speed) and proportionally to the square of the time (for the angular position), causing a divergence of position and speed estimation according to the following laws: t^4 and t^3.

These errors are extremely higher than typical medium-accuracy gyro based systems, thus it is necessary to integrate a Gyro-free IMU with an aiding measurement device as for example GPS.

In [33] the problem of accelerometers' configuration is treated with more details. The condition number of matrix $H = \left[\left(\frac{1}{l} \right) \cdot S \quad T \right]^T$ influences the quality of the solution and so it could determine or strongly influence the accelerometers' configuration. In particular, symmetric arrangements provide better performances according to an optimality criterion. Several terms are considered as indices to quantify the optimality of the configuration [Eq. (14)].

$$GDOP(H) = \sqrt{Tr(H^T \cdot H)^{-1}}$$
$$\dot{\omega}DOP(H) = \sqrt{Tr\left(\left[\left(\frac{1}{l} \right) \cdot S \right]^T \cdot \left[\left(\frac{1}{l} \right) \cdot S \right] \right)^{-1}}$$
$$aDOP(H) = \sqrt{Tr(T^T \cdot T)^{-1}}$$

$$\text{(14)}$$

An optimal configuration for all three axes, is achievable using *Platonic* solids, which are obtained joining together regular polygons.

Platonic solids, interesting for this application, are the tetrahedron, the octahedron, the icosahedrons, the cube and finally the dodecahedron. Considering that Platonic solids can be inscribed into spheres, the Gyro-free IMU is also named *Inertial Reference Sphere* (ISR) [33]. The orientation of accelerometers could be defined in order to form a Hamiltonian path from graph theory.

Several configurations have been analyzed in terms of the optimality indices [Eq. (14)], concluding that configurations built according to Hamiltonian path are not suitable or have lower performances than Chen's configuration [30], reproduced in Figure VII. Several configurations with nine accelerometers have been also considered.

The introduction of a tri-axial accelerometer at the center of a cubic configuration leads to an improvement of estimation performances of linear accelerations but there are no advantages in terms of angular acceleration estimation because of the absence of lever-arm for this further tri-axial accelerometer. Eq. (11) can be also interpreted in terms of the theory of dynamical systems [34]. It represents a dynamical system in which the state variable is the angular rate ω, the output variable is the linear acceleration $\ddot{R}$ and obviously the input is represented by accelerometers measurements f. Furthermore estimation of angular acceleration is decoupled from the estimation of linear acceleration

$$\dot{\omega} = g(\omega, f)$$
$$\ddot{R} = h(\omega, f)$$

(15)

The first expression in Eq. (15) g is a differential (generally non-linear) equation, while the second one h is an algebraic equation. For the particular configuration reproduced in Figure VII, the differential equation for $\dot{\omega}$ is linear because the geometry of the sensing directions cancels the symmetric part of the angular motion (centripetal acceleration).

Configurations with nine single-axis accelerometers have been also presented [37].

The configuration with six accelerometers is highly dependent on correct location and orientation of sensors in order to remove centripetal accelerations (caused by angular speed) from accelerometers measurements, in fact angular acceleration expression is an algebraic expression. Configurations with nine accelerometers offer a greater degree of accuracy.
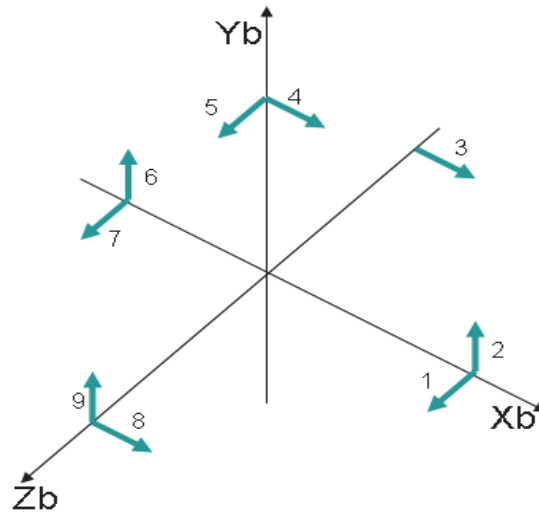
Figure VIII. Qin's Accelerometers Configuration

Integration algorithms between Gyro-free INS and GPS measurements have been also presented [38]. Both Linear and Non-Linear perturbated mechanization equations are analyzed. Linear equations can be used during very short flight phases or between two GPS measurements updates. Non-Linear error model shall be used in presence of GPS blockage and consequently in absence of corrections, because of very rapid divergence of estimation error. The linear analysis of the different error terms shows that the influence of accelerometers noise is inversely proportional to cube edges length, while the effect of configuration error depends on the dynamic of maneuver. The estimation of configuration errors depends also on the dynamic of motion: in some flight phases their observability could not be guaranteed. Location errors are insensitive to cube size, while orientation error depends on the inverse of cube edge length. The simulations, in which the linear model has been tested, show that the error of position estimation (north, east and height) is bounded and inferior to ±0.15 m.

Some other works, concerning modelling and simulation of a Gyro-free INS, have been realized by Edwan [35][36]. The proposed system is composed by several single IMUs arranged in a redundant configuration. The use of single IMUs represents an enormous advantage. The systems based on Gyro-free INS composed by single-axis accelerometers arranged in suitable configuration, have to be realized entirely by users. Edwan's system allows using commercial MEMS IMUs arranged in a suitable configuration. The disadvantages of this proposal consist in the influence of uncertainties in sensors placement in each IMU (which have to be treated as a statistic data, provided in IMU datasheet, but that cannot be controlled or eliminated) on final Gyro-free INS performances and the obviously

increase in weight and size of the final product. Two innovative aspects are covered in [36]: the resolution of the initial angular speed estimation problem and the formalization of an algorithm (under simplified assumptions on sensor error modelization) for direct estimation of angular speed. This second aspect is a key point, because, as shown previously, a great limitation of Gyro-free INS is the rapid divergence of the estimation error due to integration of angular acceleration in order to obtain the angular speed. The proposed system is composed by four accelerometers triads, arranged according to the scheme in Figure IX and a low-cost Gyroscope triad, used as aiding measurement in a Kalman filter sensor fusion algorithm.

The application of a Gyroscope triad does not make superfluous the installation of several IMUs, because the angular speed is directly provided by gyroscopes. The integration of multiple IMUs arranged in a proper configuration with gyroscopes (even if low quality ones) improves the quality of angular speed estimation, in terms of noise reduction and quicker response to rapid manoeuvres thanks to estimation of angular acceleration. Furthermore, the four IMUs, composing this system, contain each one a triad of gyroscopes; offer a triple redundancy of gyroscopes measurements.

Using a Gyroscope triad the sign-indetermination on angular speed is solved and a quicker convergence to correct solution is shown by the proposed sensor fusion algorithm.
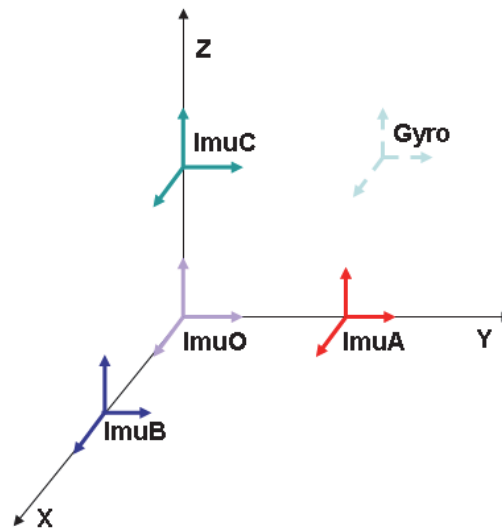
Figure IX. Edwan IMU Configuration

The assumptions, on which the proposed sensor fusion algorithm is based, are: *1.)* distributed IMUs perfectly aligned with reference axes; *2.)* perfect calibration of sensors (the proposed algorithm does not estimate sensor error parameters).

The state vector directly includes rotation changes along three orthogonal axes, while the input vector consists in the discrete angular speed change, obtained multiplying angular accelerations (estimated with linear accelerometers) for the sample time.

The aiding measurement vector is composed by directly measured angular change (obtained multiplying gyroscope angular speed for sample time) and angular speed quadratic terms (obtained from linear accelerometers measurements) multiplied for the square of the sample time.

To take into account that aiding measurements noises and input measurements noises are correlated, because angular accelerations and quadratic angular speeds are estimated both from accelerometers' outputs, a cross-covariance term is introduced in the calculation of the Kalman gain.

The results of simulations effectively show a shorter transient than simple Gyro-free INS and a lower noise respect to simple gyroscope measurements.

As previously stated, in this model only a white noise term is considered as error source on accelerometer and gyroscope measurements (biases are not included), thus it is not possible to evaluate the advantage in direct estimation of angular speed using angular speed quadratic terms and gyroscope measurements.

In [35] a dynamic model for estimation of angular motion is presented. A sensor configuration composed by four IMUs is analyzed; unlike the previous work a tri-axial gyroscope is not included. An Extended Kalman Filter is implemented to estimate angular motion, but in this case the state vector is composed by angular acceleration, angular speed and biases of angular acceleration and angular speed quadratic terms (twelve scalar components), while the measurement vector is composed by twelve outputs: angular accelerations and angular speed quadratic terms estimated from accelerometer measurements. To model the angular acceleration evolution a Wiener process is applied, while the biases are modeled as random processes driven by white noises.

The peculiarity of this work is that there is a direct estimation of biases on tangential acceleration (proportional to angular acceleration) and on centripetal acceleration (proportional to square of angular speed). Obviously these biases are fictitious, because they do not correspond to a direct measured quantity, but this model allows a reduction of the number of unknown quantities. In fact for a system of twelve accelerometers, the number of biases, to be estimated, should be equal to twelve, while with this model technique this number reduces to nine.

1.3   Mathematical Formulation of Navigation equations for Flexible Aircrafts

1.3.1   The Extended Kalman Filter

The purpose of this paragraph is to provide a short description of the basic Kalman Filter theory.

For a more detailed description the reader can consult the specialized literature [39].

A generic non-linear dynamic system can be expressed as:

$$\begin{cases} \dot{x} = f(x, u) \\ y = h(x) \end{cases}$$

(16)

The Kalman Filter is an extremely effective and versatile procedure for combining noisy outputs from several sensors, in order to estimate the state of a system with uncertain dynamics.

Two quantities assume great importance within the Kalman filter procedure:

- *Estimated State Vector*: which includes the variables of interest (i.e. speed and position), error model variables with no intrinsic interest but need to the estimation process (i.e. sensors biases).

- *Covariance Matrix*: a measure of estimation uncertainty. The covariance matrix is time propagated using the Riccati Equation.

The Kalman Filter theory can be applied to linear systems. For a non-linear system [Eq.**(16)**] a modified algorithm exists, which is applicable to the relative linearized system. This algorithm is named *Extended Kalman Filter*.

In the EKF, the linearization point (also defined as *equilibrium point*) is on-line estimated; this consideration differentiates the EKF from a Linearized Kalman Filter, in which an off-line calculated equilibrium point (trajectory) is used.

The kernel of the EKF is the Kalman Gain *K*, which is a weighting matrix for combining sensor measurements *y* data with a prior estimates of both the output $\hat{y}(-)$ and the state vector $\hat{x}(-)$ to obtain a new estimate of the state vector $\hat{x}(+)$.

$$\hat{x}(+) = \hat{x}(-) + K \cdot [y - \hat{y}]$$

(17)

Starting from an initial estimate of the state vector $\hat{x}(0)$ (initial condition) with a certain initial covariance matrix $P(0)$, the EKF (and also the KF) algorithm can be divided into two phases: **Prediction and Correction**. These two phases could have different cycle times,

because aiding measurements y could be provided at a different data rate, generally lower, than the cycle time of the prediction phase.

The operations included in the Prediction phase are described by Eq.**(18)** and Eq.**(19)**:

$$\hat{x}_k(-) = \hat{x}_{k-1}(+) + \int_{t_{k-1}}^{t_k} f(x,t)dt$$

(18)

$$P_k(-) = \Psi_k P_{k-1}(+) \Psi_k^T + Q_{k-1}$$

(19)

In the prediction phase, the filter propagates the state vector and the covariance matrix.

In **(19)** Ψ_k represents the discrete form of the linearized dynamic matrix.

The steps included in the Correction phase are reported and Eq. **(20)**, **(21)** and **(22)**:

$$K_k = P_k(-)H_k^T \left[H_k P_k(-)H_k^T + R_k \right]^{-1}$$

(20)

$$\hat{x}_k(+) = \hat{x}_k(-) + K_k \left[y_k - \hat{y}_k \right]^{-1}$$

(21)

$$P_k(+) = P_k(-) + K_k H_k P_k(-)$$

(22)

Within the correction phase, the filter calculates the Kalman gain and updates the state vector and the covariance matrix with the corrections obtained using the new measurement and the Kalman gain.

1.3.2 The Modal Decomposition

Within this dissertation, the analysis and modeling of structural deflections are based principally on the assumption of the modal decomposition validity.

Within modal decomposition theory, elastic deflections can be expressed in terms of linear combination of products between space functions $\Phi_i(x, y, z)$ (*mode shapes*) and time functions $\eta_i(t)$(*generalized coordinates*). With this assumption a generic elastic displacement d_e can be expressed, as in Eq. **(23)** and more compactly as in **(24)**, assuming that a *n*-order model is required to describe the structural dynamics.

$$d_e = \begin{bmatrix} \phi_{1x} & \phi_{2x} & \phi_{3x}.. & .. & \phi_{nx} \\ \phi_{1y} & \phi_{2y} & \phi_{3y}.. & .. & \phi_{ny} \\ \phi_{1z} & \phi_{2z} & \phi_{3z}.. & .. & \phi_{nz} \end{bmatrix} \begin{bmatrix} \eta_1 \\ . \\ . \\ \eta_n \end{bmatrix}$$

<div align="right">**(23)**</div>

$$d_e = \Phi \eta$$

<div align="right">**(24)**</div>

Similarly, it is possible to define elastic rotations as product between a space dependent function $H(x,y,z)$ and the same time function $\eta_i(t)$ Eq.

(25):

$$\theta_e = \begin{bmatrix} H_{j1x} & H_{j2x} & H_{j3x\,..} & .. & H_{jnx} \\ H_{j1y} & H_{j2y} & H_{j3y\,..} & .. & H_{jny} \\ H_{j1z} & H_{j2z} & H_{j3z\,..} & .. & H_{jnz} \end{bmatrix} \begin{bmatrix} \eta_1 \\ . \\ . \\ . \\ \eta_n \end{bmatrix}$$

<div align="right">**(25)**</div>

$$\theta_e = H \eta$$

<div align="right">**(26)**</div>

The instantaneous distance between a generic point and a certain reference point (in our analysis, the aircraft's center of gravity) is considered as a sum of a rigid fixed distance d_r and an elastic term d_e (which is time variable) Eq. **(27)**.

$$r = d_r + \Phi \eta$$

<div align="right">**(27)**</div>

The first and second derivatives of Eq. **(27)** represent respectively the velocity [Eq. **(28)**] and the acceleration [Eq. **(29)**] of a generic point, and depend only by elastic motions.

$$\dot{r} = \Phi \dot{\eta}$$

<div align="right">**(28)**</div>

$$\ddot{r} = \Phi \ddot{\eta}$$

<div align="right">**(29)**</div>

1.3.3 Algorithm Implementation: State Variables and Dynamic Equations

The intent of this paragraph is to define the key equations used in the proposed navigation algorithm. These equations will be used to derive the final perturbation form used within the EKF.

The state vector is composed by the following variables:

- $r_{cg}^t \rightarrow$ Position of aircraft's center of gravity in North-East-Down reference frame (NED or Tangent r.f. indicated with a t as superscript or subscript).

- $\dot{r}^{t}_{cg}$ → Speed of aircraft's center of gravity in NED r.f.

- η → Generalized Coordinates

- $\dot{\eta}$ → Generalized Coordinates Derivatives

- C^{b}_{t} → Rotation Matrix from Ned r.f to Body r.f.

- b_{sens} → Accelerometers and Gyroscopes Biases

We need to derive some expressions for the following variables:

- linear acceleration $\ddot{r}^{t}_{cg}$ of aircraft's center of gravity in the NED r.f.,

- second derivative $\ddot{\eta}$ of the generalized coordinates,

- the derivative $\dot{C}^{b}_{t}$ of rotation matrix,

Furthermore, we need a dynamic model for the time variation of sensors biases.

In the following equations, the superscript will indicate the reference frame in which the vector is expressed:

- *e* indicates the ECEF reference frame (blue in Figure X),

- *t* indicates the tangent (NED) reference frame (red in Figure X),

- *i* indicates the ECI reference frame (brown in Figure X),

- *b* indicates the Body reference frame (brown in Figure X),

- *s* indicates the Sensor reference frame (light blue in Figure X).

When notation with multiple subscripts is used, their meaning is the following: the first subscript from the right indicates the reference frame the specific measurement belongs to, the second one represents the reference frame respect to which this measurement is evaluated.

For example:

ω^{e}_{ie} is the angular speed of the ECEF reference frame (*e* is the first subscript index from the right) with respect to ECI reference frame (*i* is the second subscript index from the right) expressed in the ECEF reference frame (*e* is the superscript).

To obtain the equations describing the dynamic of the state variables, we start considering the expression of the linear acceleration, respect to the ECI reference frame, sensed by a generic point *j* on the aircraft structure including effects of flexibility.
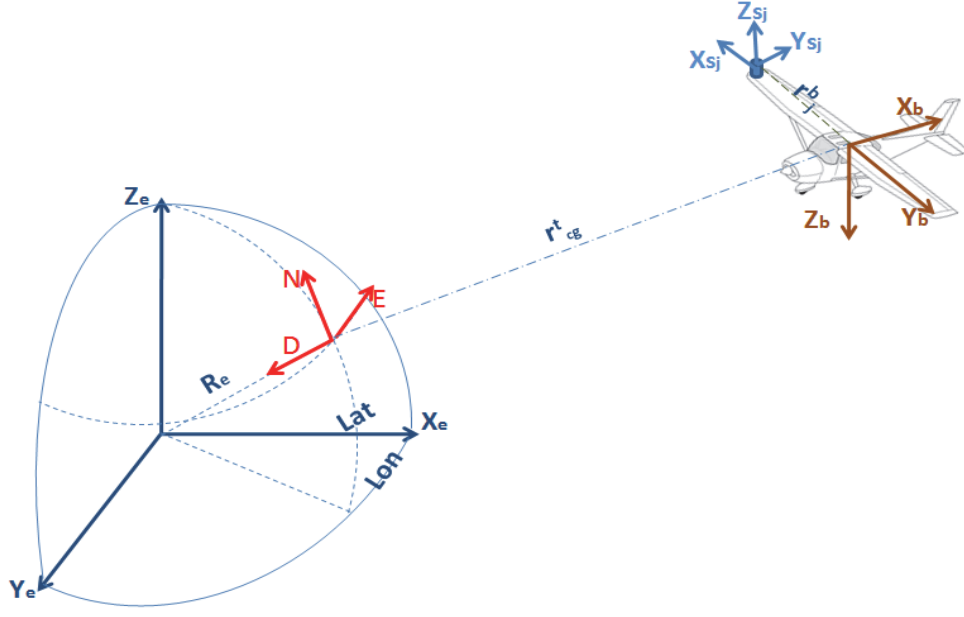
Figure X Reference Frames

$$\ddot{R}_j^i = C_e^i \omega_{ie}^e \times \left(\omega_{ie}^e \times R_e^e \right) + C_t^i \left[\omega_{it}^t \times \left(\omega_{it}^t \times r_{cg}^t \right) + 2\omega_{it}^t \times \dot{r}_{cg}^t + \left(\dot{\omega}_{it}^t \times r_{cg}^t \right) + \ddot{r}_{cg}^t \right] +$$
$$+ C_b^i \left[\omega_{ib}^b \times \left(\omega_{ib}^b \times r_j^b \right) + 2\omega_{ib}^b \times \dot{r}_j^b + \left(\dot{\omega}_{ib}^b \times r_j^b \right) + \ddot{r}_j^b \right]$$

(30)

Eq. **(30)** has been derived under the hypotheses of negligible Earth's angular acceleration and constant Earth's radius.

An accelerometer installed at a generic point j provides a measure of the linear acceleration $\ddot{R}_j^i$ summed with contribution of the gravitational force:

$$\ddot{R}_j^i - G^i = C_{sj}^i f_j^s$$

(31)

In Eq. **(31)** f_j^s represents the output of the jth accelerometer expressed in the Sensor reference frame, while C_{sj}^i represents the rotation matrix between j^{th} Sensor reference frame (subscript) and ECI reference frame (superscript). The rotation matrix can also be expressed as combination of rotation matrices, each one representing a single rotation between two specific reference frames.

$$C_{sj}^i = C_t^i C_b^t C_{sj}^b$$

(32)

$C_{sj}{}^b$ represents the rotation matrix between the jth sensor reference frame and the Body reference frame. It can be expressed as combination of the generalized coordinates.

We consider $C_{sj}{}^b$ as a little perturbation of the initial rotation matrix $R_{sj}{}^b$ due to the mounting angles. This perturbation is determined only by elastic angles θ_e, defined in Eq. **(33)**.

$$C_{sj}^b = \left[\begin{bmatrix} 1 & 0 & 0 \\ 0 & 1 & 0 \\ 0 & 0 & 1 \end{bmatrix} - \begin{bmatrix} 0 & -\theta_{3j} & \theta_{2j} \\ \theta_{3j} & 0 & -\theta_{1j} \\ -\theta_{2j} & \theta_{1j} & 0 \end{bmatrix} \right] R_{sj}^b$$

(33)

In Eq. **(34)** all the contributions to the gravitational term G^t will be expressed, we can identify a true gravitational acceleration and other centripetal accelerations due to Earth's rotation around the ECI reference frame.

$$G^t = g^t + C_e^t \left[\omega_{ie}^e \times \left(\omega_{ie}^e \times R_e^e \right) \right] - \omega_{it}^t \times \left(\omega_{it}^t \times r_{cg}^t \right) - C_b^t \left[\omega_{it}^b \times \left(\omega_{it}^b \times r_j^b \right) \right]$$

(34)

Considering that:

$$\omega_{it}^t = \omega_{ie}^t$$

(35)

$$\omega_{ib}^b = \omega_{it}^b + \omega_{tb}^b = \omega_{ie}^b + \omega_{tb}^b$$

(36)

Substituting Eq. **(30)** in Eq. **(31)**, holding Eq. **(27)**, **(28)** and **(29)** we have an expression for the linear acceleration of the aircraft center of gravity.

$$\ddot{r}_{cg}^t = C_{sj}^t f_j^s + g^t - C_b^t \left[\begin{matrix} \omega_{tb}^b \times \left(\omega_{tb}^b \times d_j^b \right) + \\ + \dot{\omega}_{tb}^b \times d_j^b \end{matrix} \right] - C_b^t \left[\begin{matrix} \Phi_j \ddot{\eta} + \omega_{tb}^b \times \left(\omega_{tb}^b \times \Phi_j \eta \right) + \\ + 2\omega_{ib}^b \times \Phi_j \dot{\eta} + \left(\dot{\omega}_{ib}^b \times \Phi_j \eta \right) + \\ + \omega_{tb}^b \times \left(\omega_{tb}^b \times \Phi_j \eta \right) \end{matrix} \right] - \left[2\omega_{it}^t \times \dot{r}_{cg}^t \right]$$

(37)

Accelerometer Measurement	Rigid Lever Arm Effect (Centripetal and Angular Accelerations)	Flexible Lever Arm Contribution	Coriolis Acceleration

Eq.**(37)** has been derived starting from the measurements of an accelerometer installed at a generic j^{th} point along the aircraft structure. The linear acceleration of the aircraft center of gravity can be equally estimated considering the measurements provided by the main IMU used for navigation purposes.

Measurements and any other physical quantity referring to main IMU are indicated with superscript "*" and the rigid lever arm with the symbol λ^{*b}.

$$\ddot{r}_{cg}^{t} = C_{sj}^{t} f_{j}^{s*} + g^{t} - C_{b}^{t} \begin{bmatrix} \omega_{tb}^{b} \times \left(\omega_{tb}^{b} \times \lambda^{*b} \right) + \\ + \dot{\omega}_{tb}^{b} \times \lambda^{*b} \end{bmatrix} - C_{b}^{t} \begin{bmatrix} \Phi^{*}\ddot{\eta} + \omega_{tb}^{b} \times \left(\omega_{tb}^{b} \times \Phi^{*}\eta \right) + \\ + 2\omega_{ib}^{b} \times \Phi^{*}\dot{\eta} + \left(\dot{\omega}_{ib}^{b} \times \Phi^{*}\eta \right) + \\ + \omega_{tb}^{b} \times \left(\omega_{tb}^{b} \times \Phi^{*}\eta \right) \end{bmatrix} - \begin{bmatrix} 2\omega_{it}^{t} \times \dot{r}_{cg}^{t} \end{bmatrix}$$

(38)

We will express cross product as a matrix multiplication.

$$a \times b = \overline{a}b$$

(39)

In the special case of a cross product between the angular speed and another generic vector, we use the following symbol $\overline{\Omega}$.

Considering the IMU accelerometer as a reference measurement, one can subtract Eq. **(38)** from Eq.**(37)**, in this way the unknown $\ddot{r}_{cg}^{t}$ disappears and one could be able to evaluate generalized coordinates second derivatives.

$$0 = \left(f_{j}^{\,t} - f^{*t} \right) - C_{b}^{t} \begin{bmatrix} \left[\left(\omega_{tb}^{b} \cdot d_{j}^{\,b} \right) \omega_{tb}^{b} - \left| \omega_{tb}^{b} \right|^{2} \left(d_{j}^{\,b} - \lambda^{*b} \right) - \left(\omega_{tb}^{b} \cdot \lambda^{*b} \right) \omega_{tb}^{b} \right] + \\ + \left(\Phi_{j} - \Phi^{*} \right) \ddot{\eta} + \\ + \left[\left(\omega_{tb}^{b} \cdot \Phi_{j}\eta \right) \omega_{tb}^{b} - \left| \omega_{tb}^{b} \right|^{2} \left(\Phi_{j} - \Phi^{*} \right) \eta - \left(\omega_{tb}^{b} \cdot \Phi^{*}\eta \right) \omega_{tb}^{b} \right] + \\ + 2\omega_{ib}^{b} \times \left[\left(\Phi_{j} - \Phi^{*} \right) \dot{\eta} \right] \end{bmatrix}$$

(40)

Installing *m* triaxial distributed accelerometers, in principle we should be able to estimate up to *3xm* generalized coordinates, however, as it will be explained later, the number of generalized coordinates which can be estimated depends on the position of the accelerometers (distributed and main IMU) and on the desired accuracy of the estimation.

We can do a further arrangement of Eq. **(40)** using properties of dot and cross products.

$$0 = \left(f_{j}^{\,t} - f^{*t} \right) - C_{b}^{t} \begin{Bmatrix} \left[\left(\omega_{tb}^{b} \left(\omega_{tb}^{b} \right)^{T} \right) - \left| \omega_{tb}^{b} \right|^{2} U \right] \left(d_{j}^{\,b} - \lambda^{*b} \right) + \\ + \left(\Phi_{j} - \Phi^{*} \right) \ddot{\eta} + \\ + \left[\left(\omega_{tb}^{b} \left(\omega_{tb}^{b} \right)^{T} \right) - \left| \omega_{tb}^{b} \right|^{2} U \right] \left(\Phi_{j} - \Phi^{*} \right) \eta + \\ + 2\overline{\Omega}_{ib}^{b} \left(\Phi_{j} - \Phi^{*} \right) \dot{\eta} \end{Bmatrix}$$

(41)

Solving Eq. **(41)** respect to $\ddot{\eta}$:

$$\left(\Phi_j - \Phi^*\right)\ddot{\eta} = +\left(C_{sj}^b f_j^{\ s} - C_{IMU}^b f^{*s}\right) - \left\{\begin{array}{l}\left[\left(\omega_{tb}^b\left(\omega_{tb}^b\right)^T\right) - \left|\omega_{tb}^b\right|^2 U\right]\left(d_j^{\ b} - \lambda^{*b}\right) + \\ \left[\left(\omega_{tb}^b\left(\omega_{tb}^b\right)^T\right) - \left|\omega_{tb}^b\right|^2 U\right]\left(\Phi_j - \Phi^*\right)\eta + \\ + 2\overline{\Omega}_{ib}^b\left(\Phi_j - \Phi^*\right)\dot{\eta}\end{array}\right\}$$

$$(42)$$

Defining the following matrices it is possible to write Eq.(42), considered for all *m* spatially distributed accelerometers in a matrix form.

$$f^s = \begin{bmatrix} f_1^s \\ f_2^s \\ . \\ f_{m-1}^s \end{bmatrix}_{3(m-1)x1} \quad C_s^b = \begin{bmatrix} C_{s1}^b & 0 & 0 \\ 0 & .. & 0 \\ 0 & 0 & C_{sm-1}^b \end{bmatrix}_{3(m-1)x3(m-1)} \quad F^{*s} = \begin{bmatrix} C_{s*}^b f^{*s} \\ C_{s*}^b f^{*s} \\ .. \\ C_{s*}^b f^{*s} \end{bmatrix}_{3(m-1)x1} \quad D^{*s} = \begin{bmatrix} \lambda^{*b} \\ \lambda^{*b} \\ .. \\ \lambda^{*b} \end{bmatrix}_{3(m-1)x1}$$

$$\Gamma^* = \begin{bmatrix} \Phi^* \\ \Phi^* \\ . \\ \Phi^* \end{bmatrix}_{3(m-1)x3(m-1)} \quad \Xi_{is*}^b = \begin{bmatrix} \left[\overline{\Omega}_{is*}^b\right]_{3x3} & 0 & 0 \\ 0 & .. & 0 \\ 0 & 0 & \left[\overline{\Omega}_{is*}^b\right]_{3x3} \end{bmatrix}_{3(m-1)x3(m-1)}$$

$$\Delta_{tb}^b = \begin{bmatrix} \left[\left(\omega_{tb}^b\left(\omega_{tb}^b\right)^T\right) - Tr\left(\omega_{tb}^b\left(\omega_{tb}^b\right)^T\right)\right]_{3x3} & 0 & 0 \\ 0 & .. & 0 \\ 0 & 0 & \left[\left(\omega_{tb}^b\left(\omega_{tb}^b\right)^T\right) - Tr\left(\omega_{tb}^b\left(\omega_{tb}^b\right)^T\right)\right]_{3x3} \end{bmatrix}_{3(m-1)x3(m-1)}$$

$$(43)$$

In the previous matrices it has been considered that $\left|\omega_{ts*}^b\right|^2 = Tr\left(\omega_{ts*}^b\left(\omega_{ts*}^b\right)^T\right)$

Definitively we have.

$$\ddot{\eta} = \left(\Phi - \Gamma^*\right)^{-1}\left[+\left(C_s^b f^s - F^{*b}\right) - \left\{\begin{array}{l}\left[\Delta_{tb}^b\right]\left(d^b - D^{*b}\right) + \\ \left[\Delta_{tb}^b\right]\left(\Phi - \Gamma^*\right)\eta + \\ + 2\Xi_{is*}^b\left(\Phi - \Gamma^*\right)\dot{\eta}\end{array}\right\}\right]$$

$$(44)$$

Eq. (44) is in a non linear form: it includes products between the state variables and input variables (acceleration measurements (m vectorial quantities) and body angular speed measured by a set of three single axis gyroscopes).

Now we need an expression for $\ddot{r}_{cg}^{t}$, in which $\ddot{\eta}$ doesn't compare; this is possible substituting Eq. **(44)** in Eq. **(38)**.

$$\ddot{r}_{cg}^{t} = f^{*t} + g^{t} - C_{b}^{t} \begin{bmatrix} \omega_{tb}^{b} \times \left(\omega_{tb}^{b} \times \lambda^{*b}\right) + \omega_{tb}^{b} \times \left(\omega_{tb}^{b} \times \Phi^{*}\eta\right) + 2\omega_{ib}^{b} \times \Phi^{*}\dot{\eta} + \\ + \Phi^{*}\left(\Phi - \Gamma^{*}\right)^{-1}\left(C_{s}^{b} f^{s} - F^{*b}\right) + \\ -\Phi^{*}\left(\Phi - \Gamma^{*}\right)^{-1}\begin{Bmatrix} \left[\Delta_{tb}^{b}\right]\left(d^{b} - D^{*b}\right) + \\ \left[\Delta_{tb}^{b}\right]\left(\Phi - \Gamma^{*}\right)\eta + \\ + 2\overline{\Xi}_{ib}^{b}\left(\Phi - \Gamma^{*}\right)\dot{\eta} \end{Bmatrix} \end{bmatrix} - \left[2\omega_{it}^{t} \times \dot{r}_{cg}^{t}\right]$$

(45)

We can develop some terms which appear in Eq. **(45)**.

$$\ddot{r}_{cg}^{t} = f^{*t} + g^{t} - C_{b}^{t} \begin{bmatrix} \left[\left(\omega_{tb}^{b}\left(\omega_{tb}^{b}\right)^{T}\right) - Tr\left(\omega_{tb}^{b}\left(\omega_{tb}^{b}\right)^{T}\right)\right]\lambda^{*b} + \left[\left(\omega_{tb}^{b}\left(\omega_{tb}^{b}\right)^{T}\right) - Tr\left(\omega_{tb}^{b}\left(\omega_{tb}^{b}\right)^{T}\right)\right]\Phi^{*}\eta + 2\overline{\Omega}_{ib}^{b}\Phi^{*}\dot{\eta} + \\ + \Phi^{*}\left(\Phi - \Gamma^{*}\right)^{-1}\left(C_{s}^{b} f^{s} - F^{*b}\right) + \\ -\Phi^{*}\left(\Phi - \Gamma^{*}\right)^{-1}\begin{Bmatrix} \left[\Delta_{tb}^{b}\right]\left(d^{b} - D^{*b}\right) + \\ \left[\Delta_{tb}^{b}\right]\left(\Phi - \Gamma^{*}\right)\eta + \\ + 2\overline{\Xi}_{ib}^{b}\left(\Phi - \Gamma^{*}\right)\dot{\eta} \end{Bmatrix} \end{bmatrix} +$$

$$-\left[2\omega_{it}^{t} \times \dot{r}_{cg}^{t}\right]$$

(46)

$$\ddot{r}_{cg}^{t} = f^{*t} + g^{t} - C_{b}^{t} \begin{bmatrix} \left[\left(\omega_{tb}^{b}\left(\omega_{tb}^{b}\right)^{T}\right) - Tr\left(\omega_{tb}^{b}\left(\omega_{tb}^{b}\right)^{T}\right)\right]\lambda^{*b} - \Phi^{*}\left(\Phi - \Gamma^{*}\right)^{-1}\left[\Delta_{tb}^{b}\right]\left(d^{b} - D^{*b}\right) + \\ \left\{\left[\left(\omega_{tb}^{b}\left(\omega_{tb}^{b}\right)^{T}\right) - Tr\left(\omega_{tb}^{b}\left(\omega_{tb}^{b}\right)^{T}\right)\right]\Phi^{*} - \Phi^{*}\left(\Phi - \Gamma^{*}\right)^{-1}\left[\Delta_{tb}^{b}\right]\left(\Phi - \Gamma^{*}\right)\right\}\eta + \\ + \left[2\overline{\Omega}_{ib}^{b}\Phi^{*} - 2\Phi^{*}\left(\Phi - \Gamma^{*}\right)^{-1}\Xi_{ib}^{b}\left(\Phi - \Gamma^{*}\right)\right]\dot{\eta} + \\ + \Phi^{*}\left(\Phi - \Gamma^{*}\right)^{-1}\left(C_{s}^{b} f^{s} - F^{*b}\right) \end{bmatrix}$$

$$-\left[2\omega_{it}^{t} \times \dot{r}_{cg}^{t}\right]$$

(47)

We can do further simplifications to obtain the final desired expression.

$$\ddot{r}_{cg}^{t} = f^{*t} + g^{t} - C_{b}^{t} \begin{bmatrix} \left[\Delta_{ts*}^{b}\right]_{1,1} \lambda^{*b} - \Phi^{*}\left(\Phi - \Gamma^{*}\right)^{-1}\left[\Delta_{ts*}^{b}\right]\left(d^{b} - D^{*b}\right) + \\ \left\{\left[\Delta_{ts*}^{b}\right]_{1,1}\Phi^{*} - \Phi^{*}\left(\Phi - \Gamma^{*}\right)^{-1}\left[\Delta_{ts*}^{b}\right]\left(\Phi - \Gamma^{*}\right)\right\}\eta + \\ + \left[2\widetilde{\Omega}_{is*}^{b}\Phi^{*} - 2\Phi^{*}\left(\Phi - \Gamma^{*}\right)^{-1}\overline{\Xi}_{is*}^{b}\left(\Phi - \Gamma^{*}\right)\right]\dot{\eta} + \\ + \Phi^{*}\left(\Phi - \Gamma^{*}\right)^{-1}\left(C_{s}^{b}f^{s} - F^{*b}\right) \end{bmatrix} - \left[2\omega_{it}^{t} \times \dot{r}_{cg}^{t}\right]$$

(48)

To verify that we have written correctly Eq.**(48)**, it is useful to perform a dimensional control: $\ddot{r}_{cg}^{t}$ is 3x1 vector, so terms to the right of the equal symbol must have the same dimension.

If we consider the term: $\Phi^{*}\left(\Phi - \Gamma^{*}\right)^{-1}\left[\Delta_{tb}^{b} + \widetilde{\Theta}_{tb}^{b}\right]\left(\Phi - \Gamma^{*}\right)\eta$, it has the following dimension: $\left|3 \ x \ 3m\right| x \left|3m \ x \ 3m\right| x \left|3m \ x \ 3m\right| x \left|3m \ x \ 3m\right| x \left|3m \ x \ 1\right|$, the final dimension of this term is equal to 3x1.

It is useful to underline the physical meaning of terms in square brackets, they represent centripetal and Coriolis acceleration of the centre of gravity and they are evaluated as a weighted mean of the centripetal and Coriolis accelerations sensed by all the accelerometers: the weights are a quantity proportional to mode shapes.

The analysis developed till now, has regarded a general situation in which all accelerometers (IMU and spatially distributed) are tri-axial.

In this application we'll consider mono-axial accelerometers for the spatially distributed ones and just one tri-axial (IMU accelerometer).

To close our system we have other two equations, the first one expresses the evolution of position of c.g. in the tangent frame, the second one expresses the evolution of the rotation matrix between tangent frame and body frame.

$$\dot{r}_{cg}^{t} = V_{cg}^{t}$$

(49)

$$\dot{C}_{b}^{t} = C_{b}^{t}\left(\widetilde{\Omega}_{is*}^{b} - \widetilde{\Omega}_{ie}^{b}\right)$$

(50)

$$\ddot{r}_{cg}^{t} = f^{*t} + g^{t} - C_{b}^{t} \begin{bmatrix} \left[\Delta_{ts*}^{b}\right]_{1,1} \lambda^{*b} - \Phi^{*}\left(\Phi - \Gamma^{*}\right)^{-1}\left[\Delta_{ts*}^{b}\right]\left(d^{b} - D^{*b}\right) + \\ \left\{\left[\Delta_{ts*}^{b}\right]_{1,1}\Phi^{*} - \Phi^{*}\left(\Phi - \Gamma^{*}\right)^{-1}\left[\Delta_{ts*}^{b}\right]\left(\Phi - \Gamma^{*}\right)\right\}\eta + \\ + \left[2\widetilde{\Omega}_{is*}^{b}\Phi^{*} - 2\Phi^{*}\left(\Phi - \Gamma^{*}\right)^{-1}\overline{\Xi}_{is*}^{b}\left(\Phi - \Gamma^{*}\right)\right]\dot{\eta} + \\ + \Phi^{*}\left(\Phi - \Gamma^{*}\right)^{-1}\left(C_{s}^{b}f^{s} - F^{*b}\right) \end{bmatrix} - \left[2\omega_{it}^{t} \times \dot{r}_{cg}^{t}\right]$$

(51)

$$\ddot{\eta} = \left(\Phi - \Gamma^* \right)^{-1} \left[+ \left(C_s^b f^s - F^{*b} \right) - \begin{Bmatrix} \left[\Delta_{tb}^b \right] \left(d^b - D^{*b} \right) + \\ \left[\Delta_{tb}^b \right] \left(\Phi - \Gamma^* \right) \eta + \\ + 2 \overline{\Xi}_{is*}^b \left(\Phi - \Gamma^* \right) \dot{\eta} \end{Bmatrix} \right]$$

(52)

In conclusion the state vector will be composed by the following state variables:

State Vector Components		
Symbol	*Definition*	*Dimensions*
r_{cg}^t	The position of vehicle's centre of gravity in the tangent frame	*(3x1 vector)*
$\dot{r}_{cg}^t$	The speed of vehicle's centre of gravity in the tangent frame	*(3x1 vector)*
η	Generalized Coordinates	*(n x1 vector)*
$\dot{\eta}$	Derivative of the Generalized Coordinates	*(n x1 vector)*
C_b^t	Rotation matrix from body reference frame to tangent frame	*(3x3 matrix)*

Table 2 State Vector for the Navigation Equations

Input Vector		
Symbol	*Definition*	*Dimensions*
f_j^s	Acceleration sensed by spatially distributed accelerometers	*(3(m-1)x1 vector)*
f_{s*}^s	Acceleration sensed by IMU accelerometers set	*(3x1 vector)*
ω_{is*}^s	Angular Speed sensed by IMU gyro set	*(3x1 vector)*

Table 3 Input Vector for the Navigation Equations

The state equations are non linear so it is necessary a linearization around an initial position, that will be coincident with the estimated state vector.

1.3.4 Pertubation Form of the State Equations

1.3.4.1 Introduction

Extended Kalman Filter can be applied to linearized dynamic systems, our dynamic equations are non linear thus we need to linearize them around an equilibrium state.

The state space form, obtained from linearization, is also known as *Perturbation Form* [Eq.**(53)**].

$$\dot{\delta g} = F\delta g + B\delta m$$
$$\delta z = H\delta g + C\delta z_m$$

$$\text{(53)}$$

The error is defined as the difference between the true (*effective*) value and the estimated value of a generic variable.

For the generic state variable g, one has:

$$\delta g = g - \hat{g}$$

$$\text{(54)}$$

A measured physical quantity can be expressed as a sum of a true value and an error (essentially due to instrument imperfections).

$$\tilde{m} = m - \Delta m$$

$$\text{(55)}$$

$\tilde{m}$ represents the measured value of the physical quantity, m the true value and Δm the instrument errors.

It is similarly possible to define an estimation of a physical quantity, measurable with a suitable sensor.

$$\hat{m} = \tilde{m} + \Delta\hat{m}$$

$$\text{(56)}$$

In Eq. **(56)** $\hat{m}$ represents the estimated value of the physical quantity, $\tilde{m}$ the measured value and $\Delta\hat{m}$ the estimation of the instrumentation errors.

Substituting the expression of $\tilde{m}$ [Eq.**(55)**] in Eq. **(56)** we have the final expression for the estimated value of a physical quantity.

$$\hat{m} = m - \delta m$$

$$\text{(57)}$$

in which $\delta m = \Delta m - \Delta\hat{m}$

In this way we have derived a direct relation between the estimation and the true value of a measurable physical quantity with the error relatives to instrument imperfections.

It is possible to specify Eq.**(57)** for accelerations and angular speeds, which are the most important physical quantities measured by an IMU.

It is useful to point out that the measurement of these quantities are given in the sensor reference frame.

For inertial acceleration:

$$\widetilde{f}_s^s = f_s^s - \Delta f_s^s$$

(58)

$$\hat{f}_s^s = \widetilde{f}_s^s + \Delta \hat{f}_s^s$$

(59)

$$\delta\left(f_s^s\right) = \Delta f_s^s - \Delta \hat{f}_s^s$$

(60)

$$\hat{f}_s^s = f_s^s - \Delta f_s^s + \Delta \hat{f}_s^s = f_s^s - \delta\left(f_s^s\right)$$

(61)

For angular speed:

A gyroscope measures the angular speed of the sensor with respect to an inertial reference frame, choosing ECI frame as inertial reference frame, one has:

$$\omega_{is}^s = \omega_{ie}^s + \omega_{tb}^s + \omega_{bs}^s$$

(62)

The measured value of angular speed will contain some errors, included in the term $\Delta\omega_{ib}^s$.

$$\widetilde{\omega}_{is}^s = \omega_{ie}^s + \omega_{tb}^s + \omega_{sb}^s - \Delta\omega_{ib}^s$$

(63)

Considering that terms ω_{ie}^s and ω_{sb}^s are littler than the angular speed of the body reference speed respect to tangent frame, it is possible to include them in the error term.

$$\Delta\omega_{tb}^s = \omega_{ie}^s + \omega_{sb}^s + \Delta\omega_{ib}^s$$

(64)

Therefore we can consider gyros measuring the angular speed of body reference frame respect the tangent reference frame with the addition of an error term $\Delta\omega_{tb}^s$:

$$\widetilde{\omega}_{tb}^s = \omega_{tb}^s - \Delta\omega_{tb}^s$$

(65)

For the estimated values one has an analogous expression:

$$\hat{\omega}_{tb}^s = \widetilde{\omega}_{tb}^s + \Delta\hat{\omega}_{tb}^s$$

(66)

$$\hat{\Delta}\omega_{tb}^s = \hat{\omega}_{ie}^s + \hat{\omega}_{sb}^s + \hat{\Delta}\omega_{ib}^s$$

(67)

$$\delta\left(\Delta\omega_{tb}^s\right) = \Delta\omega_{tb}^s - \hat{\Delta}\omega_{tb}^s = \left(\omega_{sb}^s - \hat{\omega}_{sb}^s\right) + \left(\omega_{ie}^s - \hat{\omega}_{ie}^s\right) + \left(\Delta\omega_{ib}^s - \hat{\Delta}\omega_{ib}^s\right)$$

(68)

The final expression for the estimated value of body angular speed respect tangent frame is:

$$\hat{\omega}_{tb}^{s} = \omega_{tb}^{s} - \Delta\omega_{tb}^{s} + \Delta\hat{\omega}_{tb}^{s} = \omega_{tb}^{s} - \delta\left(\omega_{tb}^{s}\right)$$

(69)

We need a measurement of body angular acceleration respect to tangent frame (it is useful to remember that $\dot{\omega}_{is} = \dot{\omega}_{tb}$ because $\dot{\omega}_{ie} = 0$); but we haven't any suitable sensor to measure it, so we obtain its estimation, through numerical derivative of the angular speed.

$$\hat{\dot{\omega}}_{tb}^{s} = \dot{\omega}_{tb}^{s} - \Delta\dot{\omega}_{tb}^{s} + \Delta\hat{\dot{\omega}}_{tb}^{s}$$

(70)

The error term is equal to angular speed error term (because angular acceleration and speed are measured by the same sensors).

$$\delta\left(\dot{\omega}_{tb}^{s}\right) = \delta\left(\omega_{tb}^{s}\right)$$

(71)

Finally:

$$\hat{\dot{\omega}}_{tb}^{s} = \dot{\omega}_{tb}^{s} - \delta\left(\omega_{tb}^{s}\right)$$

(72)

Moreover one will consider that $\dot{\omega}_{bs}$ could be neglected.

The expressions for instrument error terms will be pointed out in the state augmentation section.

It is useful o remark that knowledge of angular acceleration is not strictly required, but if it is included in the navigation equations performances are improved only in transients.

At the end of this paragraph, it is useful to develop an expression for the estimated value of the generic rotation matrix C. Considering that error term is generally littler than the actual value, one can use the small angle approximation.

$$\hat{C} = \left(I - P\right) C$$

(73)

P matrix represents a small angle rotation matrix ($\cos(\theta) \approx 1 ; \sin(\theta) \approx \theta$)between the two reference frames

$$P = \begin{bmatrix} 0 & \delta\theta_3 & -\delta\theta_2 \\ -\delta\theta_3 & 0 & \delta\theta_1 \\ \delta\theta_2 & -\delta\theta_1 & 0 \end{bmatrix} = -\begin{bmatrix} \delta\theta_1 \\ \delta\theta_2 \\ \delta\theta_3 \end{bmatrix} \times = -\rho \times$$

(74)

The error between the actual and estimated value for a rotation matrix is expressed as:

$$C - \hat{C} = C - \left(I - P\right)C = PC$$

(75)

1.3.4.2 Pertubation form of the Body to Tangent rotation matrix dynamic equation

The dynamic equation for the true rotation matrix between the body reference frame and the tangent reference frame is:

$$\dot{C}_b^t = C_b^t \overline{\Omega}_{tb}^b$$

$$(76)$$

We are interested in obtaining an expression for the vector $\dot{\rho}_b^t$, which represents the error between $\dot{C}_b^t$ and $\hat{\dot{C}}_b^t$.

Considering the definitions presented in the paragraph 1.3.4.1, it is possible to obtain an expression for $\dot{\rho}_b^t$ in terms of the estimated value of the rotation matrix and of the instrumental error of gyroscopes.

$$\hat{\dot{C}}_b^t = \hat{C}_b^t \overline{\hat{\Omega}}_{tb}^b$$

$$(77)$$

$$C_b^t = (I + P_b^t)\hat{C}_b^t \Rightarrow \dot{C}_b^t = (I + P_b^t)\hat{\dot{C}}_b^t + \dot{P}_b^t \hat{C}_b^t$$

$$(78)$$

$$(I + P_b^t)\hat{\dot{C}}_b^t + \dot{P}_b^t \hat{C}_b^t = (I + P_b^t)\hat{C}_b^t \left(\overline{\hat{\Omega}}_{tb}^b + \overline{\delta\Delta\omega}_{tb}^b \right)$$

$$(79)$$

Considering that $\overline{\delta\Delta\omega}_{tb}^b = \overline{\delta\omega}_{tb}^b$ [Eq.(57)]

$$\dot{P}_b^t \hat{C}_b^t = (I + P_b^t)\hat{C}_b^t \left(\overline{\delta\omega}_{tb}^b \right)$$

$$(80)$$

Considering that Eq. **(76)** and Eq. **(78)** represent the same quantity, we have:

$$\dot{C}_b^t = C_b^t \overline{\Omega}_{tb}^b = (I + P_b^t)\hat{C}_b^t \left(\overline{\hat{\Omega}}_{tb}^b + \overline{\delta\omega}_{tb}^b \right)$$

$$(81)$$

Considering that $P_b^t \hat{C}_b^t \left(\overline{\delta\omega}_{tb}^b \right) << \hat{C}_b^t \overline{\delta\omega}_{tb}^b$ we have the desired final expression

$$\dot{\rho}_b^t \cong \hat{C}_b^t \delta\omega_{tb}^b$$

$$(82)$$

$$\dot{\rho}_b^t = F_{\dot{\rho}_b^t \delta\omega_{tb}^b} \delta\omega_{tb}^b$$

$$(83)$$

$$F_{\dot{\rho}_b^t \delta\omega_{tb}^b} = \hat{C}_b^t$$

$$(84)$$

1.3.4.3 Pertubation form of the generalized coordinates first derivative dynamic equation

In this paragraph we'll get the pertubation equation for the generalized coordinates first derivative.

We consider the case with a single distributed triaxial accelerometer, the extension to the more general case with a number *m* of distributed accelerometers is straightforward using matrix formulation.

The expression for the true value of the generalized coordinates vector is:

$$\ddot{\eta} = \left[\Phi_j - \Phi^*\right]^{-1}\left[+\left(C_{sj}^b f_j^s - C_{IMU}^b f^{*s}\right) - \left\{\begin{array}{l}\left[\left(\omega_{tb}^b \left(\omega_{tb}^b\right)^T\right) - \left|\omega_{tb}^b\right|^2 U\right]\left(d_j^b - \lambda^{*b}\right)+ \\ \left[\left(\omega_{tb}^b \left(\omega_{tb}^b\right)^T\right) - \left|\omega_{tb}^b\right|^2 U\right]\left(\Phi_j - \Phi^*\right)\eta + \\ + 2\overline{\Omega}_{ib}^b \left(\Phi_j - \Phi^*\right)\dot{\eta} \end{array}\right\}\right]$$

(85)

Instead Eq. **(85)** applied to estimated value of generalized coordinates vector, is:

$$\hat{\ddot{\eta}} = \left[\Phi_j - \Phi^*\right]^{-1}\left[+\left(\hat{C}_{sj}^b \hat{f}_j^s - \hat{C}_{IMU}^b \hat{f}^{*s}\right) - \left\{\begin{array}{l}\left[\left(\hat{\omega}_{tb}^b \left(\hat{\omega}_{tb}^b\right)^T\right) - \left|\hat{\omega}_{tb}^b\right|^2 U\right]\left(d_j^b - \lambda^{*b}\right)+ \\ \left[\left(\hat{\omega}_{tb}^b \left(\hat{\omega}_{tb}^b\right)^T\right) - \left|\hat{\omega}_{tb}^b\right|^2 U\right]\left(\Phi_j - \Phi^*\right)\hat{\eta} + \\ + 2\overline{\hat{\Omega}}_{ib}^b \left(\Phi_j - \Phi^*\right)\hat{\dot{\eta}} \end{array}\right\}\right]$$

(86)

We can derive an expression for $\delta\ddot{\eta}$, substituting in Eq. **(86)** the definitions of the estimated terms provided previously in the paragraph and finally subtracting Eq. (85).

We will neglect products between perturbation terms.

In this paragraph it will be provided directly the final result of the linearization process.

$$\delta\ddot{\eta} = \left[\Phi_j - \Phi^*\right]^{-1}\left\{\begin{bmatrix} -\omega_{tb}^b\left[(\Phi_j - \Phi^*)\,\hat{\eta}\right]^T C_{IMU}^b - (\omega_{tb}^b)^T(\Phi_j - \Phi^*)\,\hat{\eta}\,C_{IMU}^b + \\ + 2(\Phi_j - \Phi^*)\,\hat{\eta}(\omega_{tb}^b)^T C_{IMU}^b \\ + 2\overline{(\Phi_j - \Phi^*)\,\dot{\hat{\eta}}}\,C_{IMU}^b + \\ -\omega_{tb}^b\left(d_j^{\ b} - \lambda^{*b}\right)^T C_{IMU}^b - (\omega_{tb}^b)^T\left(d_j^{\ b} - \lambda^{*b}\right)C_{IMU}^b + \\ + 2\left(d_j^{\ b} - \lambda^{*b}\right)(\omega_{tb}^b)^T C_{IMU}^b \end{bmatrix}\left(\delta\omega_{tb}^{s*}\right)+ \right.$$
$$\left. + \begin{bmatrix} -\dot{\overline{\Omega}}_{tb}^b(\Phi_j - \Phi^*) + (\omega_{tb}^b)^T(\omega_{tb}^b)(\Phi_j - \Phi^*) + \\ -\omega_{tb}^b(\omega_{tb}^b)^T(\Phi_j - \Phi^*) \end{bmatrix}\delta\eta + \right.$$
$$\left. -2\overline{\Omega}_{tb}^b(\Phi_j - \Phi^*)\,\delta\dot{\eta} + \hat{C}_{sj}^b(\delta f)_j^s - \hat{C}_{IMU}^b(\delta f)_{IMU}^{s*} \right\}$$

<div align="right">(87)</div>

In conclusion the expression for the linearized error equation relative to generalized coordinates $\delta\ddot{\eta}$ (with one triaxial delocalized accelerometer), expressed in a compact form, is:

$$\delta\ddot{\eta} = \left[\Phi_j - \Phi^*\right]^{-1}\left[+ F_{\delta\ddot{\eta}\delta\omega_{tb}^{s*}}^j\left(\delta\omega_{tb}^{s*}\right)+ F_{\delta\ddot{\eta}\delta\eta}^j\,\delta\eta + F_{\delta\ddot{\eta}\delta\dot{\eta}}^j\,\delta\dot{\eta} + F_{\delta\ddot{\eta}(\delta f)_j^s}^j\left(\delta f\right)_j^s + F_{\delta\ddot{\eta}(\delta f)_{IMU}^{s*}}^*\left(\delta f\right)_{IMU}^{s*}\right]$$

<div align="right">(88)</div>

If multiple delocalized accelerometers are installed it is possible to write a matricial expression for $\delta\ddot{\eta}$

$$\delta\ddot{\eta} = \left(\Phi - \Gamma^*\right)^{-1}\left[F_{\delta\ddot{\eta}\delta\omega_{tb}^{s*}}\left(\delta\omega_{tb}^{s*}\right)+ F_{\delta\ddot{\eta}\delta\eta}\,\delta\eta + F_{\delta\ddot{\eta}\delta\dot{\eta}}\,\delta\dot{\eta}_{sj}^b + F_{\delta\ddot{\eta}(\delta f)_j^s}\left(\delta f\right)_j^s + F_{\delta\ddot{\eta}(\delta f)_{IMU}^{s*}}\left(\delta f\right)_{IMU}^{s*}\right]$$

<div align="right">(89)</div>

1.3.4.4 Pertubation form of the center of gravity velocity dynamic equation

In this paragraph we will get the pertubation equation for the velocity of the aircraft center of gravity. To accomplish this purpose we have used the simplest expression for $\ddot{r}_{cg}^t$, because at this stage we are not interested in expressing the term depending on $\ddot{\eta}$ as a function of state variables.

$$\ddot{r}_{cg}^{\,t} = f^{*t} + g^{\,t} - C_b^t\left[\omega_{tb}^b \times \left(\omega_{tb}^b \times \lambda^{*b}\right) + \omega_{tb}^b \times \left(\omega_{tb}^b \times \Phi^*\eta\right) + 2\omega_{ib}^b \times \Phi^*\dot{\eta} + \Phi^*\ddot{\eta}\right] - \left[2\omega_{it}^t \times \dot{r}_{cg}^{\,t}\right]$$

(90)

The estimated value of $\ddot{r}_{cg}^{\,t}$ is:

$$\hat{\ddot{r}}_{cg}^{\,t} = \hat{f}^{*t} + g^{\,t} - \hat{C}_b^t\left[\hat{\omega}_{tb}^b \times \left(\hat{\omega}_{tb}^b \times \lambda^{*b}\right) + \hat{\omega}_{tb}^b \times \left(\hat{\omega}_{tb}^b \times \Phi^*\hat{\eta}\right) + 2\hat{\omega}_{ib}^b \times \Phi^*\hat{\dot{\eta}} + \Phi^*\hat{\ddot{\eta}}\right] - \left[2\hat{\omega}_{it}^t \times \hat{\dot{r}}_{cg}^{\,t}\right]$$

(91)

$\delta\ddot{r}_{cg}^{\,t}$ is evaluable with the following expression :

$$\delta\ddot{r}_{cg}^{\,t} = \left[-\overline{f^{*t}} + \overline{\left(C_b^t\,\overline{\Omega}_{tb}^b\,\Phi^*\hat{\eta}\right)} + \left[C_b^t\,\overline{\Omega}_{tb}^b\,\overline{\left(\Omega_{tb}^b\,\lambda^{*b}\right)}\right] + \left[C_b^t\,\overline{\Omega}_{tb}^b\,\overline{\left(\Omega_{tb}^b\,\Phi^*\hat{\eta}\right)}\right]\right]\rho_b^t$$

$$+ \hat{C}_b^t\overline{\left(H^*\hat{\eta}\right)}\,(\delta f)_{IMU}^{s*} - \overline{\Omega}_{it}^t\,\delta\dot{r}_{cg}^{\,t} - \hat{C}_b^t\,\overline{\Omega}_{tb}^b\,\Phi^*\delta\dot{\eta} - \hat{C}_b^t\left[\overline{\Omega}_{tb}^b\,\overline{\Omega}_{tb}^b\,\Phi^*\right]\delta\eta +$$

$$+ \hat{C}_b^t\left[\begin{array}{c}\overline{\Omega}_{tb}^b\,\overline{(\Phi^*\hat{\eta})} + \overline{\left(\overline{\Omega}_{tb}^b\,\Phi^*\,\hat{\eta}\right)} + \overline{\Omega}_{tb}^b\,\overline{\lambda}^{*b} + \overline{\left(\overline{\Omega}_{tb}^b\,\lambda^{*b}\right)} \\ + \overline{\lambda}^{*b} + \overline{(\Phi^*\hat{\eta})} + \overline{(\Phi^*\hat{\eta})}\end{array}\right]\hat{C}_{IMU}^b\,\delta\omega_{tb}^{s*}$$

$$- \hat{C}_b^t\Phi^*\delta\ddot{\eta}$$

(92)

Defining the following intermediate derivatives:

$$L_{\delta\ddot{r}_{cg}^{\,t}\rho_b^t} = \left[-\overline{f^{*t}} + \overline{\left(C_b^t\,\overline{\Omega}_{tb}^b\,\Phi^*\hat{\eta}\right)} + \left[C_b^t\,\overline{\Omega}_{tb}^b\,\overline{\left(\Omega_{tb}^b\,\lambda^{*b}\right)}\right] + \left[C_b^t\,\overline{\Omega}_{tb}^b\,\overline{\left(\Omega_{tb}^b\,\Phi^*\hat{\eta}\right)}\right]\right]$$

(93)

$$L_{\delta\ddot{r}_{cg}^{\,t}\delta\omega_{tb}^{s*}} = \hat{C}_b^t\left[\overline{\Omega}_{tb}^b\,\overline{(\Phi^*\hat{\eta})} + \overline{\left(\overline{\Omega}_{tb}^b\,\Phi^*\,\hat{\eta}\right)} + \overline{\Omega}_{tb}^b\,\overline{\lambda}^{*b} + \overline{\left(\overline{\Omega}_{tb}^b\,\lambda^{*b}\right)} + \overline{\lambda}^{*b} + \overline{(\Phi^*\hat{\eta})} + \overline{(\Phi^*\hat{\eta})}\right]\hat{C}_{IMU}^b$$

(94)

$$L_{\delta\ddot{r}_{cg}^{\,t}\delta\eta} = -\hat{C}_b^t\left[\overline{\Omega}_{tb}^b\,\overline{\Omega}_{tb}^b\Phi^*\right]$$

(95)

$$L_{\delta\ddot{r}_{cg}^{\,t}(\delta f)_{IMU}^{s*}} = \hat{C}_b^t\overline{\left(H^*\hat{\eta}\right)}$$

(96)

$$L_{\delta\ddot{r}_{cg}^{\,t}\delta\dot{\eta}} = -\hat{C}_b^t\overline{\Omega}_{tb}^b\Phi^*$$

(97)

$$L_{\delta\ddot{r}_{cg}^{\,t}\delta\dot{r}_{cg}^{\,t}} = -\overline{\Omega}_{it}^t$$

(98)

$$L_{\delta\ddot{r}_{cg}^{\,t}\delta\ddot{\eta}} = -\hat{C}_b^t\Phi^*$$

(99)

These derivatives represent $\delta\ddot{r}_{cg}^{\,t}$ complete derivatives if $\delta\ddot{\eta}$ or $L_{\delta\ddot{r}_{cg}^{\,t}\delta\ddot{\eta}}$ were null.

$$\delta\ddot{\eta} = 0 \Rightarrow L_{\delta\,\ddot{r}^t_{cg}..} = F_{\delta\,\ddot{r}^t_{cg}..}$$

(100)

In the general case in which $\delta\ddot{\eta}$ s not null, we have also a derivative $F_{\ddot{r}^t_{cg}\delta\ddot{\eta}}$.

$$F_{\ddot{r}^t_{cg}\delta\ddot{\eta}} = -\hat{C}^t_b \Phi^* (\Phi - \Gamma^*)^{-1} \left[F_{\delta\ddot{\eta}\delta\omega^{s*}_{tb}} \left(\delta\omega^{s*}_{tb}\right) + F_{\delta\ddot{\eta}\delta\eta}\,\delta\eta + F_{\delta\ddot{\eta}\delta\dot{\eta}}\,\delta\dot{\eta} + F_{\delta\ddot{\eta}(\delta f)^s_j}\left(\delta f\right)^s_j + F_{\delta\ddot{\eta}(\delta f)^{s*}_{IMU}}\left(\delta f\right)^{s*}_{IMU} \right]$$

(101)

Complete derivatives are:

$$F_{\ddot{r}^t_{cg}\delta\dot{\eta}} = L_{\delta\,\ddot{r}^t_{cg}\delta\dot{\eta}} + L_{\delta\,\ddot{r}^t_{cg}\delta\ddot{\eta}} (\Phi - \Gamma^*)^{-1} F_{\delta\ddot{\eta}\delta\dot{\eta}}$$

(102)

$$F_{\delta\,\ddot{r}^t_{cg}\rho^t_b} = L_{\delta\,\ddot{r}^t_{cg}\rho^t_b}$$

(103)

$$F_{\ddot{r}^t_{cg}\delta\eta} = L_{\delta\,\ddot{r}^t_{cg}\delta\eta} + L_{\delta\,\ddot{r}^t_{cg}\delta\ddot{\eta}} (\Phi - \Gamma^*)^{-1} F_{\delta\ddot{\eta}\delta\eta}$$

(104)

$$F_{\ddot{r}^t_{cg}(\delta f)^{s*}_{IMU}} = L_{\delta\,\ddot{r}^t_{cg}(\delta f)^{s*}_{IMU}} + L_{\delta\,\ddot{r}^t_{cg}\delta\ddot{\eta}} (\Phi - \Gamma^*)^{-1} F_{\delta\ddot{\eta}(\delta f)^{s*}_{IMU}}$$

(105)

$$F_{\ddot{r}^t_{cg}(\delta f)^s_j} = L_{\delta\,\ddot{r}^t_{cg}\delta\ddot{\eta}} (\Phi - \Gamma^*)^{-1} F_{\delta\ddot{\eta}(\delta f)^s_j}$$

(106)

$$F_{\ddot{r}^t_{cg}\delta\omega^{s*}_{tb}} = L_{\delta\,\ddot{r}^t_{cg}\delta\omega^{s*}_{tb}} + L_{\delta\,\ddot{r}^t_{cg}\delta\ddot{\eta}} (\Phi - \Gamma^*)^{-1} F_{\delta\ddot{\eta}\delta\omega^{s*}_{tb}}$$

(107)

$$F_{\delta\,\ddot{r}^t_{cg}\,\delta\dot{r}^t_{cg}} = L_{\delta\,\ddot{r}^t_{cg}\,\delta\dot{r}^t_{cg}}$$

(108)

The final expression for $\delta\,\ddot{r}^t_{cg}$ expressed in compact form is:

$$\delta\,\ddot{r}^t_{cg} = F_{\delta\,\ddot{r}^t_{cg}\delta\omega^{s*}_{tb}} \left(\delta\omega^{s*}_{tb}\right) + F_{\delta\,\ddot{r}^t_{cg}\delta\eta}\,\delta\eta + F_{\delta\,\ddot{r}^t_{cg}\delta\dot{\eta}}\,\delta\dot{\eta} + F_{\delta\,\ddot{r}^t_{cg}(\delta f)^s_j}\left(\delta f\right)^s_j + F_{\delta\,\ddot{r}^t_{cg}(\delta f)^{s*}_{IMU}}\left(\delta f\right)^{s*}_{IMU} +$$
$$+ F_{\delta\,\ddot{r}^t_{cg}\delta\dot{r}^t_{cg}}\,\delta\dot{r}^t_{cg} + F_{\delta\,\ddot{r}^t_{cg}\rho^t_b}\,\rho^t_b$$

(109)

1.3.4.5 Pertubation form of the dynamic equations: Summary

In this paragraph we will recap all the dynamic equations in their perturbated form. The perturbated state vector is composed by the following variables: $\delta\,r^t_{cg}, \delta\,\dot{r}^t_{cg}, \delta\,\eta, \delta\,\dot{\eta}, \rho^t_b$, while the perturbated input vector is composed by the following variables $(\delta f)^{s*}_{IMU}, \delta\omega^{s*}_{tb}, (\delta f)^s_j$.

For recapitulation purposes we will summarize the meaning of each element composing perturbated state vector and perturbated input vector.

➢ **Perturbated Input Vector**

- o $(\delta f)^{s*}_{IMU}$ represents the inertial acceleration error associated to the measurements of IMU accelerometers.

- o $(\delta f)^{s}_{j}$ represents the inertial acceleration error associated to the measurements of each one of spatially distributed accelerometers.

- o $\delta\omega^{s*}_{tb}$ represents the angular speed error.

➢ **Perturbated State Vector**

- o $\delta\, r^{t}_{cg}$ represents body c.g. position (in tangent frame) error

- o $\delta\, \dot{r}^{t}_{cg}$ represents body c.g. velocity (in tangent frame) error

- o $\delta\, \eta$ represents generalized coordinates vector error

- o $\delta\, \dot{\eta}$ represents derivative of generalized coordinates vector error

- o ρ^{t}_{b} represents the error between true and estimated value of rotation matrix from body r.f to tangent frame.

The mathematical representation of the perturbated state equation is:

$$\dot{\delta g} = F\delta g + B\delta m$$

(110)

The state space representation Eq. **(110)** specialized for our application is reported synthetically in Eq.**(111)**.

$$
\begin{bmatrix} \delta\ddot{r}^{t}_{cg} \\ \delta\dddot{r}^{t}_{cg} \\ \delta\dot{\eta} \\ \delta\ddot{\eta} \\ \dot{\rho}^{t}_{b} \end{bmatrix} =
\begin{bmatrix}
0 & I & 0 & 0 & 0 \\
0 & F_{\delta\ddot{r}^{t}_{cg}\delta\dot{r}^{t}_{cg}} & F_{\delta\ddot{r}^{t}_{cg}\delta\eta} & F_{\delta\ddot{r}^{t}_{cg}\delta\dot{\eta}} & F_{\delta\ddot{r}^{t}_{cg}\rho^{b}_{t}} \\
0 & 0 & I & 0 & 0 \\
0 & 0 & 0 & (\Phi-\Gamma^{*})^{-1}F_{\delta\ddot{\eta}\delta\eta} & 0 \\
0 & 0 & 0 & 0 & 0
\end{bmatrix}
\begin{bmatrix} \delta r^{t}_{cg} \\ \delta\dot{r}^{t}_{cg} \\ \delta\eta \\ \delta\dot{\eta} \\ \rho^{t}_{b} \end{bmatrix} +
$$

$$
+
\begin{bmatrix}
0 & 0 & 0 \\
F_{\delta\ddot{r}^{t}_{cg}(\delta f)^{s*}_{IMU}} & F_{\delta\ddot{r}^{t}_{cg}(\delta f)^{s}_{j}} & F_{\delta\ddot{r}^{t}_{cg}\delta\omega^{s*}_{tb}} \\
0 & 0 & 0 \\
(\Phi-\Gamma^{*})^{-1}F_{\delta\ddot{\eta}(\delta f)^{s*}_{IMU}} & (\Phi-\Gamma^{*})^{-1}F_{\delta\ddot{\eta}(\delta f)^{s}_{j}} & (\Phi-\Gamma^{*})^{-1}F_{\delta\ddot{\eta}\delta\omega^{s*}_{tb}} \\
0 & 0 & F_{\rho^{b}_{t}\delta\omega^{s*}_{tb}}
\end{bmatrix}
\begin{bmatrix} (\delta f)^{s*}_{IMU} \\ (\delta f)^{s}_{j} \\ \delta\omega^{s*}_{tb} \end{bmatrix}
$$

(111)

1.3.4.6 State Augmentation

It is possible to include in the state vector, the sensor error terms having a stochastic behaviour. In this formulation their values are estimated together with the other state variable. This formulation of the perturbated state equations is also known as "**Augmented**".

It is possible to represent sensor error term in the following way:

$$\Delta m = F_{\delta(\Delta m)x_m} x_m + v_m$$

(112)

Where vectors x_m and v_m represent respectively some parameters necessary to calibrate the sensor and a measurement error that we will represent as a White and Gaussian noise.

The estimated value of sensor calibration factors is indicated with $\hat{x}_m$.

$$\hat{\Delta} m = F_{\delta(\Delta m)x_m} \hat{x}_m$$

(113)

$$\delta m = \Delta m - \hat{\Delta} m = F_{\delta(\Delta m)x_m} \delta x_m + v_m$$

(114)

Sensors calibration factors, that we will consider, are Scale Factor and Bias, therefore we use the following error model for inertial sensors.

$$\tilde{m} = \left(I - SF_m \right) \cdot m + b_m$$

(115)

$$\tilde{m} = m - \Delta m = \left(m - SF_m m \right) + b_m \Rightarrow \Delta m = SF_m m - b_m$$

(116)

The estimated value of the term including instrument calibration factors, is

$$\hat{\Delta} m = \hat{SF}_m m - \hat{b}_m$$

(117)

$$\delta m = \delta SF_m m - \delta b_m$$

(118)

$$\delta x_m = \begin{bmatrix} \delta SF_m \\ \delta b_m \end{bmatrix}$$

(119)

It is necessary to define an evolution model for calibration factors.

$$\delta \dot{x}_m = F_{as} \delta x_m + v_m$$

(120)

We'll consider that δSF_m is a constant and determinate a priori, while for δb_m one considers a first order Gauss-Markov process.

$$\delta \dot{b}_m = -k_m \delta b_m + \gamma_{b\_m}$$

(121)

$$\delta \dot{SF}_m = 0$$

(122)

The previous equations will be now specialized for accelerometer and gyroscope error model.

> ➤ **Gyroscope Error Modelling**

A gyroscope measures angular speed between the sensor and inertial reference frame, measured in the sensor reference frame $\widetilde{\omega}_{i\_imu}^{s*}$.

It is possible to distinguish several contributions to the angular speed measured by a gyroscope $\widetilde{\omega}_{i\_imu}^{s*}$: a first term ω_{ie}^{s*} represents the angular speed of the Earth respect to the inertial r.f., a second term ω_{tb}^{s*} represents the angular speed of the body r.f. respect to the tangent r.f., a third term $\omega_{b\_imu}^{s*}$ which represents the angular speed of the sensor respect to the body r.f., an error term $\Delta\omega_{i\_imu}^{s*}$ and finally a white noise ν_{ω} .

$$\widetilde{\omega}_{i\_imu}^{s*} = \omega_{ie}^{s*} + \omega_{tb}^{s*} + \omega_{b\_imu}^{s*} - \Delta\omega_{i\_imu}^{s*} + \nu_{\omega}$$

(123)

Considering that terms $\omega_{ie}^{s}, \omega_{b\_imu}^{s*}$ (in this application we are considering MEMS gyros, thus these terms could be not even sensed by the sensor itself) are considerably littler than ω_{tb}^{s}, they can be considered as a sort of error and included in $\Delta\omega$ [Eq. **(124)**].

$$\Delta\omega_{tb}^{s*} = \omega_{ie}^{s*} + \omega_{b\_imu}^{s*} - \Delta\omega_{i\_imu}^{s*} + \nu_{\omega}$$

(124)

This assumption is equivalent to consider a gyro measuring the angular speed between body r.f. and tangent r.f. with a certain amount of error.

$$\widetilde{\omega}_{is}^{s*} = \omega_{tb}^{s*} + \Delta\omega_{tb}^{s*} \Leftrightarrow \widetilde{\omega}_{tb}^{s*}$$

(125)

The estimated value $\hat{\Delta}\omega_{tb}^{s}$ is

$$\hat{\Delta}\omega_{tb}^{s*} = \hat{\omega}_{ie}^{s*} + \hat{\omega}_{b\_imu}^{s*} - \hat{\Delta}\omega_{i\_imu}^{s*}$$

(126)

$$\delta\left(\omega_{tb}^{s*}\right) = \Delta\omega_{tb}^{s*} - \Delta\hat{\omega}_{tb}^{s*} = \left(\omega_{b\_imu}^{s*} - \hat{\omega}_{b\_imu}^{s*}\right) + \left(\omega_{ie}^{s*} - \hat{\omega}_{ie}^{s*}\right) - \left(\Delta\omega_{i\_imu}^{s*} - \hat{\Delta}\omega_{i\_imu}^{s*}\right) + \nu_{\omega}$$

(127)

We need an expression for each one of the terms appearing in Eq.**(127).**

$$\omega_{ie}^{s} = C_{b}^{s} C_{t}^{b} \omega_{ie}^{t} \Rightarrow \hat{\omega}_{ie}^{s} = \hat{C}_{b}^{s}\left(I - P_{t}^{b}\right) C_{t}^{b} \omega_{ie}^{t}$$

(128)

The rotation matrix between sensor r.f. and body r.f. is expressed as a function of generalized coordinates, analogously the angular speed between these two reference frames.

$$C_b^{sj} = I - \overline{H_j \eta} \Rightarrow \hat{C}_b^{sj} = I - \overline{H_j \hat{\eta}}$$

(129)

$$\hat{\omega}_{ie}^s = \left(I - \overline{H^* \hat{\eta}}\right)\left(I - P_t^b\right)C_t^b \omega_{ie}^t = \left(I - \overline{H^* \hat{\eta}}\right)\left(C_t^b \omega_{ie}^t - P_t^b C_t^b \omega_{ie}^t\right) \approx C_t^b \omega_{ie}^t - P_t^b C_t^b \omega_{ie}^t - \overline{H^* \hat{\eta}}\, C_t^b \omega_{ie}^t$$

(130)

$$\omega_{ie}^s = C_b^s C_t^b \omega_{ie}^t = C_t^b \omega_{ie}^t - \overline{H^* \eta}\, C_t^b \omega_{ie}^t$$

(131)

$$\omega_{ie}^s - \hat{\omega}_{ie}^s = +P_t^b C_t^b \omega_{ie}^t - \overline{H^* \delta\eta}\, C_t^b \omega_{ie}^t = -\overline{C_t^b \omega_{ie}^t} \rho_t^b + \overline{C_t^b \omega_{ie}^t} H^* \delta\eta$$

(132)

$$\omega_{sjb}^{sj} = H_j \dot{\eta} \Rightarrow \hat{\omega}_{s_jb}^{sj} = H_j \dot{\hat{\eta}}$$

(133)

$$\omega_{b\_imu}^{s*} - \hat{\omega}_{b\_imu}^{s*} = H^* \delta\dot{\eta}$$

(134)

$$\Delta\omega_{i\_imu}^{s*} = +SF\,\omega_{i\_imu}^{s*} + b_\omega$$

(135)

$$\hat{\Delta}\omega_{i\_imu}^{s*} = +\hat{SF}_\omega\,\omega_{i\_imu}^{s*} + \hat{b}_\omega$$

(136)

$$\Delta\omega_{i\_imu}^{s*} - \hat{\Delta}\omega_{i\_imu}^{s*} = \left(SF_\omega - \hat{SF}_\omega\right)\omega_{i\_imu}^{s*} + b_\omega - \hat{b}_\omega$$

(137)

Considering that we have considered the scale factor perfectly known, the desired expression for $\delta(\omega_{tb}^s)$ is

$$\delta(\omega_{tb}^{s*}) = -\delta b_\omega - \overline{C_t^b \omega_{ie}^t} \rho_t^b + \overline{C_t^b \omega_{ie}^t} H^* \delta\eta + H^* \delta\dot{\eta} + v_\omega$$

(138)

It is useful to remark that, unlike traditional sensor error modelling, in this formulation [Eq.**(138)**], sensor error depends also on state variables not associate with the sensor itself (for example $\delta\eta$), this circumstance is due to the initial choice to include $\omega_{ie}^s, \omega_{sb}^s$ in a $\Delta\omega$ term.

We are interested in $F_{\delta(\omega_{tb}^{s*})\rho_b^t}$ which is equal to $-F_{\delta(\omega_{tb}^{s*})\rho_t^b}$,because $\rho_b^t = -\rho_t^b$

In conclusion:

$$\delta(\omega_{tb}^{s*}) = -\delta b_\omega + \overline{C_t^b \omega_{ie}^t} \rho_b^t + \overline{C_t^b \omega_{ie}^t} H^* \delta\eta + H^* \delta\dot{\eta} + v_\omega$$

(139)

According to (121) and (122), state equations for gyro biases are:

$$\dot{\delta b}_\omega = -k_\omega \delta b_\omega + \gamma_{b\_\omega}$$

(140)

> ➤ **Accelerometer Error Modelling**

We consider an accelerometers error model composed only by a Scale Factor and Bias.

$$\widetilde{f}_{sj}^{s} = \left(I - SF_{f}\right)f_{sj}^{s} + b_{f} + v_{fj}$$

(141)

The general expression for an accelerometer measurement is Eq.(142)

$$\widetilde{f}_{sj}^{s} = f_{sj}^{s} - \Delta f_{sj}^{s}.$$

(142)

Substituting Eq.(141) in Eq.(142) it is possible to determine the value of Δf_{sj}^{s}

$$\widetilde{f}_{sj}^{s} - f_{sj}^{s} = -\Delta f_{sj}^{s} = \left(I - SF_{f}\right)f_{sj}^{s} + b_{f} + v_{f} - f_{sj}^{s} = -SF_{f}f_{sj}^{s} + b_{f} + v_{fj}$$

(143)

$$\Delta f_{sj}^{s} = +SF_{f}f_{sj}^{s} - b_{f} - v_{fj}$$

(144)

Considering the estimated value of Δf_{sj}^{s}

$$\hat{\Delta}f_{sj}^{s} = +\hat{SF}_{f}f_{sj}^{s} - \hat{b}_{f}$$

(145)

Finally the desired expression for δf_{sj}^{s}

$$\delta f_{sj}^{s} = +\delta SF_{f}f_{sj}^{s} - \delta b_{f} - v_{fj}$$

(146)

As for the gyroscopes, also for accelerometers we will consider a constant and a-priori known scale factor [$\delta SF_{f} = 0$].

$$\delta f_{sj}^{s} = -\delta b_{f} - v_{fj}$$

(147)

For IMU accelerometer set:

$$\delta f_{IMU}^{s*} = -\delta b_{f\_IMU} + v_{j\_imu}$$

(148)

State equation for accelerometer bias is:

$$\dot{\delta b}_{fj} = -k_{fj}\delta b_{fj} + \gamma_{b\_fj}$$

(149)

$$\dot{\delta b}_{f\_imu} = -k_{f\_imu}\delta b_{f\_imu} + \gamma_{b\_f\_imu}$$

(150)

The final expression for the state equations in the augmented state formulation is synthetically reported in Eq.(151) .

$$
\begin{bmatrix}
\delta \ddot{r}^t_{cg} \\
\delta \ddot{r}^t_{cg} \\
\delta \dot{\eta} \\
\delta \ddot{\eta} \\
\dot{\rho}^t_b \\
\dot{\delta b}_\omega \\
\dot{\delta b}_{fj} \\
\dot{\delta b}_{f\_imu}
\end{bmatrix}
=
\begin{bmatrix}
0 & I & 0 & 0 & 0 & 0 & 0 & 0 \\
0 & F^{sa}_{\delta \ddot{r}^t_{cg} \delta \ddot{r}^t_{cg}} & F^{sa}_{\delta \ddot{r}^t_{cg} \delta \eta} & F^{sa}_{\delta \ddot{r}^t_{cg} \delta \dot{\eta}} & F^{sa}_{\delta \ddot{r}^t_{cg} \rho^t_b} & F^{sa}_{\delta \ddot{r}^t_{cg} \delta b_\omega} & F^{sa}_{\delta \ddot{r}^t_{cg} \delta b_{fj}} & F^{sa}_{\delta \ddot{r}^t_{cg} \delta b_{f\_imu}} \\
0 & 0 & 0 & I & 0 & 0 & 0 & 0 \\
0 & 0 & F^{sa}_{\delta \ddot{\eta} \eta} & F^{sa}_{\delta \ddot{\eta} \delta \dot{\eta}} & F^{sa}_{\delta \ddot{\eta} \rho^t_b} & F^{sa}_{\delta \ddot{\eta} \delta b_\omega} & F^{sa}_{\delta \ddot{\eta} \delta b_{fj}} & F^{sa}_{\delta \ddot{\eta} \delta b_{f\_imu}} \\
0 & 0 & F^{sa}_{\dot{\rho}^t_b \delta \eta} & F^{sa}_{\dot{\rho}^t_b \delta \dot{\eta}} & F^{sa}_{\dot{\rho}^t_b \rho^t_b} & F^{sa}_{\dot{\rho}^t_b \delta b_\omega} & 0 & 0 \\
0 & 0 & 0 & 0 & 0 & F^{sa}_{\dot{\delta b}_\omega \delta b_\omega} & 0 & 0 \\
0 & 0 & 0 & 0 & 0 & 0 & F^{sa}_{\dot{\delta b}_{sj} \delta b_{sj}} & 0 \\
0 & 0 & 0 & 0 & 0 & 0 & 0 & F^{sa}_{\dot{\delta s}_{sj} \delta b_{f\_imu}}
\end{bmatrix}
\begin{bmatrix}
\delta r^t_{cg} \\
\delta \dot{r}^t_{cg} \\
\delta \eta \\
\delta \dot{\eta} \\
\rho^t_b \\
\delta b_\omega \\
\delta b_{fj} \\
\delta b_{f\_imu}
\end{bmatrix}
+
$$

$$
+
\begin{bmatrix}
0 & 0 & 0 & 0 & 0 & 0 \\
F^{sa}_{\delta \ddot{r}^t_{cg} \delta v_\omega} & F^{sa}_{\delta \ddot{r}^t_{cg} \delta v_{fj}} & F^{sa}_{\delta \ddot{r}^t_{cg} \delta v_{fimu}} & 0 & 0 & 0 \\
0 & 0 & 0 & 0 & 0 & 0 \\
F^{sa}_{\delta \ddot{\eta} \delta v_\omega} & F^{sa}_{\delta \ddot{\eta} \delta v_{fj}} & F^{sa}_{\delta \ddot{\eta} \delta v_{fimu}} & 0 & 0 & 0 \\
F^{sa}_{\dot{\rho}^b_t \delta v_\omega} & 0 & 0 & 0 & 0 & 0 \\
0 & 0 & 0 & I & 0 & 0 \\
0 & 0 & 0 & 0 & I & 0 \\
0 & 0 & 0 & 0 & 0 & I
\end{bmatrix}
\begin{bmatrix}
v_\omega \\
v_{fj} \\
v_{fimu} \\
\gamma_{b\omega} \\
\gamma_{b\_fj} \\
\gamma_{b\_f\_imu}
\end{bmatrix}
$$

(151)

The generic coefficient $F^{sa}_{\delta a \delta b}$ represents the derivative of δa function relative to δb variable in state augmented representation.

In Table 4 each one of these derivatives will be expressed, as much as possible, as a function of the correspondent derivative in the not augmented perturbated state equation.

Eq. **(151)** represents the dynamic equation of our system, now we need some output equations.

Augmented State	Not Augmented	Augmented State	Not Augmented
$F^{sa}_{\delta\ddot{r}^t_{cg}\delta\ddot{r}^t_{cg}}$	$F_{\delta\ddot{r}^t_{cg}\delta\ddot{r}^t_{cg}}$	$F^{sa}_{\delta\ddot{r}^t_{cg}\delta b_{fj}}$	$-F_{\delta\ddot{r}^t_{cg}(\delta f)^s_{sj}}$
$F^{sa}_{\delta\ddot{r}^t_{cg}\delta\dot\eta}$	$F_{\delta\ddot{r}^t_{cg}\delta\dot\eta} + F_{\delta\ddot{r}^t_{cg}\delta\omega^t_{tb}}H^*$	$F^{sa}_{\delta\ddot{r}^t_{cg}\delta b_{f\_imu}}$	$-F_{\delta\ddot{r}^t_{cg}(\delta f)^{s*}_{IMU}}$
$F^{sa}_{\delta\ddot{r}^t_{cg}\delta\eta}$	$F_{\delta\ddot{r}^t_{cg}\delta\eta} + F_{\delta\ddot{r}^t_{cg}\delta\omega^t_{tb}}\overline{C^b_t\omega^t_{ie}}H^*$	$F^{sa}_{\delta\ddot\eta\delta\eta}$	$\left(\Phi-\Gamma^*\right)^{-1}\left[F_{\delta\ddot\eta\delta\eta} + F_{\delta\ddot\eta\delta\omega^t_{tb}}H^*\right]$
$F^{sa}_{\delta\ddot{r}^t_{cg}\rho^t_b}$	$F_{\delta\ddot{r}^t_{cg}\rho^t_b} + F_{\delta\ddot{r}^t_{cg}\delta\omega^t_{tb}}\overline{C^b_t\omega^t_{ie}}$	$F^{sa}_{\dot\rho^t_b\delta\eta}$	$F_{\dot\rho^t_b\delta\omega^t_{tb}}H^*$
$F^{sa}_{\delta\ddot{r}^t_{cg}\delta b_\omega}$	$-F_{\delta\ddot{r}^t_{cg}\delta\omega^t_{tb}}$	$F^{sa}_{\dot\rho^t_b\delta v_\omega}$	$F_{\dot\rho^t_b\delta\omega^t_{tb}}$
$F^{sa}_{\delta\ddot\eta\delta\eta}$	$\left(\Phi-\Gamma^*\right)^{-1}\left[F_{\delta\ddot\eta\delta\eta} + F_{\delta\ddot\eta\delta\omega^t_{tb}}\overline{C^b_t\omega^t_{ie}}H^*\right]$	$F^{sa}_{\delta\ddot{r}^t_{cg}\delta v_\omega}$	$F_{\delta\ddot{r}^t_{cg}\delta\omega^t_{tb}}$
$F^{sa}_{\delta\ddot\eta\rho^t_b}$	$\left(\Phi-\Gamma^*\right)^{-1}\left[F_{\delta\ddot\eta\delta\omega^t_{tb}}\overline{C^b_t\omega^t_{ie}}\right]$	$F^{sa}_{\delta\ddot{r}^t_{cg}\delta v_{fimu}}$	$-F_{\delta\ddot{r}^t_{cg}(\delta f)^{s*}_{IMU}}$
$F^{sa}_{\delta\ddot\eta\delta b_\omega}$	$-\left(\Phi-\Gamma^*\right)^{-1}F_{\delta\ddot\eta\delta\omega^t_{tb}}$	$F^{sa}_{\delta\ddot\eta\delta v_{fj}}$	$-\left(\Phi-\Gamma^*\right)^{-1}F_{\delta\ddot\eta(\delta f)^s_{sj}}$
$F^{sa}_{\delta\ddot\eta\delta b_{fj}}$	$-\left(\Phi-\Gamma^*\right)^{-1}F_{\delta\ddot\eta(\delta f)^{s*}_{IMU}}$		
$F^{sa}_{\delta\ddot\eta\delta b_{f\_imu}}$	$-\left(\Phi-\Gamma^*\right)^{-1}F_{\delta\ddot\eta(\delta f)^{s*}_{IMU}}$		
$F^{sa}_{\dot\rho^t_b\delta\eta}$	$F_{\dot\rho^t_b\delta\omega^t_{tb}}\overline{C^b_t\omega^t_{ie}}H^*$		
$F^{sa}_{\dot\rho^t_b\rho^t_b}$	$+F_{\dot\rho^t_b\delta\omega^t_{tb}}\overline{C^b_t\omega^t_{ie}}$		
$F^{sa}_{\dot\rho^t_b\delta b_\omega}$	$-F_{\dot\rho^t_b\delta\omega^t_{tb}}$		
$F^{sa}_{\delta b_\omega\delta b_\omega}$	$-k_\omega$		
$F^{sa}_{\delta b_{sj}\delta b_{sj}}$	$-k_{fj}$		
$F^{sa}_{\delta b_{f\_imu}\delta b_{f\_imu}}$	$-k_{f\_imu}$		
$F^{sa}_{\delta\ddot{r}^t_{cg}\delta v_{fj}}$	$-F_{\delta\ddot{r}^t_{cg}(\delta f)^s_j}$		
$F^{sa}_{\delta\ddot\eta\delta v_\omega}$	$\left(\Phi-\Gamma^*\right)^{-1}F_{\delta\ddot\eta\delta\omega^t_{tb}}$		
$F^{sa}_{\delta\ddot\eta\delta v_{fimu}}$	$-\left(\Phi-\Gamma^*\right)^{-1}F_{\delta\ddot\eta\delta(f)^{s*}_{IMU}}$		

Table 4 Derivatives in Augmented State Representation

1.3.5 Output Equations

As aiding measurements we'll consider position and speed measurements provided by two couple of GPS Antenna/Receivers, with their antennas positioned respectively at a distance λ^b_{GPS1} and λ^b_{GPS2} from the IMU.

The installation points have mode shape matrices indicate respectively with the symbols $\Phi^{\#1}$ and $\Phi^{\#2}$.

The first two aiding equations refer to the position and speed measured by one of the GPS receivers/antenna, other two equations refer to the difference between positions/speeds provided by the two GPS receivers/antennas.

The GPS system provides measurements of position in a ECEF (Earth Centered Earth Fixed) or LLH (Latitude, Longitude and Height) reference frame, speed is indeed measured in NED r. f.

In this analysis we consider the position in the ECEF r.f. r^e_{ant} [Eq. **(152)**].

$$r^e_{ant} = C^e_t r^t_{cg} + C^e_t C^t_b \lambda^b_{GPS} + C^e_t C^t_b \Phi^\# \eta + r^{ECEF}_{NED}$$

(152)

Where:

- r^{ECEF}_{NED} represents the origin of the NED r.f. expressed in the ECEF r.f.

- C^e_t represents the rotation matrix from the NED r.f. to the ECEF r.f..

The speed measured at GPS antenna $\dot{r}^t_{ant}$ expressed in the NED r.f. is expressed in Eq.**(153)**:

$$\dot{r}^t_{ant} = \dot{r}^t_{cg} + C^t_b \overline{\Omega^b_{tb}} \lambda^b_{GPS} + C^t_b \overline{\Omega^b_{tb}} \Phi^\# \eta + C^t_b \Phi^\# \dot{\eta}$$

(153)

The other two aiding equations are respectively Eq. **(154)** and Eq.**(155)**.

$$\Delta r^e_{ant} = r^e_{ant1} - r^e_{ant2} = C^e_t C^t_b \left(\lambda^b_{GPS1} - \lambda^b_{GPS2} \right) + C^e_t C^t_b \left(\Phi^{\#1} - \Phi^{\#2} \right) \eta$$

(154)

$$\Delta \dot{r}^t_{ant} = \dot{r}^t_{ant1} - \dot{r}^t_{ant2} = C^t_b \left(\Phi^{\#1} - \Phi^{\#2} \right) \dot{\eta} + C^t_b \overline{\Omega^b_{tb}} \left[\left(\lambda^b_{GPS1} - \lambda^b_{GPS2} \right) + \left(\Phi^{\#1} - \Phi^{\#2} \right) \eta \right]$$

(155)

The last output equation considers the relation between the tangent of the heading angle and the measurements of magnetometers in the body reference frame.

$$\psi_t = \tan \left(\psi \right) = \frac{M^h_y}{M^h_x}$$

(156)

In Eq. **(156)** M^h_y and M^h_x represent the component of Earth magnetic field in the plane North-East (Horizontal plane).

The estimated value of the heading tangent is:

$$\hat{\psi}_t = \tan \psi = \frac{C^t_b(2,1:3) \, C^b_s \tilde{M}^b}{C^t_b(1,1:3) \, C^b_s \tilde{M}^b}$$

(157)

In Eq.**(157)** vector $\tilde{M}^b$ represents the components of Earth magnetic field measured in the body r.f. We have considered being able to correct magnetic sensors errors with a suitable external algorithm or with off-line calibration.

1.3.6 Pertubation Form of the Output Equations

The perturbations equation for GPS antenna position and speed are Eq.**(158)** and Eq. **(159)** :

$$\delta r_{ant}^e = r_{ant}^e - \hat{r}_{ant}^e = C_t^e \delta r_{cg}^t + C_t^e C_b^t \Phi^{\#} \delta\eta - C_t^e \left[\overline{C_b^t \Phi^{\#} \hat{\eta}} + \overline{C_b^t \lambda_{GPS}^b} \right] \rho_b^t$$

(158)

$$\delta \dot{r}_{ant}^t = \delta\ddot{r}_{cg}^t + \left[C_b^t \overline{\Omega_{tb}^b} \Phi^{\#} + \overline{C_t^b \omega_{ie}^t} H^* \right] \delta\eta + \left[C_b^t \Phi^{\#} + H^* \right] \delta\dot{\eta} - \left[\hat{C}_b^t \overline{\Phi^{\#} \hat{\eta}} + \hat{C}_b^t \overline{\lambda_{GPS}^b} \right] \delta b_\omega +$$

$$- \left[\left[\overline{C_b^t \overline{\Omega_{tb}^b} \lambda_{GPS}^b} \right] + \left[\overline{C_b^t \overline{\Omega_{tb}^b} \Phi^{\#} \hat{\eta}} \right] + \left[\overline{C_b^t \Phi^{\#} \hat{\eta}} \right] - \overline{C_t^b \omega_{ie}^t} \right] \rho_b^t$$

(159)

Perturbations equations of GPS antennas relative positions and speeds are Eq. **(160)** and Eq.**(161)**.

$$\delta\Delta r_{ant}^e = C_t^e C_b^t \left(\Phi^{\#1} - \Phi^{\#2} \right) \cdot \delta\eta - C_t^e \left[\overline{C_b^t \left(\lambda_{GPS1}^b - \lambda_{GPS2}^b \right) + C_b^t \left(\Phi^{\#1} - \Phi^{\#2} \right) \eta} \right] \rho_b^t$$

(160)

$$\delta\Delta\dot{r}_{ant}^t = C_b^t \left(\Phi^{\#1} - \Phi^{\#2} \right) \delta\dot{\eta} + C_b^t \overline{\Omega_{tb}^b} \left(\Phi^{\#1} - \Phi^{\#2} \right) \delta\eta +$$

$$C_b^t \overline{\left[\left(\lambda_{GPS1}^b - \lambda_{GPS2}^b \right) + \left(\Phi^{\#1} - \Phi^{\#2} \right) \eta \right]} \delta b_\omega - C_b^t \left(\overline{\Omega_{tb}^b} \left[\left(\lambda_{GPS1}^b - \lambda_{GPS2}^b \right) + \left(\Phi^{\#1} - \Phi^{\#2} \right) \eta \right] + \left(\Phi^{\#1} - \Phi^{\#2} \right) \dot{\eta} \right) \rho_b^t$$

(161)

The error term $\delta\psi_t = \psi_t - \hat{\psi}_t$ is only a function of ρ_t^b.

$$\delta\psi_t = H_{\delta\psi_t \rho_t^b} \rho_t^b$$

(162)

In Eq.**(163)** output equations are summarized in a matrix form. The H terms represent the derivatives indicated in equations **(158)**, **(159)**, **(160)**, **(161)** and **(162)**.

$$
\begin{bmatrix} \delta r^e_{ant\,1} \\ \delta \ddot{r}^t_{ant\,1} \\ \delta \Delta r^e_{ant} \\ \delta \Delta \dot{r}^t_{ant} \\ \delta \psi_t \end{bmatrix}
=
\begin{bmatrix}
H_{\delta r^e_{ant\,1} \delta r^t_{cg}} & 0 & H_{\delta r^e_{ant\,1} \delta\eta} & 0 & H_{\delta r^e_{ant\,1} \rho^b_t} & 0 & 0 & 0 \\
0 & H_{\delta \dot{r}^e_{ant\,1} \delta \dot{r}^t_{cg}} & H_{\delta \dot{r}^e_{ant\,1} \delta\eta} & H_{\delta \dot{r}^e_{ant\,1} \delta\dot{\eta}} & H_{\delta \dot{r}^e_{ant\,1} \rho^b_t} & H_{\delta \dot{r}^e_{ant\,1} \delta b_\omega} & 0 & 0 \\
0 & 0 & H_{\delta \Delta r^e_{ant} \delta\eta} & 0 & H_{\delta \Delta r^e_{ant} \rho^b_t} & 0 & 0 & 0 \\
0 & 0 & H_{\delta \Delta \dot{r}^e_{ant} \delta\eta} & H_{\delta \Delta \dot{r}^e_{ant} \delta\dot{\eta}} & H_{\delta \Delta \dot{r}^e_{ant} \rho^b_t} & H_{\delta \Delta \dot{r}^e_{ant} \delta b_\omega} & 0 & 0 \\
0 & 0 & 0 & 0 & H_{\delta \psi_t \rho^b_t} & 0 & 0 & 0
\end{bmatrix}
\begin{bmatrix} \delta r^t_{cg} \\ \delta \dot{r}^t_{cg} \\ \delta\eta \\ \delta\dot{\eta} \\ \rho^b_t \\ \delta b_\omega \\ \delta b_{fj} \\ \delta b_{f\_imu} \end{bmatrix}
+
$$

$$
+
\begin{bmatrix}
1 & 0 & 0 & 0 & 0 \\
0 & 1 & 0 & 0 & 0 \\
0 & 0 & 1 & 0 & 0 \\
0 & 0 & 0 & 1 & 0 \\
0 & 0 & 0 & 0 & 1
\end{bmatrix}
\begin{bmatrix} \kappa_{Rgps} \\ \kappa_{Vgps} \\ \kappa_{\Delta Rgps} \\ \kappa_{\Delta Vgps} \\ \kappa_{\psi_t} \end{bmatrix}
$$

$$(163)$$

2 On-Line Shape Changes Estimation for Flexible Aircrafts

2.1 Problem Overview

A new approach to estimate both navigation states and generalized coordinates has been proposed in the previous chapter.

As already affirmed, the generalized coordinates, associated with the knowledge of the mode shapes, can be used to describe the elastic displacements showed by the aircraft's structure.

A new vision on the problem of elastic displacements estimation will be provided in this chapter. As it will be shown, it is a simplified approach, because it neglects influence of the rigid state error on flexible state error and vice versa.

It is useful to highlight that this approach is more flexible from the point of view of navigation, because it is possible to consider or neglect shape changes in navigation algorithm depending on the specific application (for typical aircrafts using GPS, in the standalone operative mode, the influence of flexible deflections on GPS measurements can be neglected; otherwise it cannot be neglected if some differential corrections or carrier phase measurements are used).

The difference from the approach of chapter 1 is in the presence of two different estimation algorithms, the first one dedicated only to shape changes determination (based on the same modeling of chapter 1, this algorithm is dedicated to determination of generalized coordinates and their first derivatives) and the second one dedicated to the estimation of state variables associated to the rigid body dynamics.

Such a kind of approach is to prefer, whenever possible, because it is computationally less burdensome.
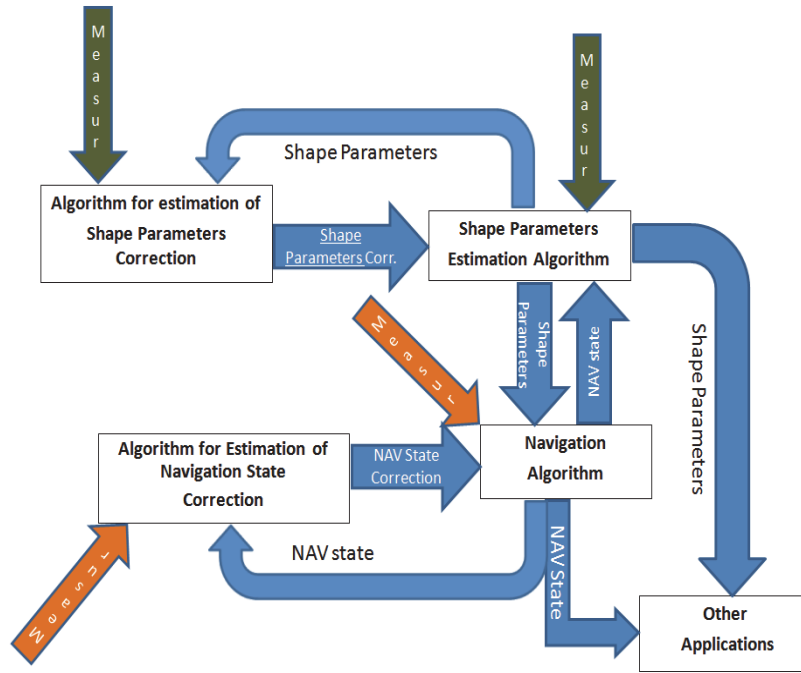
Figure XI Schematic representation of connection between shape changes estimation algorithm and other functionalities considering influences of flexibility on navigation parameters.
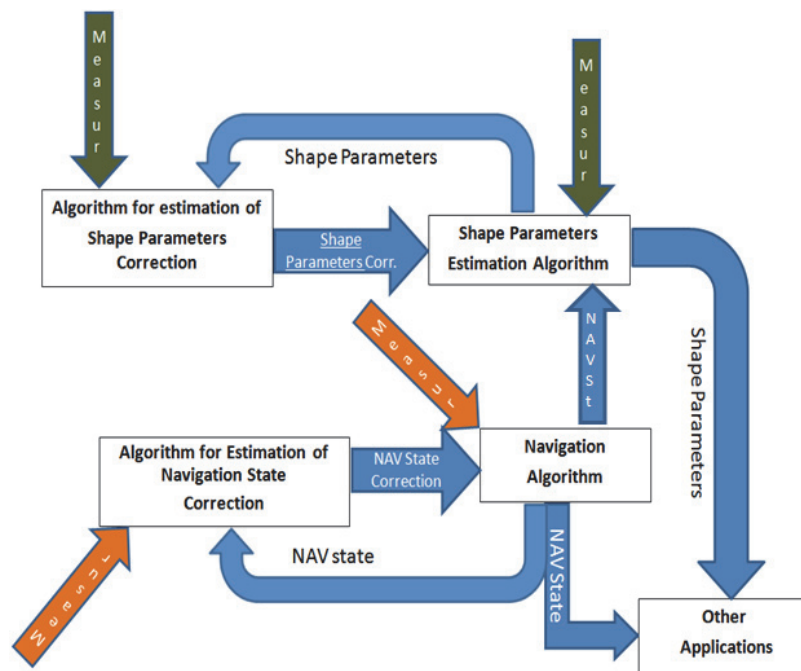
Figure XII Schematic representation of connection between shape changes estimation algorithm and other functionalities without considering influences of flexibility on navigation parameters.

From a mathematical point of view, the previous architecture represents the association of two parts:

a) an algorithm for the estimation of the flexible state variables η and ή (integration of the non-linear equation **(164)**) together with the corresponding algorithm for propagation of the correction [Eq. **(165)**] (for example an EKF);

   b) an algorithm for the estimation of the navigation parameters $r,\ \dot{r}$ and $\rho_b{}^t$ (integration of non-linear equations) together with the corresponding algorithm for propagation of the correction [Eq.**(168)**] (for example an EKF).

In the navigation equations, flexible variables can be included or neglected according to the architecture of Figure XI or Figure XII (respectively Eq.**(166)** or Eq.**(167)**).

$$\ddot{\eta} = t\left(\eta, \dot{\eta}, f_{imu}, f_{sens}, \omega\right)$$

(164)

$$\begin{bmatrix} \delta\dot{\eta} \\ \delta\ddot{\eta} \end{bmatrix} = \begin{bmatrix} 0 & I \\ F^{sa}_{\delta\ddot{\eta}\delta\eta} & F^{sa}_{\delta\ddot{\eta}\delta\dot{\eta}} \end{bmatrix} \begin{bmatrix} \delta\eta \\ \delta\dot{\eta} \end{bmatrix} + \begin{bmatrix} 0 & 0 & 0 \\ F^{sa}_{\delta\ddot{r}^t_{cg}\delta v_\omega} & F^{sa}_{\delta\ddot{\eta}\delta v_{fj}} & F^{sa}_{\delta\ddot{\eta}\delta v_{fimu}} \end{bmatrix} \begin{bmatrix} v_\omega \\ v_{fj} \\ v_{fimu} \end{bmatrix}$$

$$\left[\delta y_{el}\right] = \begin{bmatrix} H_1 & H_2 \end{bmatrix} \begin{bmatrix} \delta\eta \\ \delta\dot{\eta} \end{bmatrix} + \kappa_{el}$$

(165)

$$\ddot{r}^t_{cg} = q\left(\dot{r}^t_{cg}, \rho^t_b, f_{imu}, f_{sens}, \omega\right)$$
$$\dot{\rho}^t_b = z\left(\rho^t_b, \omega\right)$$
$$\dot{b}_{f\_imu} = p^1\left(b_{f\_imu}\right)$$
$$\dot{b}_{fj} = p^2\left(b_{fj}\right)$$
$$\dot{b}_\omega = p^3\left(b_\omega\right)$$

(166)

$$\ddot{r}^t_{cg} = q'\left(\dot{r}^t_{cg}, \rho^t_b, \eta, \dot{\eta}, \ddot{\eta}, f_{imu}, f_{sens}, \omega\right)$$
$$\dot{\rho}^t_b = z\left(\rho^t_b, \omega\right)$$
$$\dot{b}_{f\_imu} = p^1\left(b_{f\_imu}\right)$$
$$\dot{b}_{fj} = p^2\left(b_{fj}\right)$$
$$\dot{b}_\omega = p^3\left(b_\omega\right)$$

(167)

$$
\begin{bmatrix} \delta\ddot{r}^t_{cg} \\ \delta\dot{r}^t_{cg} \\ \dot{\rho}^t_b \\ \delta\dot{b}_\omega \\ \delta\dot{b}_{fj} \\ \delta\dot{b}_{f\_imu} \end{bmatrix} = \begin{bmatrix} 0 & I & 0 & 0 & 0 & 0 \\ 0 & F'_{\delta\dot{r}^t_{cg}\delta\dot{r}^t_{cg}} & F'_{\delta\dot{r}^t_{cg}\rho^t_b} & F'_{\delta\ddot{r}^t_{cg}\delta b_\omega} & F'_{\delta\ddot{r}^t_{cg}\delta b_{fj}} & F'_{\delta\ddot{r}^t_{cg}\delta b_{f\_imu}} \\ 0 & 0 & F'_{\delta\ddot{\eta}\rho^t_b} & F'_{\dot{\rho}^t_b\delta b_\omega} & 0 & 0 \\ 0 & 0 & 0 & F'_{\delta\dot{b}_\omega\delta b_\omega} & 0 & 0 \\ 0 & 0 & 0 & 0 & F'_{\delta\dot{b}_{sj}\delta b_{sj}} & 0 \\ 0 & 0 & 0 & 0 & 0 & F'_{\delta\dot{S}_{sj}\delta b_{f\_imu}} \end{bmatrix} \begin{bmatrix} \delta r^t_{cg} \\ \delta\ddot{r}^t_{cg} \\ \rho^t_b \\ \delta b_\omega \\ \delta b_{fj} \\ \delta b_{f\_imu} \end{bmatrix} +
$$

$$
+ \begin{bmatrix} 0 & 0 & 0 & 0 & 0 & 0 \\ F'_{\delta\ddot{r}^t_{cg}\delta v_\omega} & F'_{\delta\ddot{r}^t_{cg}\delta v_{fj}} & F'_{\delta\ddot{r}^t_{cg}\delta v_{fimu}} & 0 & 0 & 0 \\ F'_{\dot{\rho}^b_t\delta v_\omega} & 0 & 0 & 0 & 0 & 0 \\ 0 & 0 & 0 & I & 0 & 0 \\ 0 & 0 & 0 & 0 & I & 0 \\ 0 & 0 & 0 & 0 & 0 & I \end{bmatrix} \begin{bmatrix} v_\omega \\ v_{fj} \\ v_{fimu} \\ \gamma_{b\omega} \\ \gamma_{b\_fj} \\ \gamma_{b\_f\_imu} \end{bmatrix}
$$

$$
\begin{bmatrix} \delta y_{rig} \end{bmatrix} = \begin{bmatrix} C_1 & C_2 & C_3 & C_4 & C_5 & C_6 \end{bmatrix} \begin{bmatrix} \delta r^t_{cg} \\ \delta\ddot{r}^t_{cg} \\ \rho^t_b \\ \delta b_\omega \\ \delta b_{fj} \\ \delta b_{f\_imu} \end{bmatrix} + \kappa_{rig}
$$

(168)

With reference to Eq. **(165)**, in this chapter the output equations used within an EKF for generation of corrections, will be described.

2.2 State of the Art

In order to measure structural displacements, several systems have been proposed in the specialized literature.

The use of GPS, standalone or in general without application of carrier phase differences technique, limits the capability to estimate only structural displacements of extremely flexible aircrafts, showing displacements with an order of magnitude of several meters (as for example NASA HELIOS aircraft [40]), because in standalone operative mode the GPS shows low accuracy.

In [41] it is proposed a control system for spatial flexible structures based on differential carrier phase measurements obtained using an array of GPS antennas. The differential carrier phase measurements are used to assess deformations.

Furthermore differential techniques as RTK (Real Time Kinematic) or carrier phase differences present some disadvantages that will be identified in the following.

Concerning civil engineering, the Structural Health Monitoring is the main field in which the knowledge of the structural shape is required. Some techniques applied in this field could be applied also to aerospace structures.

Some works propose integration of GPS with accelerometers in order to estimate displacements of civil structures, taking advantage of their complementary dynamic properties and using accelerometers measurements to recover GPS false or missing data. In [42] the results, of some experimental tests conducted on a test rig simulating the typical dynamics of a bridge, are reported. In [43] and [44] a sensor setup, composed by GPS and an accelerometer, is applied to monitor a 108 meters high steel tower during typhoons and earthquakes. In [45] Fiber Bragg Grating (FBGs) optical sensors are included in the measurement system, together with GPS and accelerometers. In [46] an array of several GPS antennas is installed on the Pacoima Dam (California) in order to measure its deformations. The measurements obtained in three years have been analyzed and the final result is that a mean displacement, between the reference points on the dam, and the actual positions of the same points has an order of magnitude of some tenths of millimeters. This analysis has been performed offline, averaging GPS measurements (batch processing); this allows reaching a millimetric accuracy in GPS measurements. In [47] another example of integration between GPS and accelerometers measurements for bridge monitoring is provided.

Obviously the batch approach cannot be used in real time application, as for example for the aircraft active control and moreover the accuracy of GPS standalone in real time is considerably worst than the one available with a post-processing of measurements. RTK technique (which allows obtaining an accuracy of some centimeters) is not always suitable to be used in dynamical environments and moreover the maximum distance between the rover and the base station is limited to 10 km [48]. Furthermore a GPS device, enabled to receive RTK corrections, is more expensive than a simple GPS receiver standalone (the price depends on the corrections update rate and can reach some thousands of US dollars). Concerning carrier phase measurements, the resolution of initial integer ambiguity is required. Moreover GPS signals could be lost during some maneuvers and consequently compromise the control or monitoring action.

To overcome limitations due essentially to GPS and previously presented, integration of a vision-based system with accelerometers and/or GPS has been widely examined and applied above all in civil engineering, specifically for monitoring of bridges and tall buildings.

A vision-based system, alone or coupled with accelerometers, provides compactness and affordable price.

Like GPS, a vision-based system allows obtaining a direct measurement of displacement but with a higher accuracy. Furthermore videometry offers the same level of accuracy of contact devices as optical fibers, but at the same time, it is more flexible in usage [49].

In [50] and [51] it is analyzed the application of a vision based sensor system for direct determination of displacement time histories at selected locations on a bridge undergoing to ambient oscillations. The sensor architecture includes a video-camera coupled with targets (two high resolution low-power light emitting diodes (LEDs)) spaced with a known distance. These two targets are installed under the bridge deck near the mid span, while the camera is placed on one column of the bridge. Measuring the relative motions between the two targets is possible to determine the bridge displacements. The results of a test, performed on Vincent Thomas Bridge in Los Angeles, are reported. Specifically, a displacement time history is reproduced and the frequencies, correspondent to the first two modes, are identified. According to the authors, the measurements obtained with the vision based system are coherent with the same information obtained using the accelerometer array already installed on the bridge. In order to detect modifications in structural properties (specifically dynamic features of a structure) for SHM purposes, in [52] it is presented another application of a vision-based system composed only by a camera. No optical targets are mounted on the bridge, because the applied image processing technique requires the selection of some reference points in the first frame (their coordinates must be provided to the algorithm with a sub-pixel accuracy) and consequently it follows their displacements in the following video frames.

In the aerospace field there are few examples of videometry applications to detect structural displacement.

An application of a vision-based system for identification of structural modes of vibration in the aeronautical field is presented in [53]. In this paper two techniques are examined: specifically an online technique based on a multi sensor vision system and an offline technique based on a single camera. Offline measurements based on batches of data are suitable to obtain higher accuracy. The online technique is more suitable to be used in dynamic environments but the different cameras need to be synchronized and the HW is more complex.

Both the approaches presented in [53] are addressed to the experimental identification of wing structural modes through laboratories tests not true flights.

In the aeronautical field, videometry is also extensively used for wind tunnel tests, to evaluate both aerodynamic and structural properties.

In [54] an application of range imaging sensors is proposed in order to estimate elastic displacements of spatial structures; the proposed system is based on a vision based system installed on robots orbiting around the space structure. Such a kind of system is not suitable for aeronautical applications in which the video-based system has to be necessarily installed on the aircraft.

In [55] an application of a stereo-vision system for deformation determination of a large flexible satellite is presented. In case of satellite, the solar arrays or large phased array radars are the parts more sensitive to deformations.

The application of accelerometers, as only means to determine shape variations, is not suitable due to bias integration and high sensibility to disturbances present in the spatial environment, thus a system which can directly determine displacements could be more robust to these problems and, moreover, a video system is nonintrusive (in the sense that the cameras could be installed on the body of the satellite and not directly on the deformable structure) except for the presence of LED on the structure. A multi-view vision system is composed at least by a pair of cameras opportunely arranged or more cameras depending on the structure dimensions and cameras field of view. Obviously a multi-view vision system induces a greater increment to the overall mass of the system than a single camera.

2.3   Vision Based System Architecture

The vision-based system consists of an emitter-receiver pair operating at visible or infrared wavelength.

In the proposed setup the receiver is a digital camera, the emitter is a Light-Emitting-Diode (LED). The system output consists of the LED image coordinates in the Camera acquired frames.

Both Camera and LED follow linear and rotational deformations of the mounting points.

The Camera Field of View (FOV) is selected to keep the LED image within the frame in the case of maximum deformation.

The operative condition is assumed fine weather and good visibility. Perturbative phenomena of weather conditions able to create refractions or occlusions, as fog or precipitation of various kinds, are neglected.

The model of vision system includes the image projection model and the measurement error model.

In the first one, the equations of projective geometry define the transformation of the LED position from the three dimensional space to its projection in the bidimensional frame.

Let be the origin of the Camera reference frame in the optical centre of the camera system, the *x*-axis (left-right direction) and *y*-axis (down-up direction) parallel to the sensor surface, the *z*-axis orthogonal to the sensor surface and with back-front direction with respect to the image plane. The orientation of such reference frame follows the elastic rotation of the Camera mounting point.

Named x_c, y_c, z_c the LED coordinates in the Camera Reference Frame, the LED coordinates u, v respect to the 2D video frame (with origin in the top left corner and positive indices for rows and columns), measured in pixels, may be written as in eq. **(169)** and **(170)**:

$$u = \frac{f_u x_c}{z_c} + u_o$$

$$\text{(169)}$$

$$v = \frac{-f_v y_c}{z_c} + v_o$$

$$\text{(170)}$$

where u_0, v_0 are constant off-sets and f_u, f_v are the positive values, measured in pixel, of the focal length normalized respectively with respect to the vertical and the horizontal size of a generic photosensitive element of the camera sensor.

The LED coordinates x_c, y_c, z_c are related to mode shapes and generalized coordinates through Eq. **(24)**.
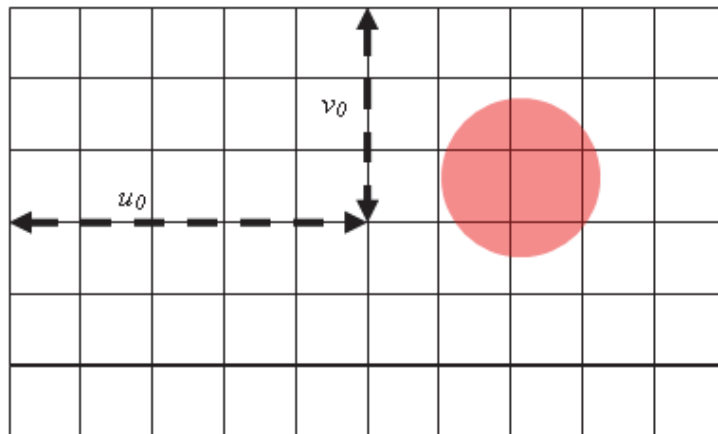
Figure XIII Image Reference Frame

In the system model two sources of error have been considered.

The first one is the truncation error due to the pixel quantization in the digital acquisition.

The second one is the approximation error on the 3D position of the LED: $P_c \equiv (x_c, y_c, z_c)$, ideally coincident with the centre of the brightest part of the light spot, that could be not clearly distinguishable in the image. In fact many pixels around the projection (u, v) of P_c can have very similar values. Usually the projection of the light spot centre, under a small error, can be estimated with the barycentre of the pixels with the highest response. Under the previous hypothesis it can be supposed that the coordinates founded by the image processing algorithms are the projection of an immaterial 3D point belonging to an uncorrelated Gaussian distribution centred in P_c and with a standard deviation comparable to the physical dimensions of the LED, identical for every component.

Because the wing range of deformation is known (by experimental evidence or by mechanical considerations), the optical zoom of the camera can be tuned with aim to minimize the field of view.

Special filters can be mounted on the optic in order to increase the sensitivity to the wavelengths emitted by the LED and decrease the sensitivity to other undesired wavelengths.

The area, in which the LED is installed, has to be painted with a low refraction index varnish at the selected wavelengths.

Under the previous setup conditions, the light spot is easily distinguishable due to its high contrast with the background. On the base of projective geometry considerations, the shape and the dimensions in pixels of the light spot projection are approximately known so that it is easy to design a bidimensional digital filter able to detect the LED in the image [56]. Because the aspect of the image patch around the light spot projection, at sufficiently high frame rates, varies slowly with its location in the image, a simple patch comparison strategy based on block matching algorithms [57] can be implemented. A rectangular patch representing the projection of the light spot in the image is taken as reference template. At the beginning, during the initialization phase, when the wing is still undeformed, the 3D LED position is exactly known, therefore the reference patch can be easily localized around its 2D projection. During the operation phase, at the end of every update step, the previously used template can be replaced with an updated version, that is obtained by the cut of the current image around the predicted 2D location of the LED projection. These coordinates can be obtained projecting the last 3D position of the LED estimated by the sensor fusion algorithm presented in the paper or otherwise using an independent visual tracking algorithm that estimates the apparent 2D motion of the visual objects in the scene (optical flow) [58]. The reference patch is then compared with small, overlapped, portions of the image that have exactly the same dimensions of the template patch and that belong to a limited search window around the

predicted 2D LED coordinates; the search window, thanks to the use of tracking, is usually smaller than the whole image so that the computational burden can be strongly reduced. The minimum admissible dimensions of the search window depend on the projected area of the spot and on the prediction uncertainty. The best match in terms of the reference metric, for example the mean square error, is used to determine the current 2D location of the spot.

The same type of algorithms, described above, is also used in video coding [59].

They are currently able to work at 30-60 Hz on Central Processing Units (CPUs) or Digital Signal Processors (DSPs) for consumer electronics applications.

3 Load Alleviation Methods and Systems

3.1 Introduction

In this chapter it will presented a method to control elastic motions of a flexible aircraft (control of elastic motions is included in Load Alleviation and Gust Control techniques) using a suitable control law associated with the algorithm for estimation of generalized coordinates and their first derivatives, presented in the previous chapter.

As it will be shown later, the conventional control surfaces will be used to contrast elastic motions.

The analysis of the system will be preceded by a short description of the most important state of the art applications in this field.

3.2 State of The Art

In [60] a large-degree-of-freedom, transonic, inviscid computational fluid dynamics/finite element model of a fighter aircraft is coupled with a flight control system for aeroelastic oscillation reduction. A Reduced-Order Model, several orders of magnitude smaller and able to capture the dynamic characteristics of the full system, is then derived for system analysis and control design. A modal decomposition is used to describe the structural deformation. In the general formulation, a certain number of structural node displacements, velocities or accelerations is assumed to be available for the control law.

In [61] an analytical and experimental investigation, into the use of active lifting surfaces with distributed strain actuators for dynamic aeroelastic control, is described. In the test configuration, laser sensors measure the tip displacement at the leading edge, midchord and trailing edge of the tested wing. It is although observed that actual lifting surfaces are not able to take advantage of such displacement measurements, whereas they have ample space for accelerometers, the output of which can be integrated to yield measurements equivalent to the displacement measurements.

In [62] experimental and analytical results of gust response of a scaled transport type wing, with a gust load alleviation system, are presented. Several output feedback control laws are compared using accelerometers, strain gage or both. A simultaneous use of the accelerations and strains measurements is demonstrated to be more effective, because when only the signals from the accelerometers are used the effect of the control is quite deteriorate, mainly because signals from accelerometers represent not only the wing motion ,but also the gravity component with the opposite directional effect.

In [63] an analytical design technique, for an active flutter-suppression and gust-alleviation control system, is presented. The focus is mainly on optimization of a predetermined partial feedback control law, over a wide range of aerodynamic parameters.

In [63] the problem of obtaining the required measurements is not covered. It is only stated that the optimized control laws are physically realizable because measurements concern actual structural motion.

The applicability of Active Control, and thus the capability of obtaining measurements required by control laws are not limited to aerospace engineering.

In [64] the authors investigate the optimal deployment of one type of trailing-edge device, the micro-tabs, in conjunction with collective and individual pitch control to provide effective load alleviation for wind Turbines. The microtab control system consists of a Proportional-Derivative feedback design that requires tip deflection as the feedback signal. All these works and many others demonstrate the need for a proper estimation of the structural motions.

In [65] it is proposed an algorithm able to elaborate onboard sensor measurements for real time estimation of structural motion of a flexible aircraft and more in general to include the influence of elastic motion in the navigation equations.

In [65] and [66] the modal decomposition it is used to describe the structural displacements, thus an Extended Kalman Filter based on measurements of a suitable sensor setup, is used to estimate generalized coordinates and their first derivatives.

The innovative proposal presented in this paper is the coupling of such a kind of algorithm with an active control function, which is based on an optimal state feedback control law for Gust Alleviation.

In the field of Gust Alleviation, the knowledge of generalized coordinates allows the direct control of the structural loads by means of an optimal state feedback control technique. The overall structure represents an LQG (Linear-Quadratic Gaussian) control technique applied to the structural Load Alleviation.

The effectiveness and features of the proposed approach are verified through numerical simulations, performed using a complete aeroelastic model of a flexible UAV, and a realistic modeling of sensors included in the proposed setup. The proposed sensor setup, which integrates inertial measurements of accelerometers and gyros with the output of a vision based system with a target LED positioned in a suitable point of the aircraft, represents another aspect of innovation in the field of Load Allevation techniques.

The advantadges, provided by this sensor setup, are: compactness, high accuracy and low cost.

3.3 System Description

The proposed active control system uses the conventional control surfaces to alleviate the wing loads and reduces the structural deformation during maneuvers or gust occurrences.

The logical scheme of the load alleviation system is depicted in Figure XIV. The vehicle, modeled simply by the Bare Aircraft, the Actuators and Sensors modules, is subject to the control signals u. These signals represent the sum of the attitude control contribute, u_{ac}, and the term due to the Load Alleviation control, u_{la}.
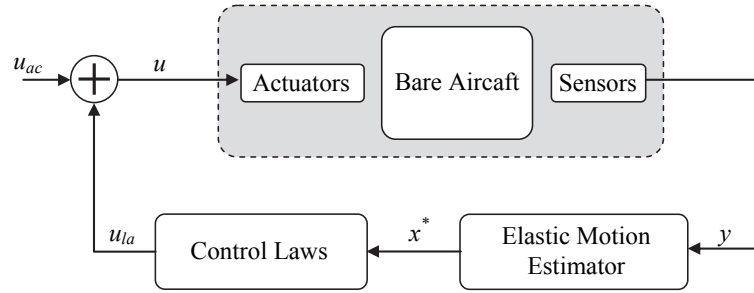
Figure XIV The logical scheme of the Load Alleviation System

Since the attitude control is not the focus of this paper, only the Load Alleviation contribute is here considered. This term is provided by the Control Laws, that process the estimated elastic state, x^*, which is provided by the Elastic Motion Estimator, combining the raw sensors measurements, y, which include both inertial measurements and displacements provided by a vision-based system.

In the following section the Control Laws for the load alleviation are fully discussed, while the Elastic Motion Estimator has been described in detail in the previous chapter. The control is a classic LQ state feedback control, thus forming a LQG control structure.

As already mentioned, the control laws are based on the classic Linear Quadratic optimal control technique with state feedback [67]. Even though, LQ control is a well known technique, some recalls are given below for the sake of completeness along with the implementation details.

The mathematical description of the generic elastic structure of the aircraft is given in Eq. **(171)**, where η_i represent the *i-th* generalized coordinate, while M_i, ς_i, ω_i and Q_i represent, respectively, the corresponding generalized mass, the damping factor, the resonance angular frequency, and the generalized aerodynamic force.

$$M_i\ddot{\eta}_i + \varsigma_i\dot{\eta}_i + M_i\omega_i\eta_i = Q_i$$
$$i = 1,\ldots,n$$

(171)

Note that each Q_i depends on the rigid body state variables and the control surfaces deflections.

Now, given a certain equilibrium flight condition, Eq. **(171)** can be easily linearized to obtain equation **(172)**, where $\delta\eta_i$ with $i = 1,...,n$ represent the displacements of the generalized coordinates around their equilibrium values and, similarly, δu_j with $j = 1,...,m$ are the perturbations of each control surfaces with respect to the equilibrium deflections.

$$\dot{x} = Ax + Bu;$$
$$x = [\delta\eta_1, \cdots, \delta\eta_n, \delta\dot{\eta}_1, \cdots, \delta\dot{\eta}_n];$$
$$u = [\delta u_1, \cdots, \delta u_m];$$

(172)

Thanks to the Elastic Motion estimator, the measurements of the generalized coordinates are available, moreover the observability of the system is ensured. Being **(172)** provided also of the controllability property, it is allowed to apply a classic *LQ* state feedback control to obtain a proper load alleviation control system.

For the sake of simplicity, an infinite-horizon cost function is chosen (see Eq.**(173)**), to ensure asymptotical stability and the desired performances to the closed-loop system.

$$J = \int_0^\infty \left(x^T Q x + u^T R u \right) dt$$

(173)

As known, Q and R, respectively semi-positive definite and positive definite, are the weighting matrices of the state and the control effort. The minimization of the cost function in **(173)** can be obtained considering the typical proportional control with state feedback reported in Eq.**(174)**,

$$u_{la} = -K \cdot x$$

(174)

where the gain matrix K has the form as in Eq.**(175)**

$$K = R^{-1} B^T P$$

(175)

and the matrix P is the solution of the algebraic Ricatti equation, reported in Eq. **(176)**.

$$A^T P + PA - PBR^{-1} B^T P + Q = 0$$

(176)

While designing the load alleviation control system, it has been neglected the interactions between the rigid body dynamics and the elastic structure, assuming that the attitude control system, not described in this paper, would have taken care of the rigid body state variables, with its specific aims. In the numerical tests, given the aforementioned assumption, the attitude control system it is not considered at all.

4 Numerical Results

4.1 Simulation Model of a Flexible Aircraft

4.1.1 Introduction

The analyses of flight mechanic, the evaluation of performances, as well as the design of the GN&C system, are generally performed using a suitable aircraft's model whose validity is generally limited to the hypothesis of rigid body, while the effects of flexibility are generally considered within the aeroelasticity analyses.

The assumption of rigid body considers constant relative positions of masses composing the aircraft (excluding possible rotating parts).

As known, aeroelasticity studies the interaction between aerodynamic and inertial forces with the structural stiffness of the aircraft. Aeroelastic problems include structural instabilities as flutter, structural loads caused by maneuvers or atmospheric turbulence.

For flexible bodies, stability and controllability analyses shall take into account the effects of flexibility, as well as the interaction between structural dynamics and control system ones.

These issues are generally treated within aeroservoelasticity studies. Specifically, the aerodynamic features, the stability and controllability properties can be strongly affected by the elastic deformations shown by the structure due to external loads.

An uncorrect modelling of these effects leads to a wrong design of some subsystems, as for example the flight control system. Aeroservoelasticity is generally considered a part from the flight mechanic, because of a frequency separation between the structural phenomena and rigid body dynamics. This separation is not valid for some configuration such as for HALE configurations and consequently for HAPD aircraft. For this category of aircrafts, the first structural modes have a frequencial content in the same band of flight mechanic. In this condition is essential to consider in the aircraft modelling, the coupling between rigid body dynamic and stuctural deformation [68].

4.1.2 Model Architecture

Within this thesis, the model of flexible aircraft has been considered as an extension of the model generally used for rigid aircraft (Figure XV), thus the same functional blocks included in the model of a rigid aircraft are included in this new model., but each block introduces in the model or processes a part of information which derives from the instantaneous deformation of the aircraft and takes in account its effects on measurements and actuation

system. The format and the number of variables synthetizing, in discrete values, the distributed information on deformation and its dynamic depends on the specific methodology applied.
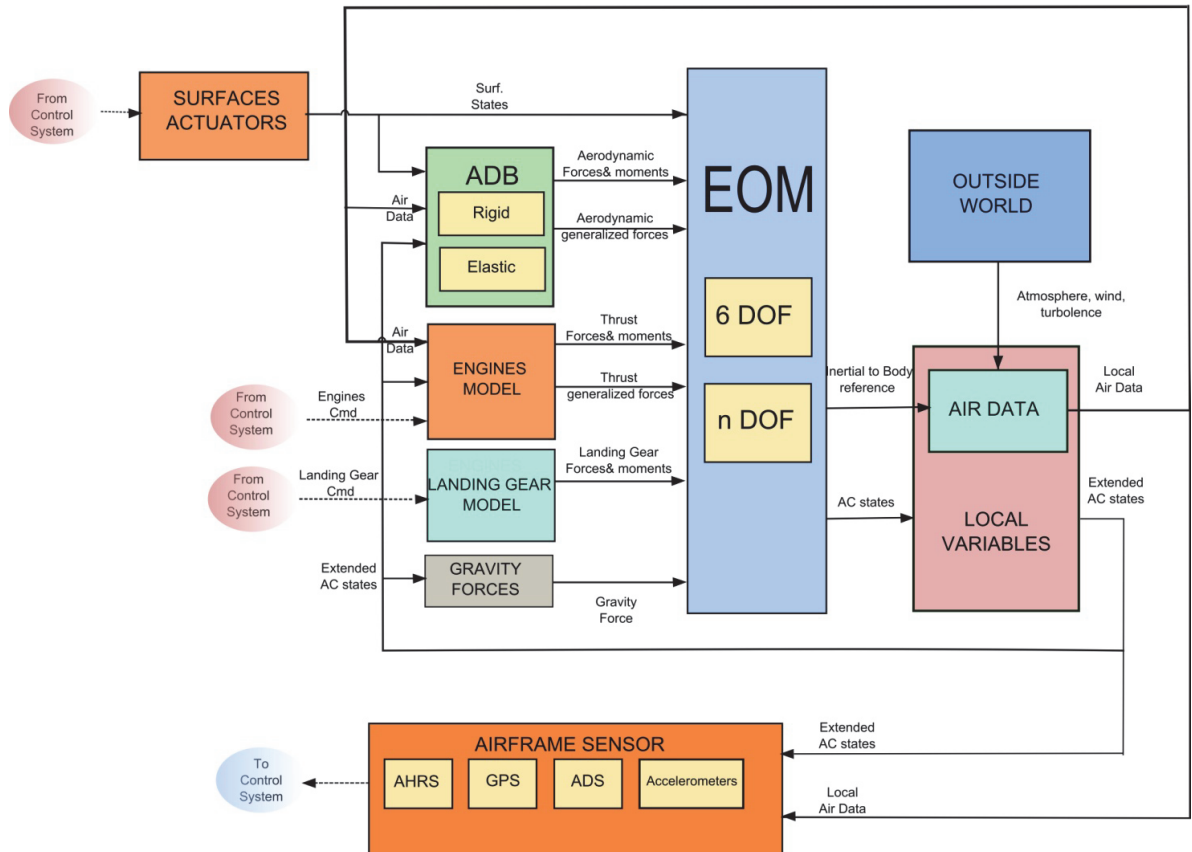
Figure XV High level architecture for the model of elastic aircraft for flight mechanic analyses

The description of blocks is provided in the followings:

1. **EoM**: it includes the equation of flexible aircraft. Under the considered hypotheses, (described later) this block joins a part implementing the rigid body equations (6 DoF) with another one implementing the equations of deformation dynamic (*n* DoF). The output of this block includes the evolution of rigid body and the instantaneous deformation of the aircraft in a discrete way. The input includes the resultant of the external forces and moments, and some variables synthetizing dynamic effects of force distribution on the aircraft deformation.

2. **Gravity Forces**: they provide resultant forces and moments generated by gravitational forces. Furthermore, it also evaluates the effects on deformation of these forces.

3. **ADB**: it is an aerodynamic database including flexible effects. As input, it receives the variables describing the aircraft rigid motion and the instantaneous deformation and speed of deformation of the aircraft. It provides as output the effects of this

deformation on resultant aerodynamic forces and moments with the consequent aerodynamic effects.

Several issues are related to the development of a database able to describe the complex interactions between deformations and aerodynamic effects. The implemented aerodynamic model derives from some simplifying hypotheses particularly strong. Considering the modularity of the proposed architecture, in future, a more detailed aerodynamic model could be included.

This database has been realized integrating a rigid aerodynamic database, obtained with typical CFD applications, with an aeroelastic database obtained with traditional methods used in linear aeroelastic analyses.

4. **Engines Model**: it calculates forces and moments generated by the propelling system and the effects of engine's thrust on deformations. As for the aerodynamics forces, also for propelling ones.

   An evaluation of the effects of deformations on engine forces is required. In the model these effects are essentially represented by a modification of both: the application point and the direction of thrust.

5. **Airframe sensor**: it includes all the sensors considered in the examined configuration. In this block sensor dynamics and delay are considered. Unlike a rigid aircraft model, deformations could influence sensor measurements, with for example a lever arm variation.

6. **Surfaces Actuator**: it implements the dynamics of the actuation systems moving the control surfaces.

7. **Outside World**: it provides the environmental information of the external world. This information includes wind, turbulence and atmospheric properties. This information is elaborated in the block Air Data which elaborates the variables used in the remaining blocks.

At a high level, the system receives as input the commands to the control surfaces and to the engines and provides as output the extended state of the aircraft, including variables which describe the deformation. It also provides as output measurements of the considered sensors.

4.1.3 Hypotheses and Validity of the model

In this paragraph, the main hypotheses, at the basis of the proposed model, will be briefly discussed.

Some of these hypotheses derive from the need to limit the field of applicability to the examined aircraft, avoiding useless complications. Specifically, the validity of the model is limited to an aircraft whose deformations are sufficiently limited so that the theory of linear elasticity could be applied.

Other hypotheses derive from the need to use some assessed methods without using a completely original theory. This concept is valid, for example, for the aerodatabase.

These hypotheses don't limit the field of applicability, but remove the need of method validation, required for new theories.

The aerodinamic theory chosen for this model is limited to a low subsonic regime, in agreement with the demands of HAPD project.

The proposed model can be used for flight mechanic performances evaluation as well as for the design and the analisys of a GN&C system for an aircraft whose structural stiffness can guarantee the validity of the linear elastic theory and which flies at a low subsonic speed.

The followig hypotheses have been considered in the formulation of equations describing the motion of a flexible aircraft:

<u>Hp 1</u> The inertial matrix has been considered variable respect to elastic deformations.

<u>Hp 2</u> The linear elastic theory has been considered valid

The equations are written in a general formulation valid for bodies with a variable inertial matrix. The hypothesis Hp 2 is related to the small value assumed by the deformations and can be considered valid because of the value considered for structural stiffness.

This hypothesis allows to use the principle of superposition for deformations and consequently to apply a modal decomposition to describe the aircraft deformation.

The modal decomposition is the method used to describe a spatial phenomenon, as the deformation of a solid body, with an infinite (in principle) number of variable. For implementation issues this number is considered finite. The accuracy of solution is guaranteed by the choice of a suitable number of variables.

The following hypotheses have also been considered in formulation of the aerodynamic model

<u>Hp 3</u> It is supposed to be valid the linear superimposition between stationary aerodynamic due to rigid body and the aerodynamic depending on vibrational modes.

<u>Hp 4</u> The aerodynamic due to vibrational modes is supposed to be quasi-stationary.

<u>Hp 5</u> Inertial effects due to control surfaces movements are neglected.

Hp 3 is justified by the need to employ assessed computational techniques. It implies that the aerodynamic forces depend linearly on the elastic deformations. The constant coefficients

expressing this linear dependence are determined using a linear model realized for other purposes (as for example flutter analysis).

Hp 4 derives from the analysis of coefficients related to instationary effects, which can be considered negligible.

Within the validity of Hp 5, the movement of control surfaces has effect only on the aerodynamic forces.

The aerodynamic model, built on the basis of Hp 3, is the integration of two different database: a first one based on the hypothesis of rigid body, which is non linear; and a second one whih is elastic and linear. Both these database are realized using computational techniques.

The following hypotheses have been considered respectively for engines, sensors and actuators.

Hp 6 The thrust generated by each engine is considered as a force concentrated in a point.

Sensor and actuator Hypotheses

Hp 7 Sensors are modeled as a first order linear system.

Hp 8 Actuators are modeled as a second order linear system.

4.1.4 Dynamic Equations for the flexible aircraft
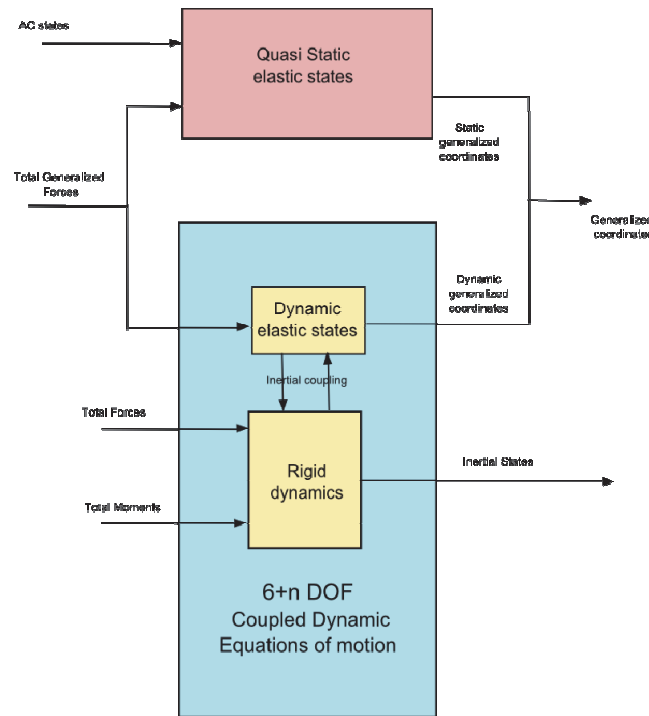
Figure XVI EoM block Architecure

The EoM block includes the equations of the flexible aircraft. These equations are formulated starting from the Hp2. Aircraft motion is represented by a rigid motion of a non inertial reference frame chosen with the constraint that elastic deformations could be considered "of limited entity". The position of an elementary particle is represented by Eq.**(177)** (Figure XVII).

$$\boldsymbol{R}(x, y, z, y) = \boldsymbol{R_0}(t) + \boldsymbol{r}(x, y, z, t) = \boldsymbol{R_0}(t) + \boldsymbol{q}(x, y, z, t) + \widetilde{\boldsymbol{r}}$$

(177)
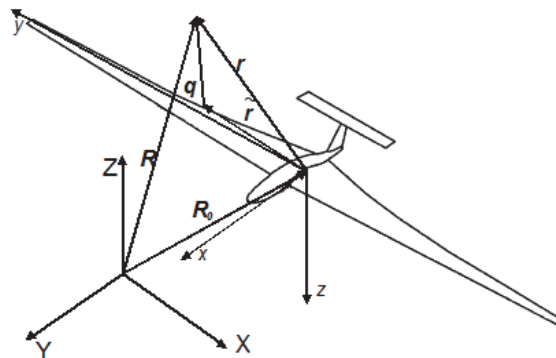
Figure XVII Particle's position in Tangent Reference frame

Equations of flexible vehicle are derived using a modal decomposition of elastic displacements. (Eq.**(178)**) .

$$q = \sum_{i=1}^{\infty} \Phi_i(x, y, z) \cdot \eta_i(t)$$

$$(178)$$

The space depending functions ϕ_i are defined "*mode shapes*", while the time depending functions η_i are defined "*generalized coordinates*". The sum in Eq. **(178)** ends at a predefined value n

Mode shape functions are derived from structural analysis performed for the unconstrained aircraft, excluding rigid motions. Under this hypothesis, deformations are referred to a particular reference frame, defined "*mean axes*", which guarantees the maximum inertial decoupling between the equation set describing rigid motion and the set of equations describing deformation.

The general expression for a variable inertia matrix is reported in Eq. **(179)**.

$$\mathbf{I} = \mathbf{I_0} + \sum_{k=1}^{n} \mathbf{J}^{(k)} \eta_k + \sum_{m,n=1}^{n} \mathbf{J}^{(m,n)} \eta_m \eta_n$$

$$(179)$$

Considering that for the specified aircraft HAPD, the variation of inertia matrix due the deformation is neglectable, J coefficients are equal to zero.

In Eq.**(180)** one has summarized the equations of motions in the aircraft reference frame as implemented in the EoM block.

$$
\left\{
\begin{aligned}
& M(\dot{u} - rv + qw + g\sin\vartheta) && = F_x \\
& M(\dot{v} - pw + ru + g\sin\varphi\cos\vartheta) && = F_y \\
& M(\dot{w} - qu + pv + g\cos\varphi\cos\vartheta) && = F_z \\
& I_{xx}\dot{p} - I_{xy}\dot{q} - I_{xz}\dot{r} + (I_{zz} - I_{yy})qr + (I_{xy}r - I_{xz}q)p + (r^2 - q^2)I_{yz} + \dot{I}_{xx}p - \dot{I}_{xy}q - \dot{I}_{xz}r && = M_x \\
& I_{yy}\dot{q} - I_{yx}\dot{p} - I_{yz}\dot{r} + (I_{xx} - I_{zz})pr + (I_{yz}p - I_{xy}r)q + (p^2 - r^2)I_{xz} + \dot{I}_{yy}q - \dot{I}_{xy}p - \dot{I}_{yz}r && = M_y \\
& I_{zz}\dot{r} - I_{zx}\dot{p} - I_{zy}\dot{q} + (I_{yy} - I_{xx})pq + (I_{xz}q - I_{yz}p)r + (q^2 - p^2)I_{xy} + \dot{I}_{zz}r - \dot{I}_{zx}p - \dot{I}_{zy}q && = M_z \\
\\
& M_i\ddot{\eta}_i + \zeta_i\dot{\eta}_i + M_i\omega_i\eta_i + \frac{1}{2}(J_{xx}^{(i)}p^2 + J_{yy}^{(i)}q^2 + J_{zz}^{(i)}r^2 - J_{xy}^{(i)}pq - J_{xz}^{(i)}pr - J_{yz}^{(i)}qr) + \ldots \\
& \qquad \ldots + \frac{1}{2}\sum_{k=1}^{n}(J_{xx}^{(k)}p^2 + J_{yy}^{(k)}q^2 + J_{zz}^{(k)}r^2 - J_{xy}^{(k)}pq - J_{xz}^{(k)}pr - J_{yz}^{(k)}qr)\eta_k = Q_i
\end{aligned}
\right.
$$

$$(180)$$

In addition to these equations, equations of attitude kinematic have to be also considered (Eq.**(181)**).

$$
\begin{cases}
\dot\vartheta \sin\psi - \dot\phi \sin\vartheta \cos\psi = p \\
\dot\vartheta \cos\psi + \dot\phi \sin\vartheta \cos\psi = q \\
\dot\phi \cos\vartheta + \dot\psi = r
\end{cases}
$$

(181)

In the previous equations, moments of inertia derivatives have to be calculated according to Eq. **(179)**.

The first six equations in Eq. **(180)** are coincident with the standard equations describing the motion of a rigid body, in which the coupling (represented by the moments of inertia derivatives) with elastic deformations has been included.

In the remaining n equations, which are second order linear differential equations, some structural parameters appear. They are: the generalized masses M_i ; frequencies of vibration ω_i; structural damping ζ_i and other remaining terms which represent the coupling with the rigid body dynamic (these last terms are null if the inertia matrix is considered constant, they are anyway neglectable with respect to angular speed). All these terms depend on masses distribution and on mode shape functions.

The n-DOF block is parametrically implemented, according to the technique of the "residual stiffness". This technique considers more important the dynamics of vibrational modes with a lower frequency, while it considers instantaneously the higher frequency modes. Thus the evolution of the first *ndyn* modes is described with a second order dynamic, while for the remaining *nstat=n-ndyn* are evaluated from a simple algebraic system, in which generalized coordinates are evaluating as linear functions of the generalized forces by inversion of stiffness matrix conveniently residualized.

$$
\begin{bmatrix}
\eta_{ndyn+1} \\
\ldots \\
\eta_n
\end{bmatrix} = \widetilde{K}^{-1} \cdot Q
$$

(182)

The number of modes to be taken into account in the dynamic of the aircraft is to be defined during the inizialization of the model.

The final state of the implementated model is reportes in Eq.**(182)**.

$$
x = \begin{pmatrix} x_{cg} & y_{cg} & z_{cg} & u & v & w & \varphi & \vartheta & \psi & p & q & r & \eta_1 \ldots \eta_{ndyn}, \dot\eta_1 \ldots \dot\eta_{ndyn} \end{pmatrix}
$$

(183)

The output includes the state associated with the statically evaluated modal coordinates.

Other interesting variables are calculated within the block 6-DoF, as for example the DCM between the body reference frame and the inertial one (allthe variables calculated in this block are reported in Table 5).

Inputs are the resultant forces and moments, which appear in the first six equations; and the generalized forces. These latter are defined as the virtual work done by external applied forces with respect to displacements defined by each mode shape. Generalized and resultant forces and moments are calculated in the module relative to the system which has generated them (Engine, ADB).

Input	*Total Forces, Total Momement*
States	$x_{cg}, y_{cg}, z_{cg}, u, v, w, \varphi, \vartheta, \psi, p, q, r, \eta_{dyn}, \dot{\eta}_{dyn}$
Output	$x_{cg}, y_{cg}, z_{cg}, u, v, w, \varphi, \vartheta, \psi, p, q, r, V_{ground}, \gamma$ **,track,climb_rate,** $a_{Xcg}, a_{Ycg}, a_{Zcg}, \dot{p}, \dot{q}, \dot{r}, M$ **,DCM,**$\eta = \left(\eta_{dyn}, \eta_{stat} \right)$
Parameters	$M, M_i, \zeta_i, \omega_i,$ **I,J$^{(i)}$,J$^{(m,n)}$**

Table 5 Main Features of EoM block

4.1.5 AeroDatabase
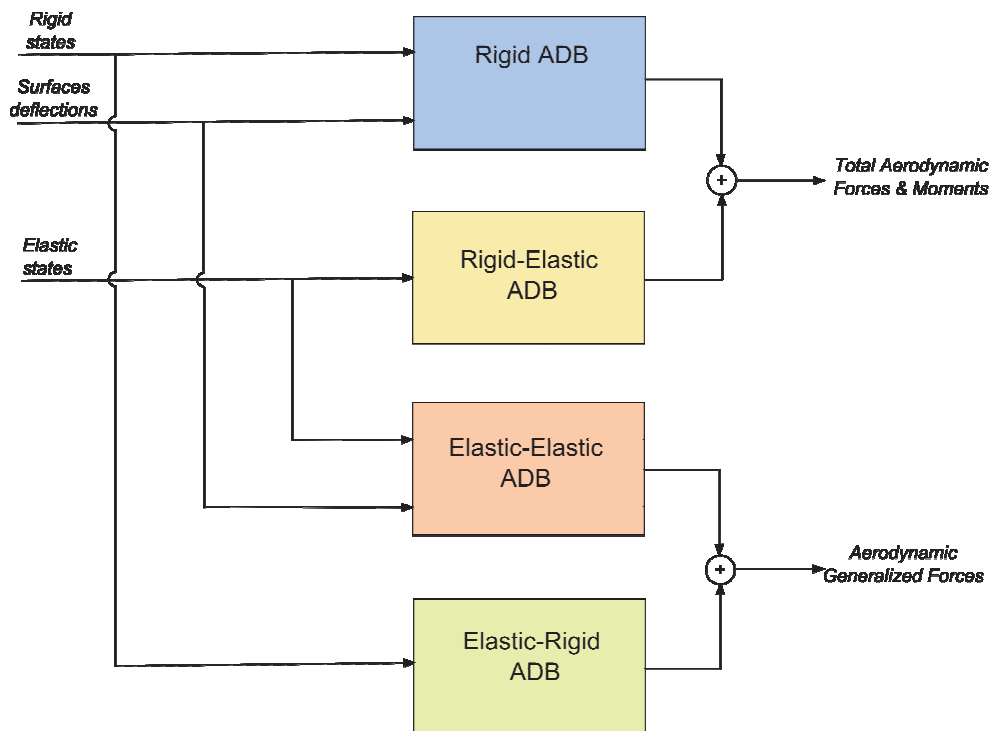
Figure XVIII Architecture of the ADB block

The aerodynamic laws considered within the model of flexible aircraft are based on a simplified methodology which allows using data already available and obtained using assessed aerodynamic tools. Specifically, results provided by CFD analysis for determining the aerodatabase of the rigid aircraft are integrated with the results obtained from the linear aeroelastic analysis.

The aerodatabase has the following structure:

$$L = \frac{\rho V_0^2 S}{2} C_L(\alpha,\beta,p,q,r,\delta_{\sup}) + \frac{\rho V_0^2 S}{2} \sum_{i=1}^{n} C_{L\eta_i}\eta_i + \frac{\rho V_0^2 S\bar{c}}{2} \sum_{i=1}^{n} C_{L\dot{\eta}_i}\dot{\eta}_i$$

$$D = \frac{\rho V_0^2 S}{2} C_D(\alpha,\beta,p,q,r,\delta_{\sup}) + \frac{\rho V_0^2 S}{2} \sum_{i=1}^{n} C_{D\eta_i}\eta_i + \frac{\rho V_0^2 S\bar{c}}{2} \sum_{i=1}^{n} C_{D\dot{\eta}_i}\dot{\eta}_i$$

$$Y = \frac{\rho V_0^2 S}{2} C_Y(\alpha,\beta,p,q,r,\delta_{\sup}) + \frac{\rho V_0^2 S}{2} \sum_{i=1}^{n} C_{Y\eta_i}\eta_i + \frac{\rho V_0^2 Sb}{2} \sum_{i=1}^{n} C_{Y\dot{\eta}_i}\dot{\eta}_i$$

$$M = \frac{\rho V_0^2 S\bar{c}}{2} C_m(\alpha,\beta,p,q,r,\delta_{\sup}) + \frac{\rho V_0^2 S\bar{c}}{2} \sum_{i=1}^{n} C_{m\eta_i}\eta_i + \frac{\rho V_0^2 S\bar{c}^2}{2} \sum_{i=1}^{n} C_{m\dot{\eta}_i}\dot{\eta}_i$$

$$\bar{L} = \frac{\rho V_0^2 Sb}{2} C_l(\alpha,\beta,p,q,r,\delta_{\sup}) + \frac{\rho V_0^2 Sb}{2} \sum_{i=1}^{n} C_{l\eta_i}\eta_i + \frac{\rho V_0^2 Sb^2}{2} \sum_{i=1}^{n} C_{l\dot{\eta}_i}\dot{\eta}_i$$

$$N = \frac{\rho V_0^2 Sb}{2} C_n(\alpha,\beta,p,q,r,\delta_{\sup}) + \frac{\rho V_0^2 Sb}{2} \sum_{i=1}^{n} C_{n\eta_i}\eta_i + \frac{\rho V_0^2 Sb^2}{2} \sum_{i=1}^{n} C_{n\dot{\eta}_i}\dot{\eta}_i$$

$$Q_{\eta_i} = \frac{\rho V_0^2 S\bar{c}}{2}(C_0^i + C_\alpha^i\alpha + C_\beta^i\beta + C_p^i p + C_q^i q + C_r^i r + C^i{}_{\delta_{\sup}}\delta_{\sup} + \sum_{j=1}^{n} C^{ij}{}_\eta\eta_i) + \frac{\rho V_0^2 S\bar{c}^2}{2} \sum_{i=1}^{n} C^{ij}{}_{\dot{\eta}}\dot{\eta}_i$$

(184)

The nonlinear terms are described by suitable look-up table included in the non-linear database derived under the hypothesis of rigid configuration. The constant coefficient of the linear terms are derived, short of a reference frame transformation, from the linear aeroelastic model.

These coefficients are derived, within the aeroelastic analysis, for a specific flight condition. In principle their validity is limited to a little variations of this flight condition. To extend their applicability, it is required a sort of interpolation between their values at different flight condition.

The database is implemented in four distinct blocks, as shown in Figure XVIII. The block labelled Rigid-ADDN includes the nonlinear part of the aerodynamic model depending on the rigid body variables (α,β,p,q,r).

The other three blocks are totally linear and they include the constant parameters derived from a linearized model of the deformed body aerodynamic. The block labelled Rigid-Elastic ADB includes the coefficients, which describe the effect of elastic modes on the resultant forces and moments. The block labelled Elastic-ADB includes the coefficients describing the mutual aerodynamic effect among elastic modes. The last one, labelled Elastic-Rigid ADB represents the effect of rigid state variables on elastic modes. The effect of control surfaces on elastic modes has been included in the block Elastic-ADB.

Input	$\alpha, \beta, p, q, r, \eta_1, \ldots, \eta_n, \dot{\eta}_1, \ldots, \dot{\eta}_n, \delta_{\sup}$
Output	$L, D, Y, M, \bar{L}, N, Q_{\eta_i}, \ldots, Q_{\eta_n}$
Parameters	$C_L, C_D, C_Y, C_m, C_l, C_n$ *(look up table)*
	$C_{L\eta_i}, C_{L\dot{\eta}_i}, C_{D\eta_i}, C_{D\dot{\eta}_i}, C_{Y\eta_i}, C_{Y\dot{\eta}_i}, C_{l\eta_i}, C_{l\dot{\eta}_i}, C_{n\eta_i}, C_{n\dot{\eta}_i},$
	$C_0^{\ i}, C_\alpha^{\ i}, C_\beta^{\ i}, C_p^{\ i}, C_q^{\ i}, C_r^{\ i}, C^i_{\delta_{\sup}} \qquad per \quad i = (1 \ldots n)$
	$C^{ij}_\eta, C^{ij}_{\dot{\eta}} \qquad per \quad i, j = (1 \ldots n)$

Table 6 Main Features of ADB block

4.1.6 Propelling System
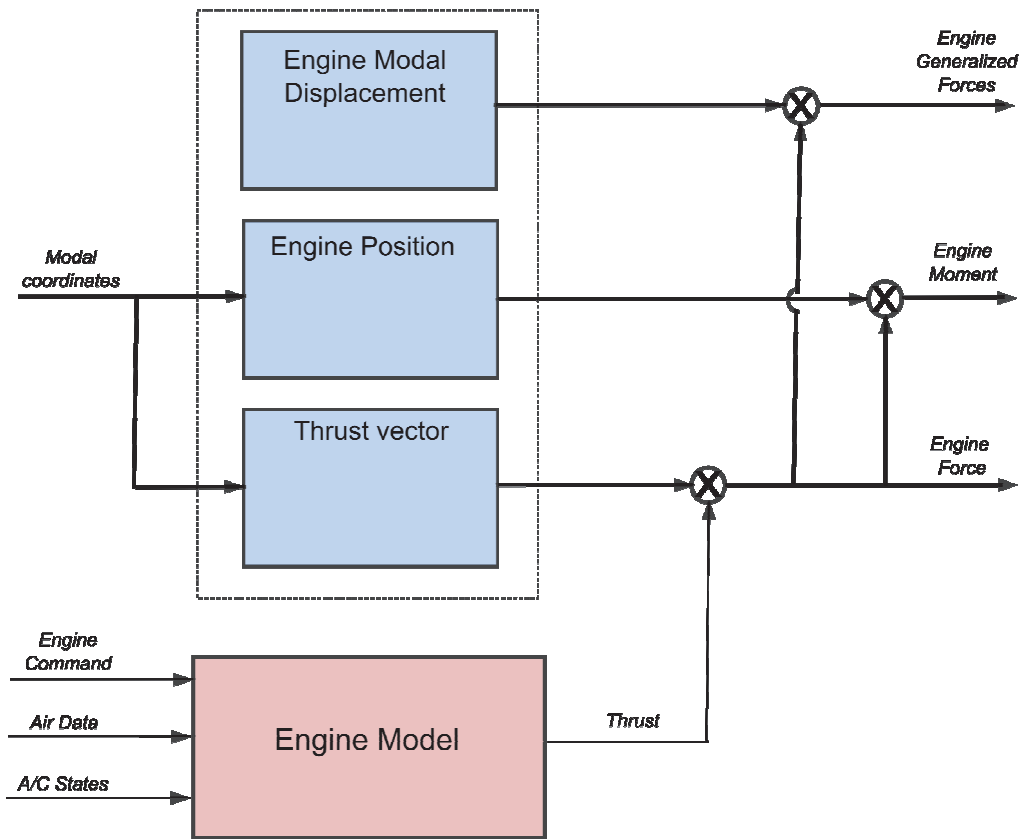
Figure XIX Architecture of the Propelling System block

Figure XIX represents the architecture of the model of a single engine. The kernel of the propelling system model is the block *Engine Model* which describes the dynamic of the engine coupled with the propeller.

The other blocks "*Thrust Vector*", "*Engine Position*" and "*Engine Modal Displacement*" receive as input the modal coordinates which represent a synthetic description of the instantaneous deformation. These coordinates are used to determine the actual direction of the thrust and consequently the thrust vector generated by each engine; the momentum generated

by this vector with respect to the aircraft center of gravity and the contribution provided by each engine to the generalized forces for each one of the vibrational mode.

The generalized forces are defined as in Eq.**(185)**

$$\boldsymbol{Q}_i = \int_V \boldsymbol{\Phi}_i \cdot \boldsymbol{F}_V \, dV - \int_S \boldsymbol{\Phi}_i \cdot \boldsymbol{F}_S \, dS$$

(185)

Where Q_i is the generalized force, ϕ_i is the ith mode shape and F_s and F_v are respectively the distribution of volume forces and superficial forces. The thrust contribution, supposed to be concentrated in a point, to the ith generalized force is expressed in Eq. **(186)**.

$$\boldsymbol{Q}_{Ti} = \boldsymbol{T} \cdot \boldsymbol{\Phi}_i(\widetilde{r}_i) \eta_i$$

(186)

Where $\widetilde{r}_i$ is the nominal position of the thrust application point in the body reference frame.

In addition to the generalized coordinates, these blocks need, as input, also some information about the local deformation of the engine position, that depends on the value of mode shape functions in the thrust application point and on the rotation of this point (Jacobian of mode shape functions calculated in the application point of thrust). This information is transmitted to the blocks as parameters, as highlighted in the related tables.

In Figure XX we have represented with greater detail the block Engine Model.
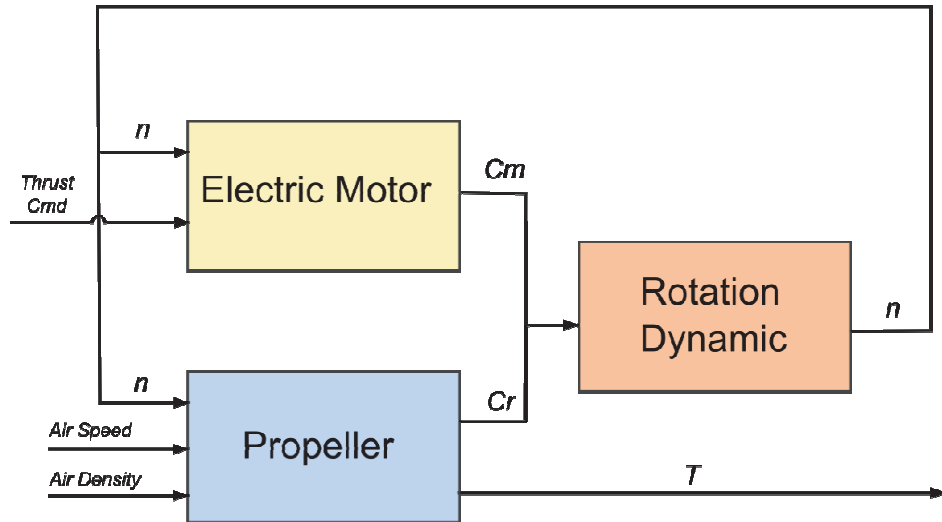
Figure XX Architecture of the Engine Model block

The block *Electric Motor* implements the power curve as a function of engine command δT and the number of revolutions *n*, from which the torque: can be derived:

$$C_m = C_m(n, \delta_T)$$

(187)

The block propeller includes the information of the propeller aerodynamic. This information, represented by thrust and power coefficients, is included in look-up tables as function of the advance ratio $J = \dfrac{V}{nD}$.

In the last block *Rotation Dynamic*, the axis' equilibrium equation is implemented and it determines dynamically the revolution number using the following Eq. **(188)**

$$I_r \ \dot{n} + b \ n = C_m - C_r$$

(188)

This block requires the knowledge of the rotational inertia of the group engine-propeller and the friction coefficient.

Input	***Thrust Cmnd, Air Speed, Air Density***
Output	***Thrust, n***
Parameter	$C_T(J), C_p(J)$ I_r, b

Table 7 Main Features of Engine Model block

Input	$\eta_1, \ldots, \eta_n$
Output	***Versore della spinta***
Parameter	$\Phi_1(\widetilde{r}), \ldots, \Phi_n(\widetilde{r})$

Table 8 Main Features of Thrust Vector block

Input	$\eta_1, \ldots, \eta_n$
Output	***Posizione del punto di applicazione della spinta ($\widetilde{r}$)***
Parameter	$\Phi_1(\widetilde{r}), \ldots, \Phi_n(\widetilde{r})$

Table 9 Main Features of Engine Position

Output	Q_{Ti}
Parameter	$\Phi_1(\widetilde{r}), \ldots, \Phi_n(\widetilde{r})$

Table 10 Main Features of Engine Modal Displacement block

4.1.7 Gravitational Forces block

This block calculates the gravitational force in the body reference frame. It receives as input the Euler's angle.

Input	φ, ϑ, ψ
Output	***Gravity force***
Parameter	***g, Mass***

Table 11 Main Features of Gravity Forces block

4.1.8 AirData block

It receives as input the model of the atmosphere, wind, turbulence, sound speed in body reference frame and DCM. As output it provides true Airspeed, angles of attack and sideslip, Mach number, dynamic pressure, total pressure and calibrated airspeed.

4.1.9 Outside World

This block calculates components of wind speed, turbulence and physical properties of air such as static temperature and pressure; total pressure etc. This information will be provided to the AirData block. The realized model allows calculation of wind speed in the body reference frame as a function of altitude. This calculation is performed through statistical analyses. The input variables are: aircraft altitude h included in aircraft state vector and the aircraft speed (including the wind but excluding the turbulence). The output variables are wind speed components in North, East and Up direction; the components of perturbations in turbulence; static pressure, air density, static temperature and speed of sound.

4.2 Experimental Tests for determination of Inertial Sensors Parameters

4.2.1 Introduction

An inertial measurement unit is typically composed by three different sensors:

- accelerometers,
- gyroscopes,
- magnetometers.

MEMS technology has lead to realization of sensors with very reduced weight, size and cost. These features are extremely important because they allow to use MEMS sensors in aerospace applications, especially in the field of unmanned air vehicles, where the main requirement is the reduction of costs, weights and sizes of the onboard equipments, even if they have lower performances than traditional ones (i.e FOG/Laser gyros).

MEMS sensors are subject to different sources of error, which can be classified according to their deterministic or stochastic nature (Table 12).

Deterministic Sources	Stochastic Sources
Calibration	Thermal / Mechanical Noise
Temperature	Electronic Noise
Acceleration (Gyros)	
Magnetic/Electric sources (Magnetometers)	

Table 12 Sources of Error for Inertial Sensors

The output of a MEMS sensors can be expressed as a sum of different terms:

$$\widetilde{y} = (1 + SF) \times y^t + b_0 + b_T(T) + b_1(t) + b_\mu(t)$$

(189)

$\tilde{y}$: *measured quantity*
y^t : *true quantity*
SF : Calibration Scale Factor
b_o : *Calibration Bias*
b_T : *Temperature dependent Bias*
b_1: *Stochastic Bias*
b_μ : *Noise*

Laboratory tests and mathematical theories are useful to characterize and quantify these sources of error.

By knowledge of the different sources of error it is possible to characterize the overall accuracy of the sensor and thus to choice the best sensor for the desired application. Moreover error characterization is required to realize a simulation model which reproduces, as much as possible, the real behavior of the sensor.

The purposes of tests, treated in this chapter, are the realization of a faithful simulation model of an IMU to include in the aircraft global simulation environment and the determination of the dynamical model parameters to use in navigation Kalman filter.

The following lines give basic explanations about the method to identify all components of the sensor error model.

- The b_0 component can be obtained by taking long term data when the sensor is subjected to a zero input. The average of this long term data will be b_0. This value is sometimes indicated on datasheets for the inertial sensors. However, this value isn't often constant, that's why the value can be verified by performing a laboratory test. Nevertheless, it isn't sure that the signal input is really to zero, in other words, it's important to take in account the Earth's rotation and the Earth's gravity which can modify the measurement. The first one can have an impact on the angular rate measurements and the second one on the acceleration measurements. Regarding the rotation of the Earth, we can assume that is insignificant. Regarding the Earth's gravity, in the event that the z-axis of the unit isn't along the Earth's gravity axis (and in consequence the x and y-axes not orthogonal with the Earth's gravity axis) some components will be measured by the accelerometer and will corrupt the bias estimation. That's why a specific algorithm can be used in order to perform the estimation of the b_0 bias and the scale factor (SF) by taking into account the measurement of the Earth's gravity.

- The $b_1(t)$ component is difficult to estimate, because of its stochastic character. It's possible to identify a mathematical form of this bias component, but the difficulty is, and what's most important, to find the specific numerical coefficients which are part of the mathematical model. Several techniques are used in order to estimate the model as the identification tools which can be ARX, ARMA, etc. However, these tools can result in mathematical models which are of high orders. Consequently, not suitable for an implementation in an estimator running in real time. That's why, an other method can be used, named "Allan Variance Analysis" [69] ,which can characterize the

stochastic component of $b_1(t)$. The explanations of this last method are explained in the next chapters.

- The $b_2(T)$ component depends on the temperature value of the sensor. It's possible to estimate this bias by taking data when the sensor is subjected to a zero input and a temperature gradient. The plot of the measurement according to the temperature will give the equation of the bias evolution with the temperature. Explanations are provided in the next paragraphs.

It's important to note that this kind of test depends on the time, so $b_0(t)$ and $b_1(t)$ components too. More, the temperature in which the temperature bias is zero isn't the 0°C but generally 25°C (check with the appropriate sensor datasheet). Consequently, this part of this bias isn't the easier to estimate.

- The $b_w(t)$ term is sometimes called "output noise" and can be modelled as band-limited white noise. The band-limit for the $b_w(t)$ is very high relating to the frequency content of $b_1(t)$. Thus, a numerical value for $b_w(t)$ can be obtained by looking at the standard deviation of the sensor output when it is subjected to a zero input and sampled at a rate much higher than the maximum frequency content of $b_1(t)$.

In this thesis, experimental tests for determination of the temperature depending bias and stochastic terms will be described.

All the test have been performed used the Crossbow Micronav Unit, which includes inertial sensors based on the MEMS technology.

4.2.2 Temperature Tests

In general, all sensors are sensitive to a temperature gradient, that is to say, a bias appears in the signal and its amplitude changes with the temperature. That's why a correction must be performed in order to make null the bias evolution with the change of temperature.

In these temperature tests, the IMU has been put in a fixed position and the temperature has been changed.

Unfortunately, the available equipment has allowed us to test the item in a limited range of temperature, but the results are very relevant.

The MNAV100CA unit was put inside an airtight box in order to increase the temperature (thanks to the electronic components). When the stabilized temperature was reached, the airtight box was removed in order to allow the temperature to decrease to the balanced

temperature (between the unit and the ambient air). The unit was subjected to a zero input in order to not disturb the acquisition. Then, it has been possible to determine the model of the temperature bias by plotting the data in accordance with the measured temperature.

In the next figures, the analysis of acceleration evolution according to the temperature provides the equation allowing to perform the compensation (an interpolation technique can be used for the equation estimation).

a) For the X-axis measurement
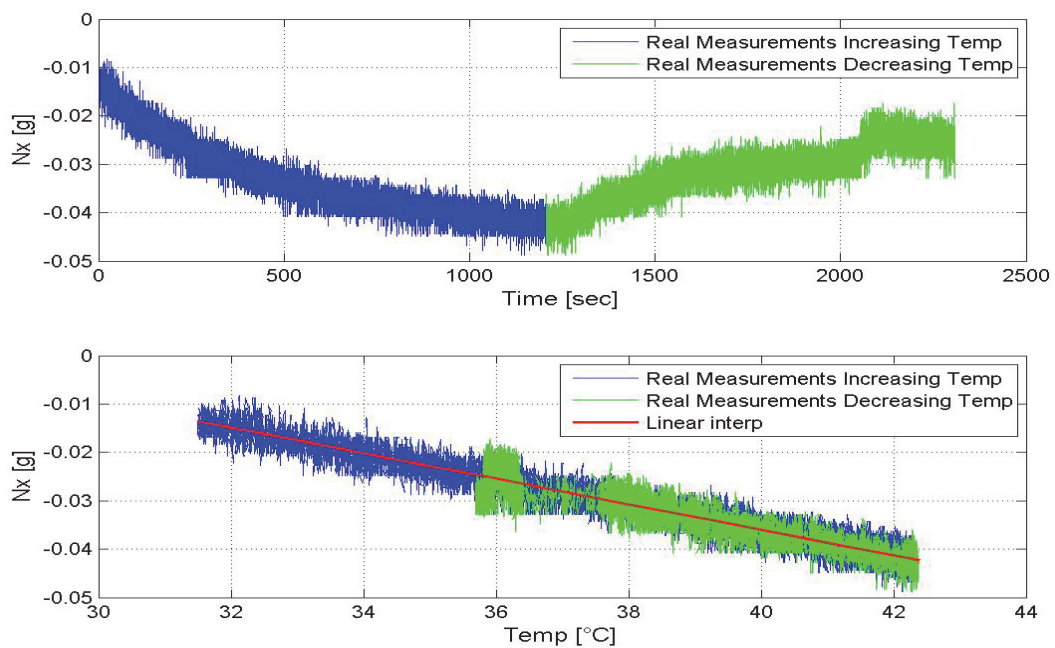
Figure XXI X-axis acceleration variation vs. temperature

In bleu is shown the evolution of the X-axis bias when the temperature is increased and in red when the temperature is decreased. A linear interpolation of these values has been performed (shown in green). It's important to note that the zero bias isn't at the temperature of 0°C but at 25°C for this sort of sensor. That's why the corrective term to perform to the measurement will be: *Correction=-0.0026 x (T[°]-25)*

a) For the Y-axis measurement
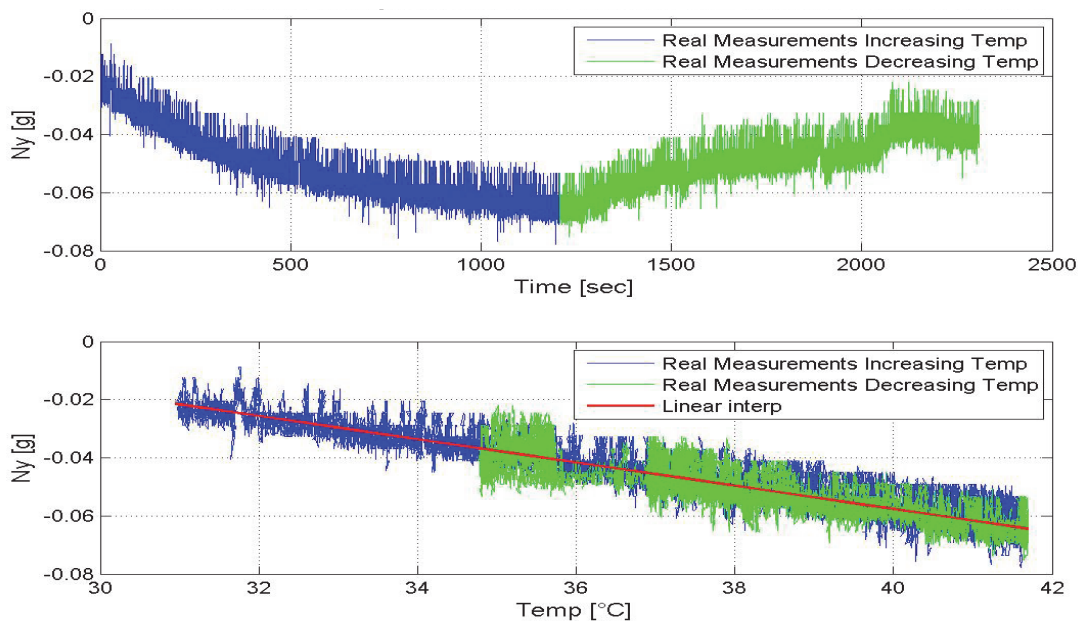
Figure XXII Y-axis acceleration variation vs. temperature

The corrective term becomes: *Correction=-0.004 x (T[°]-25)*

b) <u>For the Z-axis measurement</u>
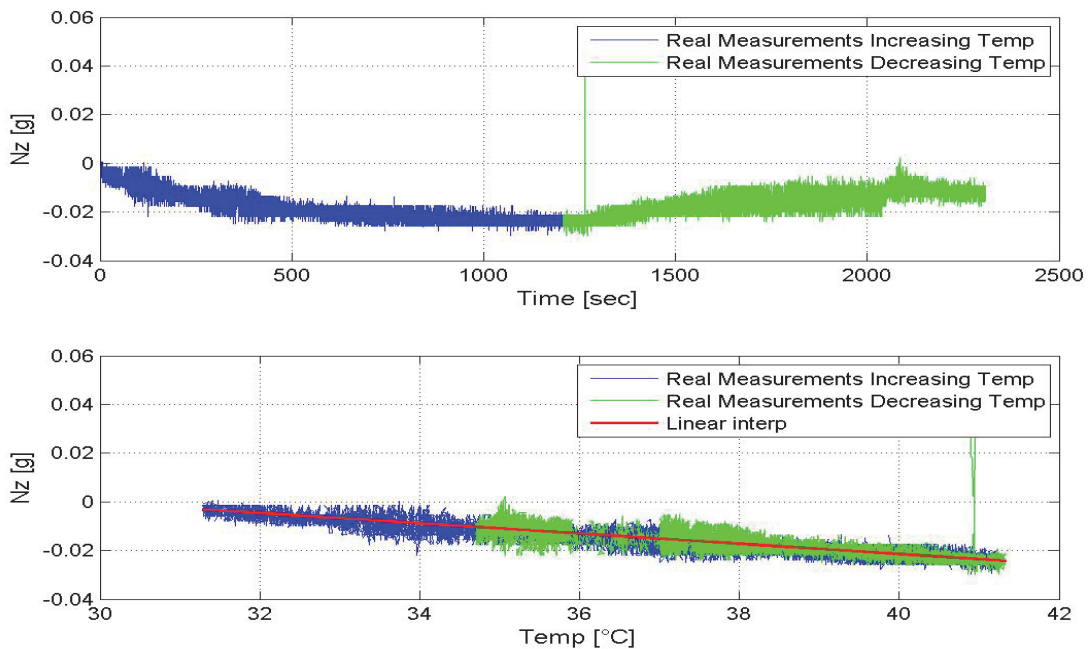
Figure XXIII Z-axis acceleration variation vs. temperature

The corrective term becomes: *Correction=-0.0021 x (T[°]-25)*

There are three sensors mounted on the MNAV100CA for the angular rate measurement. The ADXRS150 from ANALOG DEVICES Company is a 1-axis sensor which is used to measure the angular rate along one MNAV100CA axis.
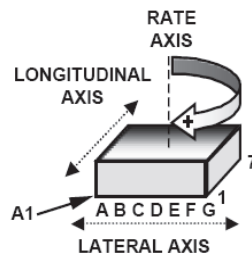
Figure XXIV: ADXRS150 illustration

a) For the X-axis measurement
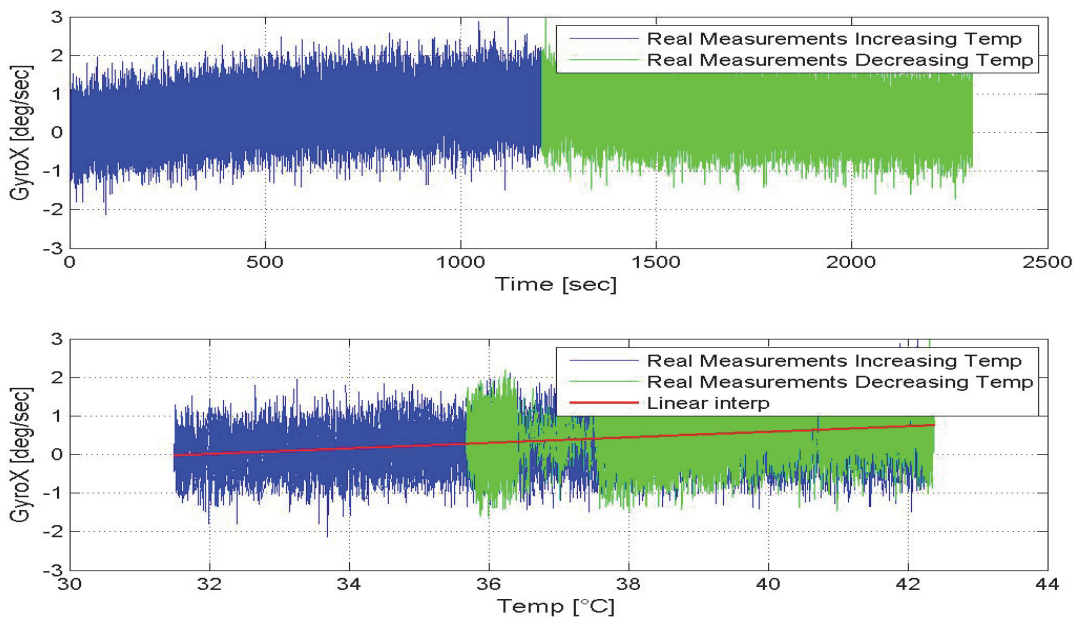
Figure XXV: X-axis angular rate variation vs. temperature

In bleu is shown the evolution of the X-axis bias when the temperature is increased and in red when the temperature is decreased. An interpolation was performed, shown in green. It's important to note that the zero bias isn't at the temperature of 0°C but at 25°C for this kind of sensor. That's why the corrective term to perform to the measurement will be:

Correction=-0.0724 x (T[°]-25)

b) For the Y-axis measurement
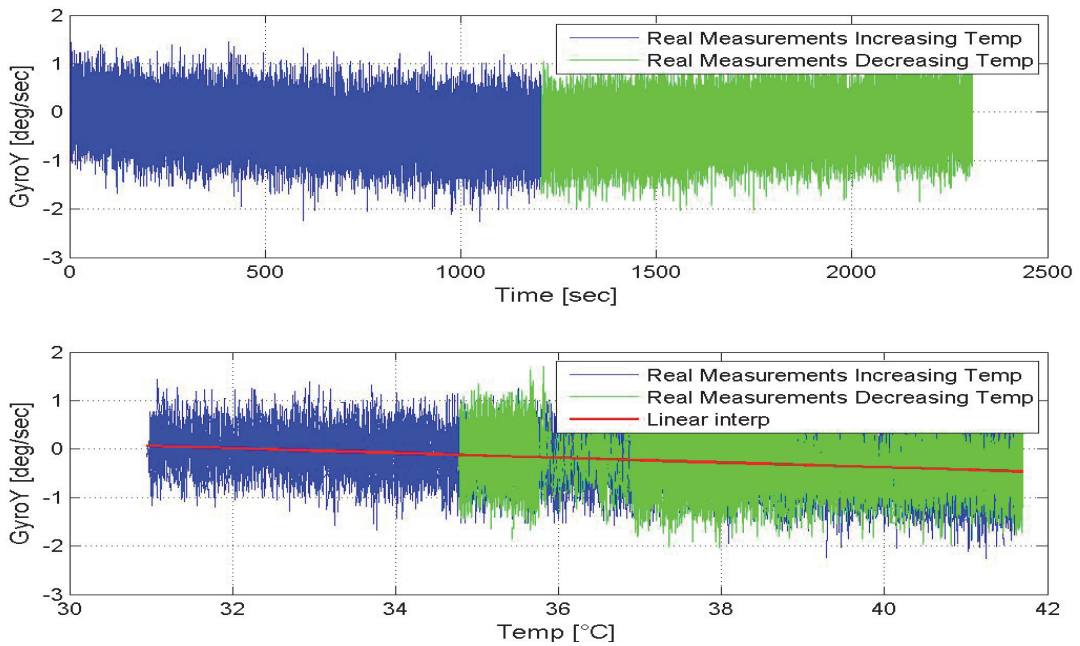
Figure XXVI: Y-axis angular rate variation vs. temperature

The corrective term becomes: *Correction=-0.0494 x (T[°]-25)*
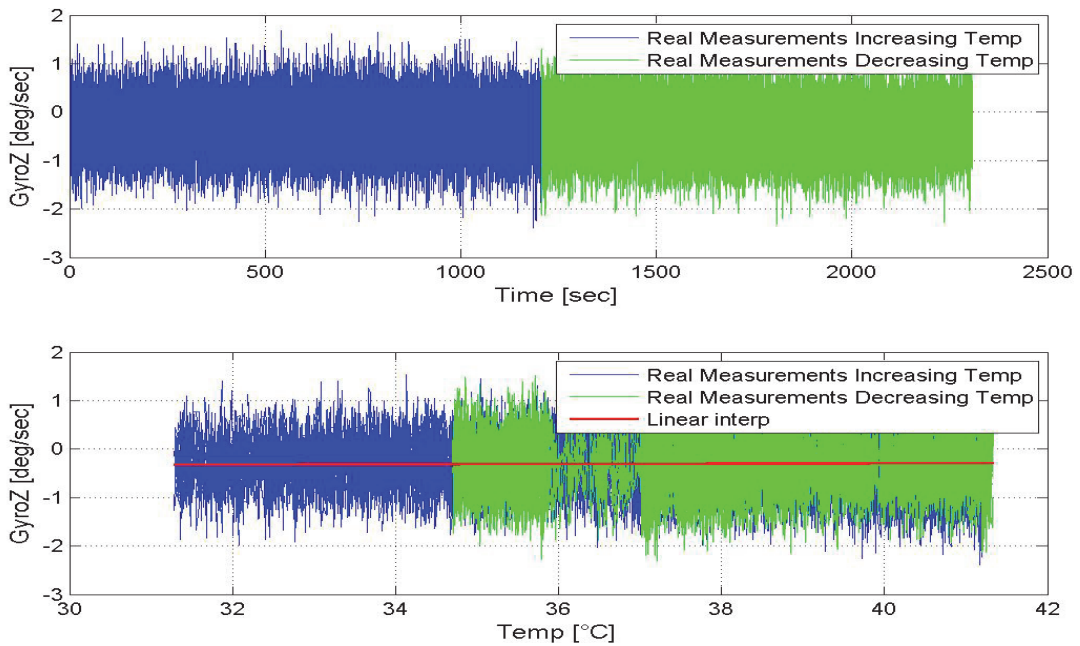
Figure XXVII: Z-axis angular rate variation vs. temperature

The corrective term becomes: *Correction=0.0032 x (T[°]-25)*

Gyroscopes are less sensitive to a temperature variation than accelerometers.

There are two different sensors mounted on the MNAV100CA for the magnetic field measurement.

The first one is the HMC1051ZL from Honeywell Company. It's a 1-axis sensor which is used to measure the magnetic field along the MNAV100CA Z-axis.
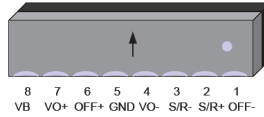
Figure XXVIII: HMC1051ZL illustration

The second and last one is the HMC1052 from Honeywell Company. It's a 2-axis sensor which is used to measure the magnetic field along the MNAV100CA X and Y-axes.
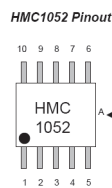
Figure XXIX: HMC1052 illustration

a) For the X-axis measurement
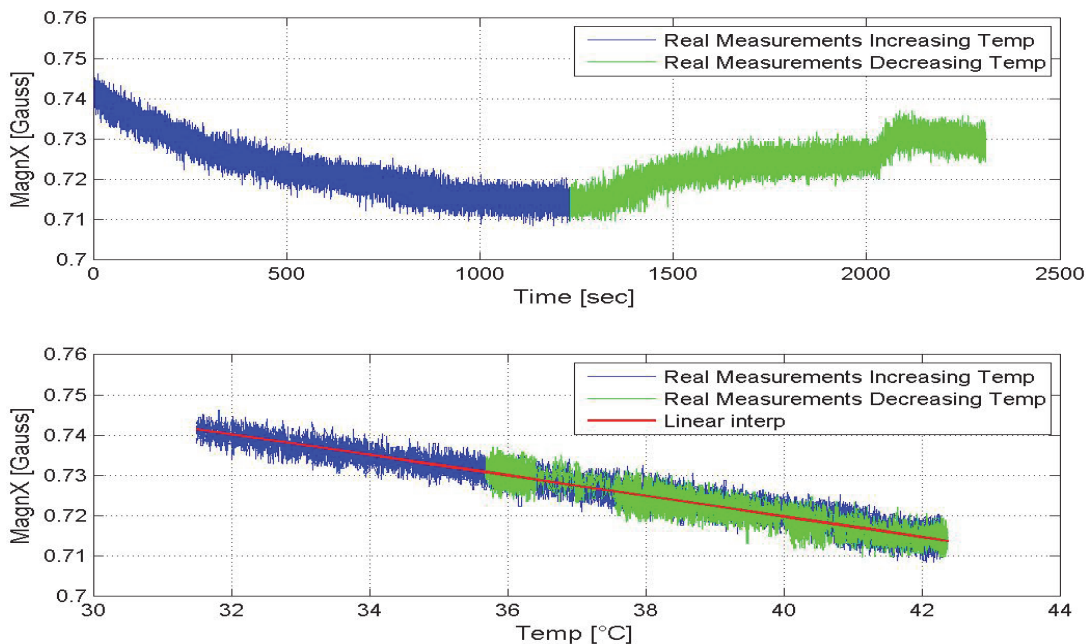
Figure XXX: X-axis magnetic field variation vs. temperature

In bleu is shown the evolution of the X-axis bias when the temperature is increased and in red when the temperature is decreased. An interpolation was performed, shown in green. It's important to note that the zero bias isn't at the temperature of 0°C but at 25°C for this sort of sensor. That's why the corrective term to perform to the measurement will be:

Correction=-0.0025 x (T[°]-25)

b) <u>For the Y-axis measurement</u>
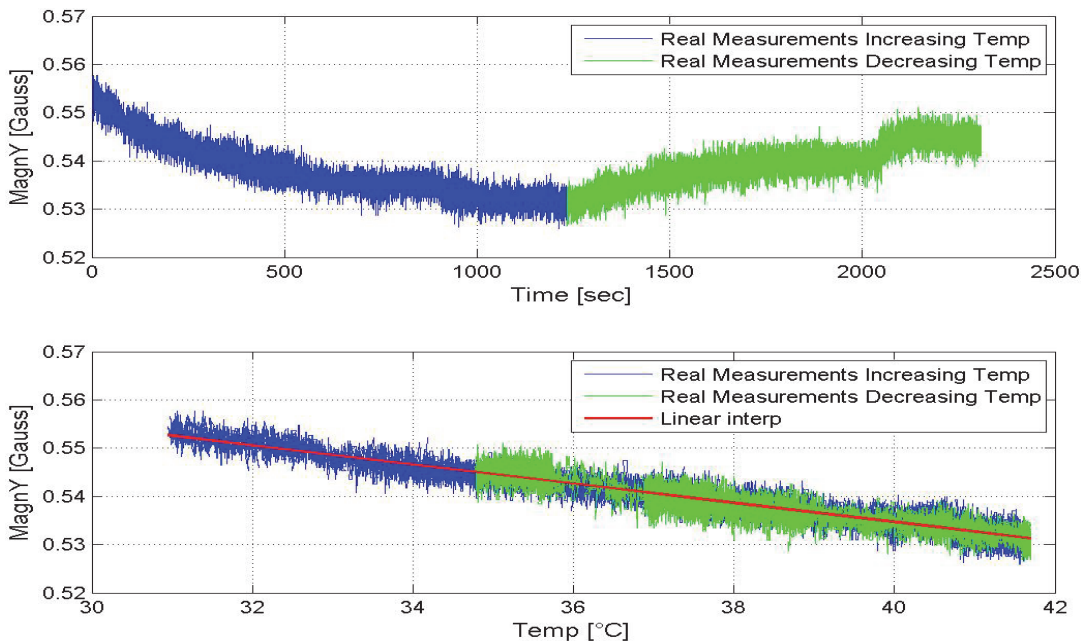
Figure XXXI: Y-axis magnetic field variation vs. temperature

The corrective term becomes: *Correction=-0.002 x (T[°]-25)*

c) <u>For the Z-axis measurement</u>
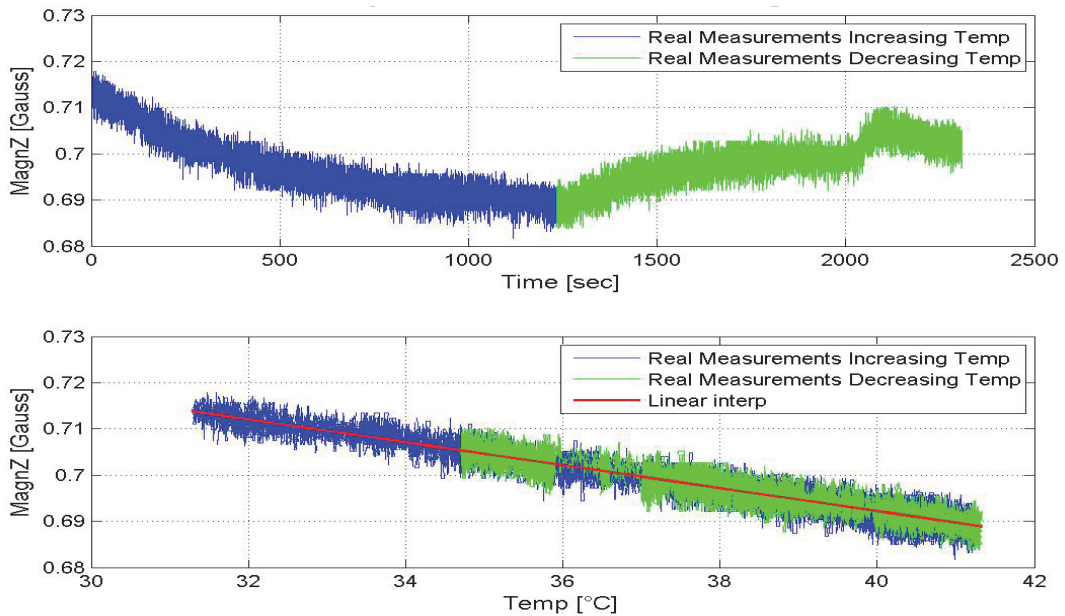
Figure XXXII: Z-axis magnetic field variation vs. temperature

The corrective term becomes: *Correction=-0.0025 x (T[°]-25)*

The obtained results are compatible with the information included in the datasheet of each sensor.

4.2.3 Tests for determination of Allan variance

The Allan variance can be viewed as the time domain equivalent of the power spectrum. Instead of power as a function of frequency it gives power as a function of averaging time.

In order to use this method, let us assume that the time history is a record of inertial sensor outputs (in volts, deg/s, deg/h, g), as a function of time. Let us say that the data was sampled at the rate of Fs Hertz and recorded for T seconds. The total number of recorded data points is, therefore, N=Fs*T. The signal must comes from sensor when this one is subjected to a zero input, and when there isn't temperature evolution (i.e. constant temperature or compensated temperature).

In this test the time history has a length of 4 hours with a sample frequency of 100 Hz.

The formula which gives the Allan variance is the following:

$$\sigma^2(\tau_{av}) = \frac{1}{2} E[(\overline{\Omega}_{k+1}(M) - \overline{\Omega}_k(M))^2]$$

(190)

with :

- $\overline{\Omega}_k$, the average of the data for the kth cluster. $\overline{\Omega}_k(M) = \frac{1}{M} \sum_{i=1}^{M} \omega_{(k-1)M+i}$

- M, the number of sampling in one cluster

- τ_{av} , the averaging time ($\tau_{av} = \frac{M}{Fs}$)

- Fs, the sampling frequency

- $E[]$, the ensemble average

Then it's possible to plot the Allan variance according to the various averaging time windows τ_{av}. Following the appearance of the plot, it will be possible to determinate the stochastic components included inside the *b₁(t)* bias. The following table shows the result of the Allan variance chart from several kinds of error mechanism signals:

Error Mechanism	Allan Variance Slope [70]
Quantization Noise	-1
Random Walk (or White Noise)	-1/2
Flicker Noise (or Random Bias)	0
Rate Random Walk	+1/2
Exponentially Correlated Noise (First Order Gauss-Markov Process)	+1/2
Linear Rate Ramp	+1
Sinusoidal	Sine curve

Table 13: Allan variance slope analysis

Thanks to this table, it will be possible to characterize the kind of stochastic error which is included inside the $b_1(t)$ bias.

In the next graphs, the term random walk refers to the Angle Random Walk model for gyroscopes and to the Velocity Random Walk for the accelerometers.
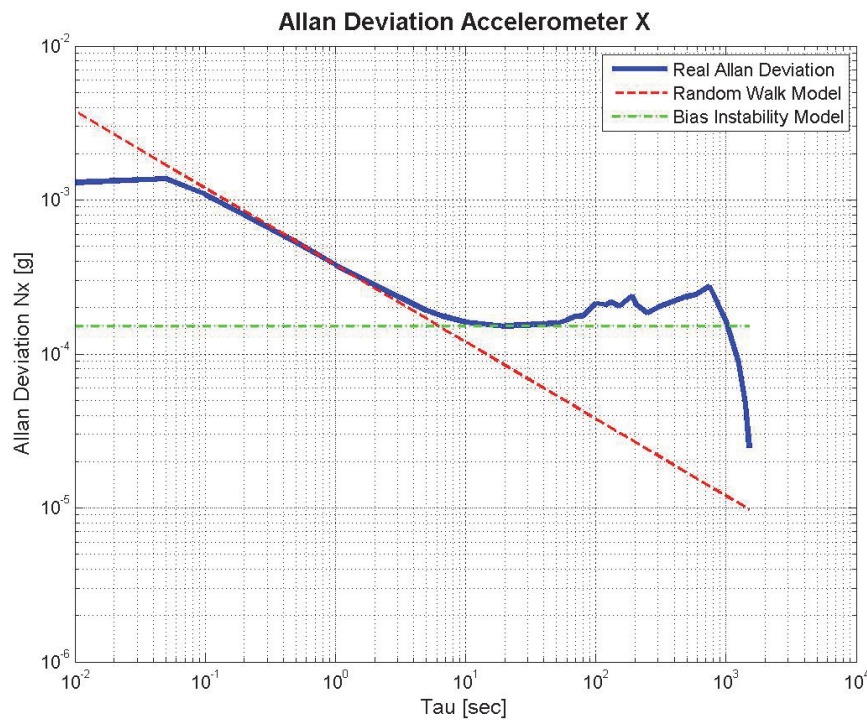
Figure XXXIII X-axis accelerometer Allan standard deviation
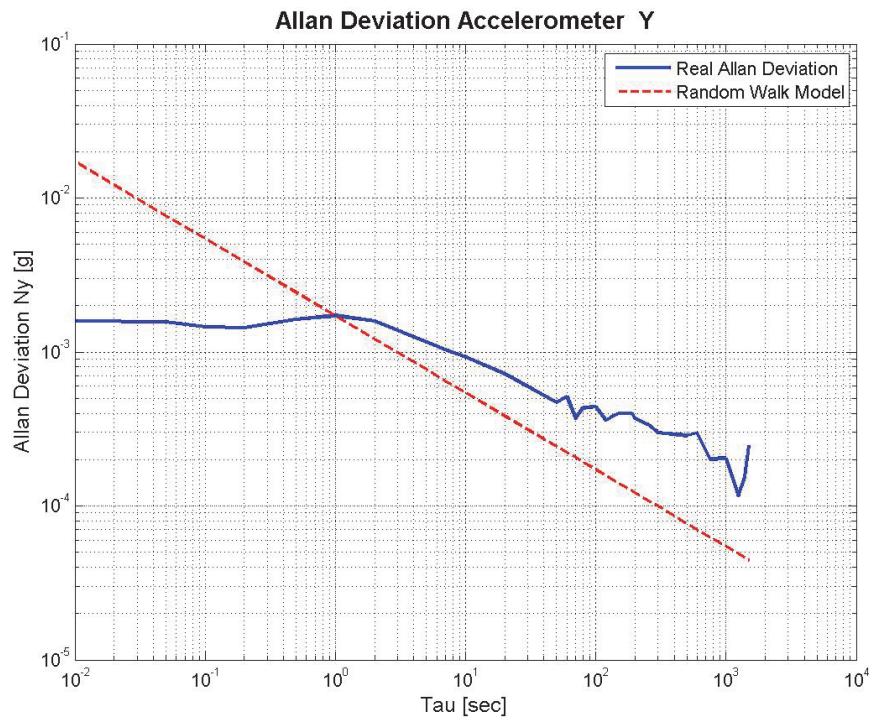
Figure XXXIV Y-axis accelerometer Allan standard deviation
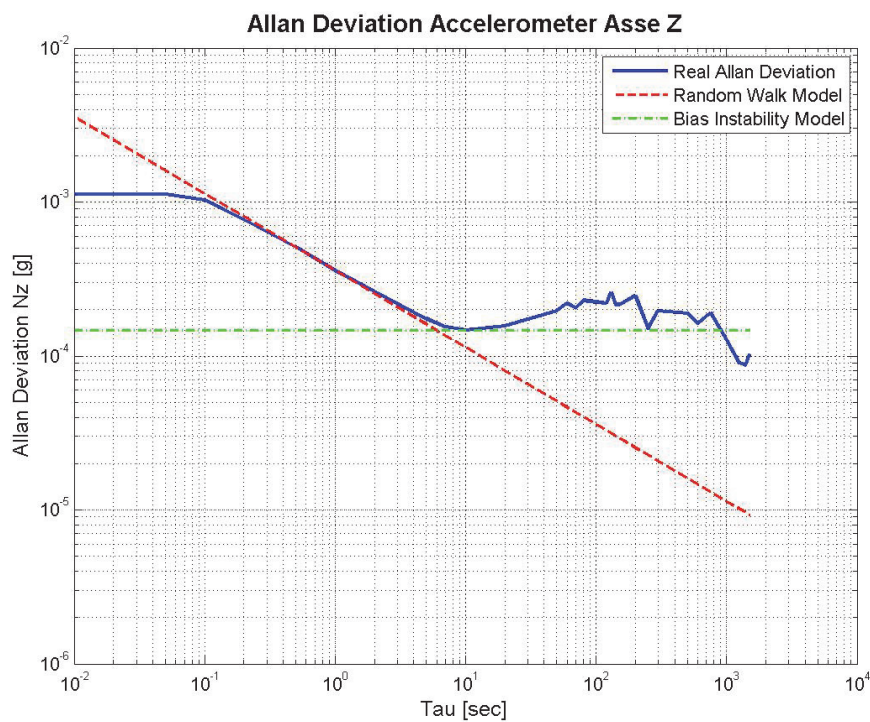
Figure XXXV Z-axis accelerometer Allan standard deviation

The analysis of accelerometers' plots shows two different contributions to Allan deviation: an angle random walk and a bias instability.
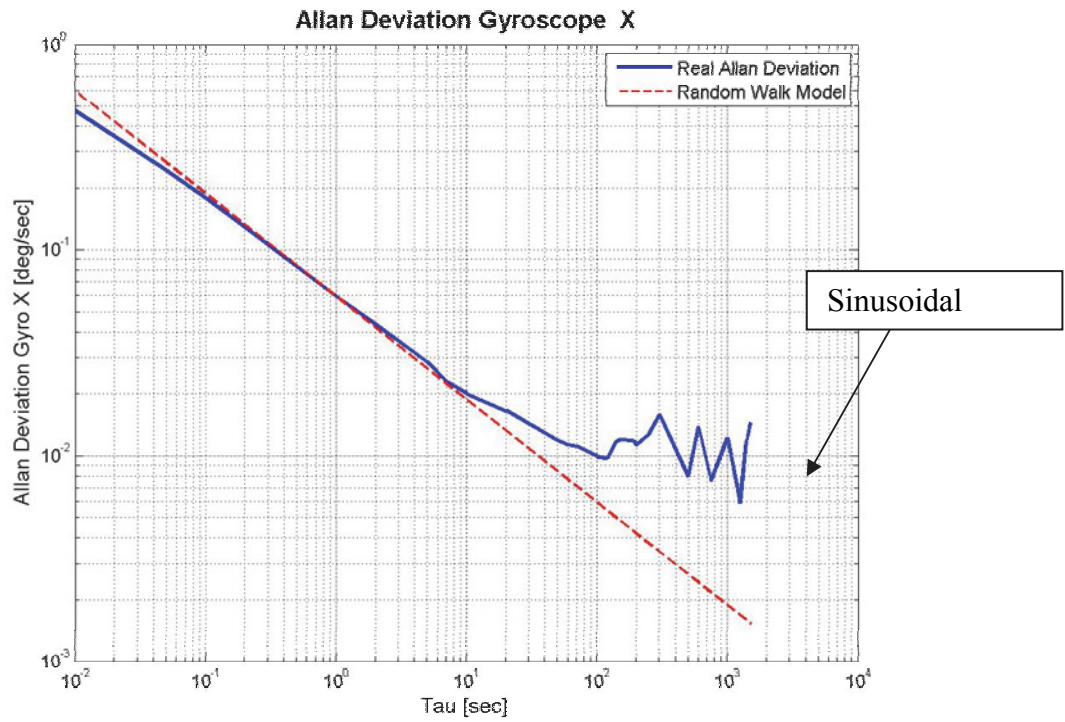
Figure XXXVI X-axis gyroscope Allan standard deviation
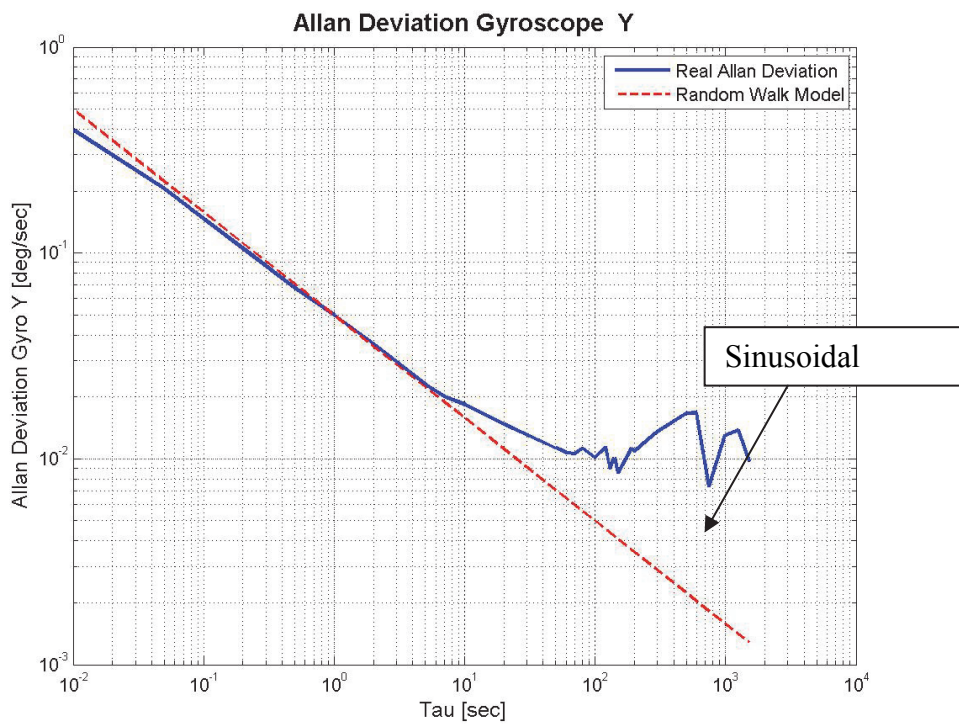
Figure XXXVII Y-axis gyroscope Allan standard deviation
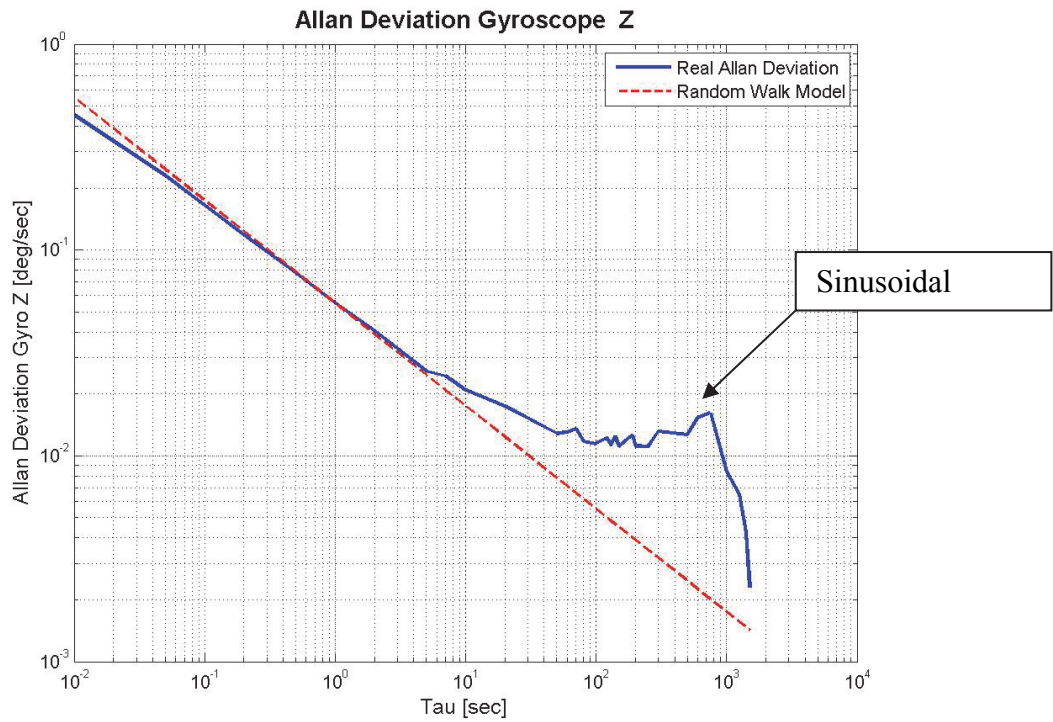
Figure XXXVIII Z-axis gyroscope Allan standard deviation

The analysis of plots for gyroscopes shows that at short averaging times. The Allan variance is dominated by noise. At higher averaging times, the sinusoidal noise appears.
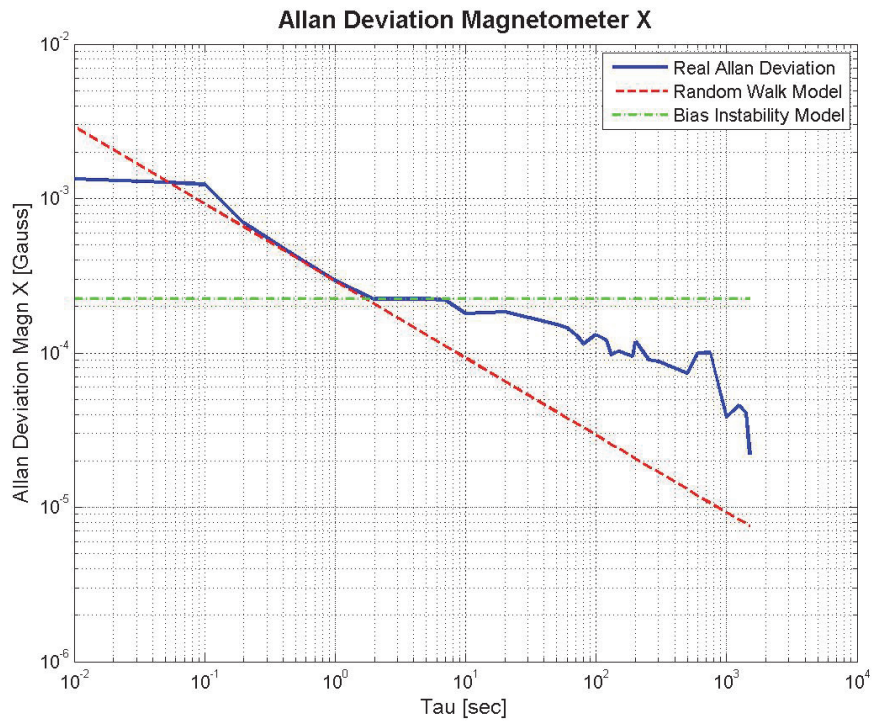
Figure XXXIX X-axis magnetometer Allan standard deviation
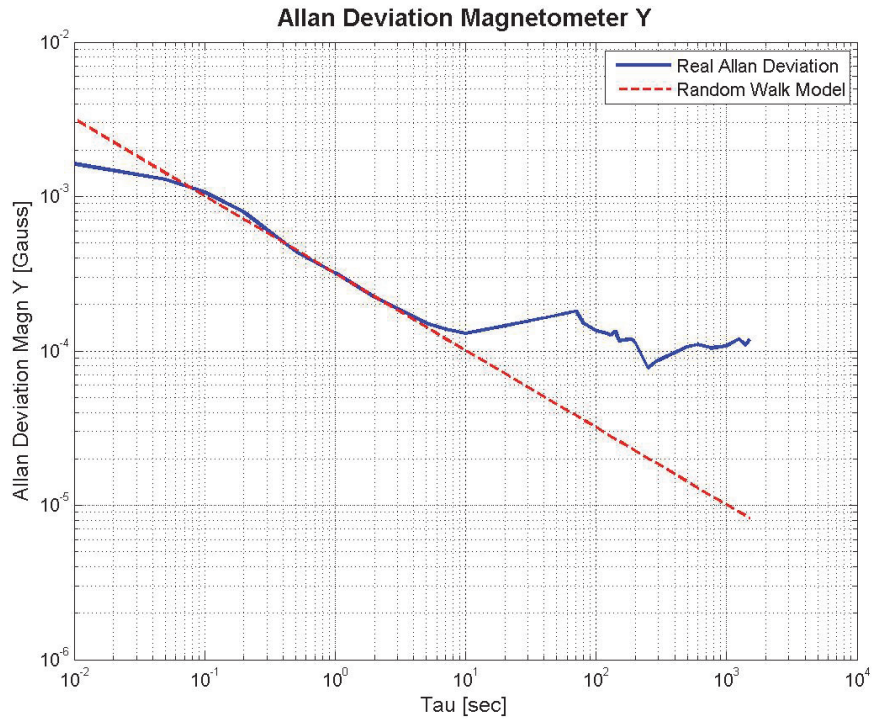
Figure XL Y-axis magnetometer Allan standard deviation
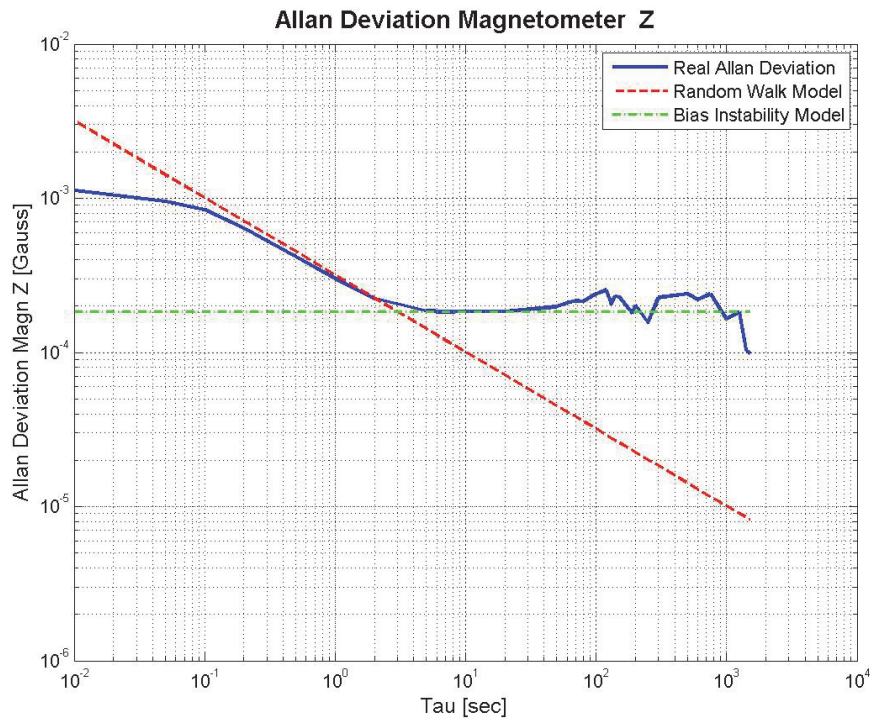
Figure XLI Z-axis magnetometer Allan standard deviation

The magnetometers also show two type of noise: angle random walk and bias instability. In the time span of our interest the main contribution to noise is represented by the white noise. In Table 14, for all the sensors we have summarized the Allan factors related to angle random walk and we have compared them with the datasheet value.

	ALLAN ANALISYS RESULTS				Datasheet Values [71]
	N (ARW) *[deg/ sqrt(sec)]*	*B* *[deg/sec]*	*Variance (deg/sec)^2*	*Bias Instability (deg/sec)*	*N (ARW)* *[deg/ sqrt(sec)]*
Gyro X	0.0594	N/A	0.2528	N/A	0.05
Gyro Y	0.0499	N/A	0.1773	N/A	0.05
Gyro Z	0.0553	N/A	0.227	N/A	0.05
	N(VRW) *[g/sqrt(Hz)]*	*B* *[g]*	*Variance [g^2]*	*Bias Instability (m/sec²)*	*N (VRW)* *[g/sqrt(Hz)]*
Acc X	0.0004	0.002	4.5e-6	1.5	0.0005
Acc Y	0.0017	N/A	1.3e-5	1.8	0.0005
Acc Z	0.0004	0.002	3.2e-6	1.1	0.0005
	N *[Gauss/sqr(Hz)]*	*B* *[Gauss]*	*Variance [Gauss^2]*	*Bias Instability (Gauss)*	*N* *[Gauss/sqrt(Hz)]*
Magn X	0.0003	0.0003	4e-6	2e-4	0.0005
Magn Y	0.0003	N/A	4.8e-6	1.5e-4	0.0005
Magn Z	0.0003	0.0003	2.8e-6	2e-4	0.0005

Table 14 Allan analysis final values

All the values obtained through the experimental tests confirm the datasheet information. Concerning Bias Instability the values obtained through Allan analysis are compatible with the class of sensors that we have analyzed.

These results, specifically the Angle Random Walk and the Velocity Random Walk factors, will be used to realize the error models for the inertial sensors and for the tuning of the Kalman filter.

4.3 Navigation

To prove the effectiveness of the navigation algorithm [Par 1.3], including its ability to estimate flexible motions, some simulations have been carried out in Matlab Simulink® environment using the aircraft simulation model presented in paragraph 4.1. Considering that flexible displacements, shown by the modeled aircraft, have a magnitude of few tens of centimeters, the accuracy of GPS receiver has been chosen equal to 1 cm, corresponding to a high accuracy GPS, operating in RTK differential mode. GPS measurements are updated with a frequency of 10 Hz, consequently the correction step of EKF works at the same frequency. The IMU sensors and four distributed accelerometers have been modeled with a typical MEMS sensors error model. Their data rate has been fixed to 100 Hz and consequently the prediction step of EKF works at this frequency.

The mode shapes matrices for a certain number of points, are provided by the FEM structural analysis. As stated in the previous paragraph the placement of distributed accelerometers is fundamental for an accurate estimation of the generalized coordinates, thus before performing any simulation, the selection of the best position for the four triaxial distributed accelerometers has been performed on the basis of the combination of the number and typology of estimable mode shapes. In Figure XLII is shown the condition number of matrix for different combination of number and typology of estimable mode shapes. The positions of triaxial distributed accelerometers are the same for all combinations. This condition number is a sort of measure of the accuracy that can be achieved in estimation of generalized coordinates. The best condition number (1.25) is obtained considering only the first two symmetric modes (the first generalized coordinates).

The observability of $\delta\eta$ state variable depends on the difference between mode shapes matrices relative to GPS antennas mounting points. To underline the importance of this consideration and to show how it heavily influences the quality of results, GPS antenna are positioned in points which can guarantee greater observability of the first generalized coordinate error term. In particular the matrix $\left(\Phi^{\#1} - \Phi^{\#2}\right)$ assumes the following value [Eq.**(191)**]:

$$\left(\Phi^{\#1} - \Phi^{\#2}\right) = \begin{bmatrix} 0.47 & 0.23 \\ -0.16 & 0.09 \\ -1.22 & 0.11 \end{bmatrix} \quad m$$

(191)

$$\Phi^{\#1} = \begin{bmatrix} 0.35 & 0.32 \\ -0.16 & 0.09 \\ -0.99 & 0.19 \end{bmatrix} \quad m$$

(192)

$$\Phi^{\#2} = \begin{bmatrix} -0.11 & 0.088 \\ 0 & 0 \\ 0.23 & 0.07 \end{bmatrix} \quad m$$

(193)

The terms in the first column of matrix in Eq.**(191)**, which is relative to the first generalized coordinate, have a greater magnitude respect to terms of the second one, which is relative to the second generalized coordinate (in the third row, which represents the influence of vertical relative displacement error term $\delta\Delta r^e_{ant} \_ z$ on the generalized coordinates error term, the two terms have values which differ for an order of magnitude). After the choice of sensors locations, the maneuver to be simulated had to be decided. To excite structural elastic motions, two abrupt elevators deflections have been simulated: in particular a first pulse (with a positive one degree magnitude and a 6 sec width) starting at time instant 2 sec and a second one pulse (with a minus one degree magnitude and a 10 sec width) starting at time instant 50 sec. In Figure XLIII and Figure XLIV the generalized coordinates, estimated with the proposed Kalman Filter (blue lines), are presented together with the true values and with values obtained with a simple double integration of Eq.**(44)**. As expected the first generalized coordinate is estimated with a greater accuracy than the second one. In Figure XLV and Figure XLVI estimations of wing tip displacements are also reported. Estimated values of displacements along X direction in the Body reference frame have a lower accuracy than the Z direction, because of the greater influence of the second generalized coordinate on the elastic motions along this direction (this dependence can be easily verified comparing value of $\Phi^{\#1}$ mode shape matrix [Eq. **(192)**]. Considering the results obtained along the Z-direction as representative of the proposed algorithm potentialities, the accuracy in the elastic motion estimate, using a couple of GPS antennas with differential RTK, is less than 1 cm. In general the accuracy of the proposed algorithm will be dependent only by the level of accuracy that the chosen GPS system can provide.
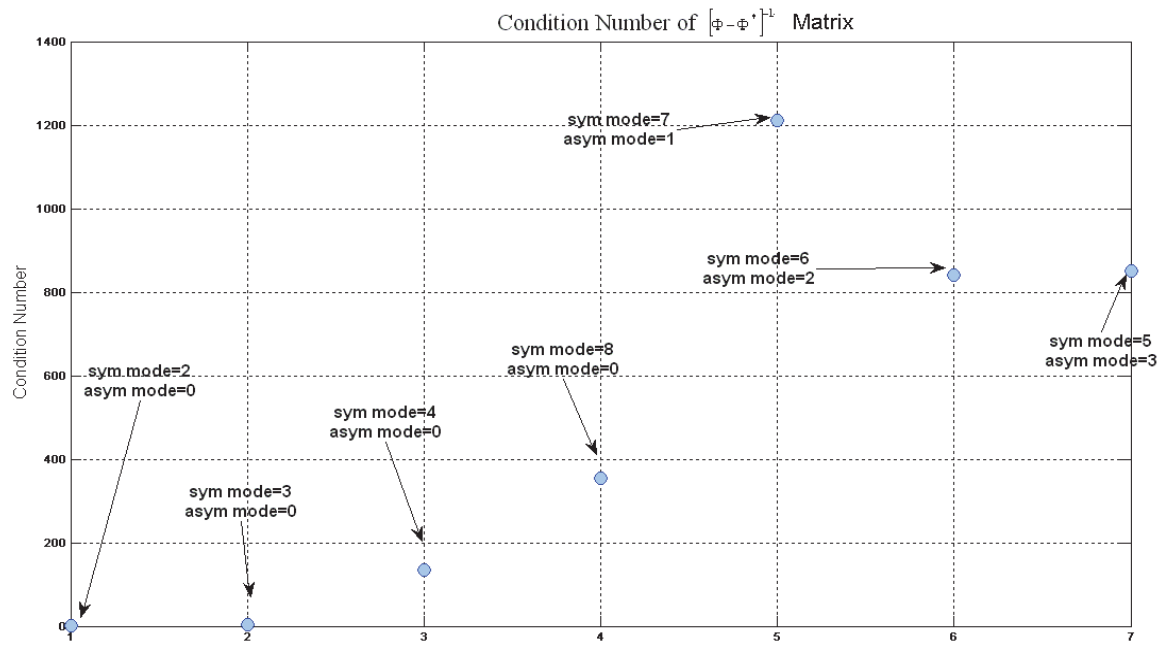
Figure XLII Condition Number for different choices of mode shapes.
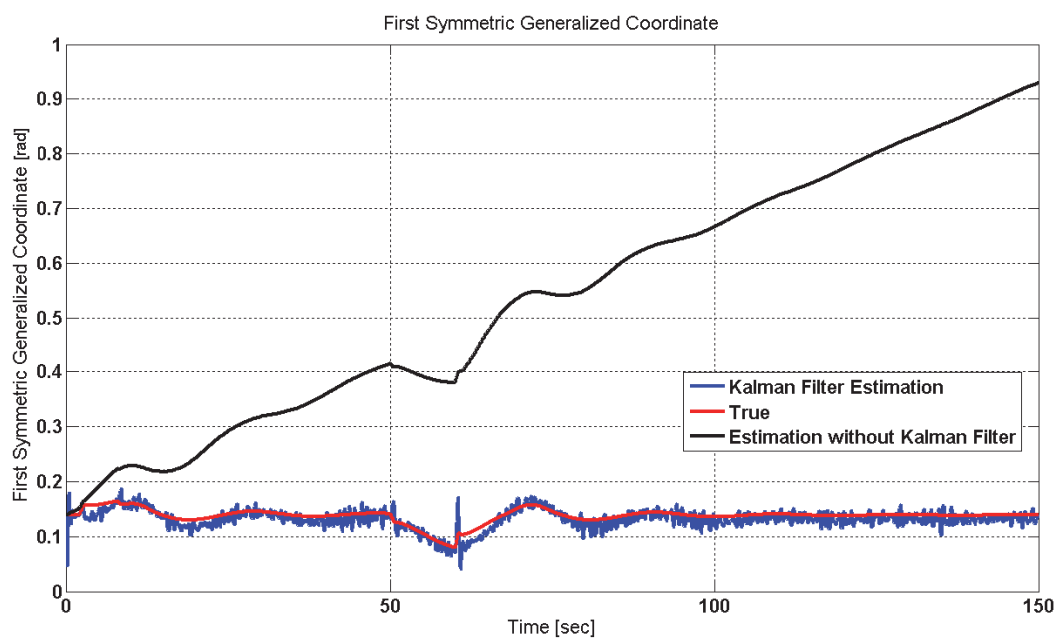
Figure XLIII Estimation of first generalized coordinate
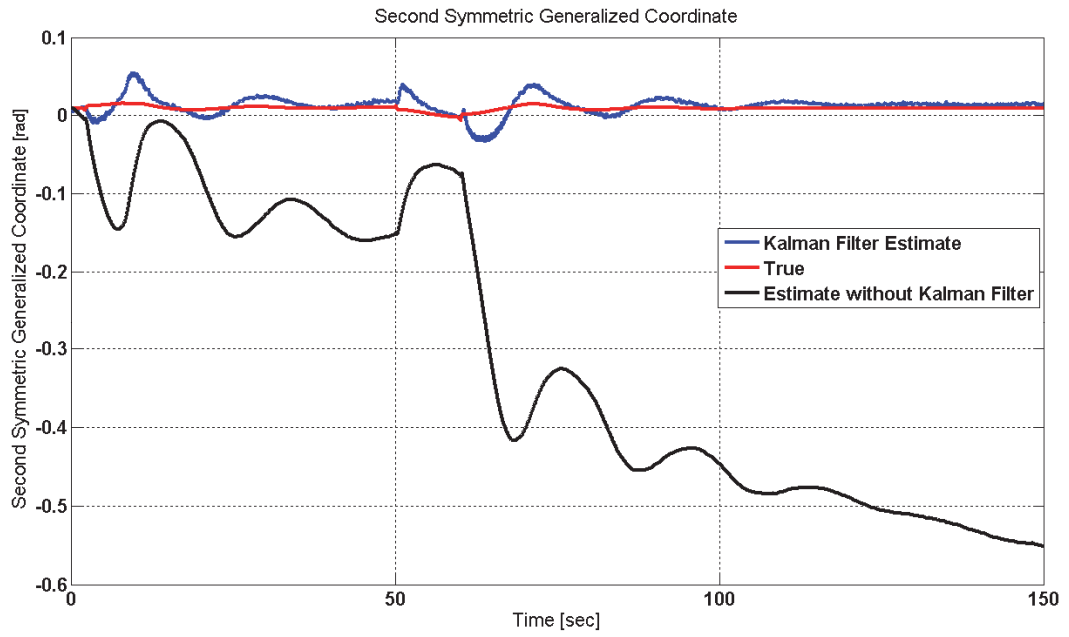
Figure XLIV Estimation of second generalized coordinate
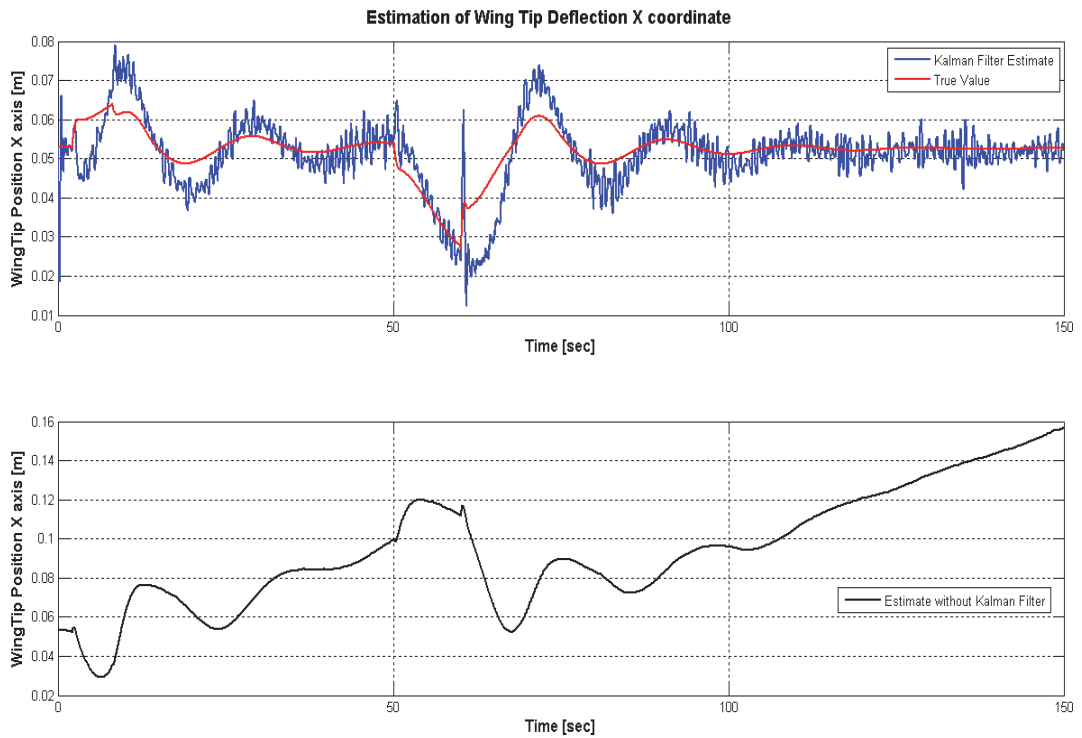
Figure XLV Estimation of Wing Tip deflection X coordinate
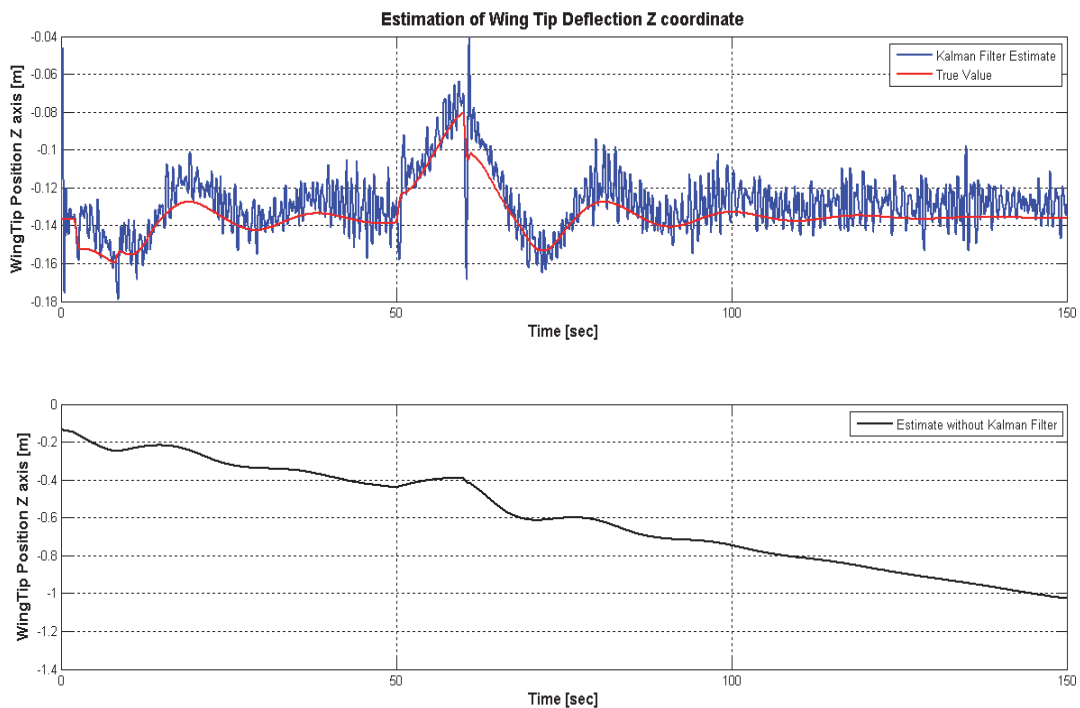
Figure XLVI Estimation of Wing Tip deflection Z coordinate

In these last figures a comparison between aircraft center of gravity position estimated using the proposed navigation algorithm and a standard EKF based on rigid body modeling has been reported.

For the modeled aircraft, flexible motions have very low magnitude, thus there is not an extremely evident improvement in results.

The improvement has a magnitude of few centimeters. This result is coherent with the magnitude of flexible motions showed in previous figures.
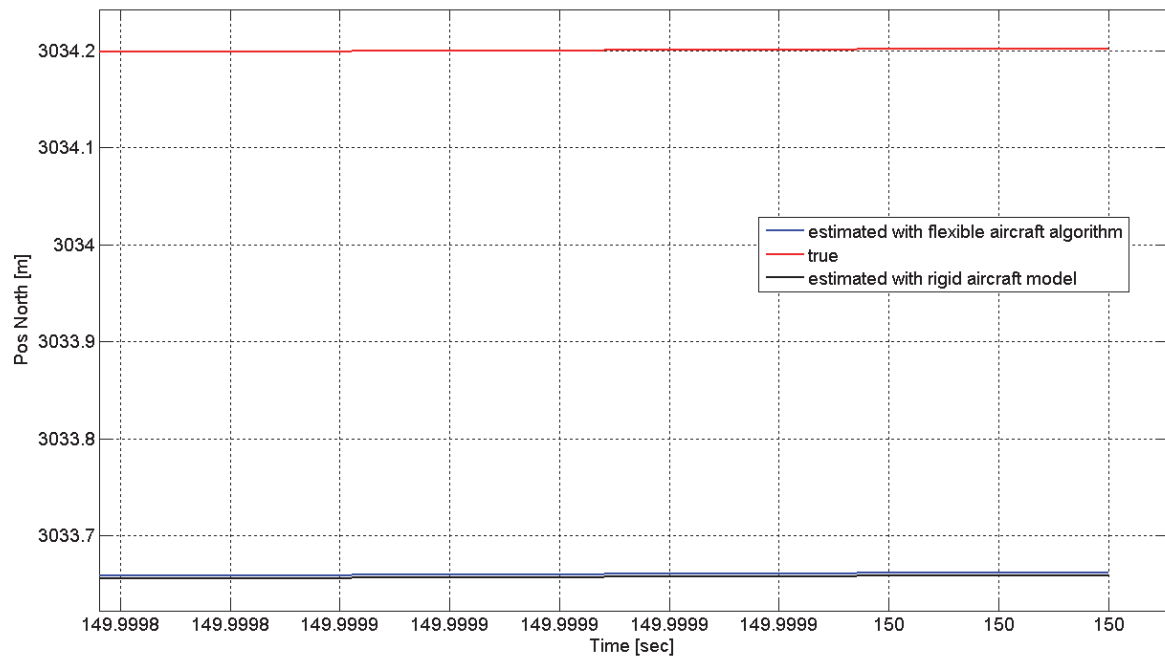
Figure XLVII Comparison between Position estimation with and without flexible aircraft model.
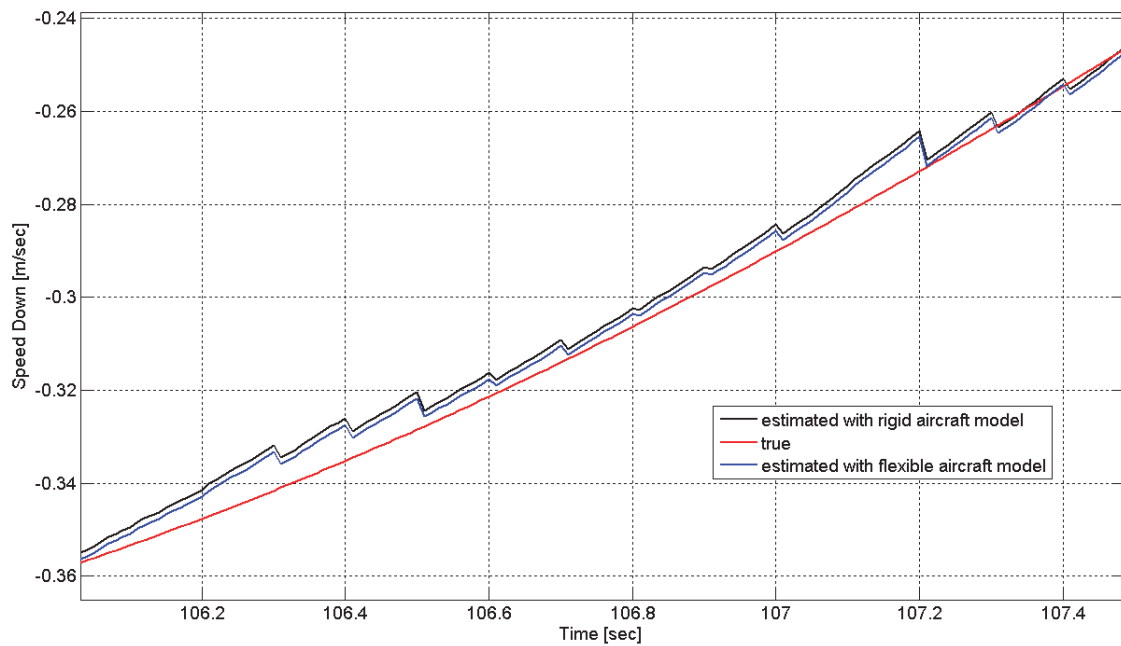
Figure XLVIII Comparison between Speed estimation with and without flexible aircraft model.

4.4 Flexible Displacements Estimation

As stated in paragraphs 2.1 and 2.3, the simulated sensor setup includes a camera with the related LED, four triaxial accelerometers and an IMU. It is useful to remark that the optimal arrangement depends on the model order which you have to estimate; consequently before executing any simulation, the selection of the best arrangement for the four triaxial distributed accelerometers and for the video-based system has been performed. Concerning accelerometers, the same positions indicated in the previous chapter have been chosen.

The LED is placed on the wing tip, while the Camera is placed on the tail empennage to centre the LED in the undeformed condition.

In Figure XLIX a schematic view of the sensors arrangement on the modeled aircraft has been reported.
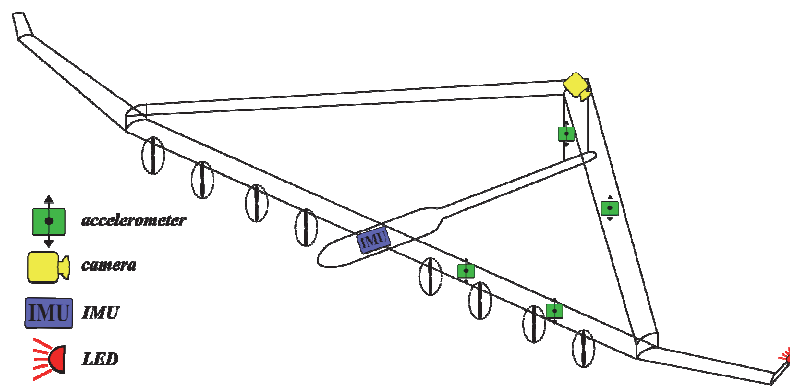
Figure XLIX Schematic view of the Sensor Setup.

In Table 15, the principal parameters describing the features and the error of the simulated sensors have been reported. The error model of inertial sensors, used in simulations, is typical of Micro Electro-Mechanical Systems (MEMS) sensors.

Sensors Parameters	
Camera Field of View	5°
Camera Resolution	1024 x 768 pixel
LED Radius	0.01 m
Focal Length/ photosensitive element dimension Ratio	11727
Frame Rate	10 Hz
Accelerometers Bias	2 mg
Accelerometers Noise @ 30 Hz (Standard Deviation)	0.0012 g
Gyroscopes Bias	0.5 deg/sec
Gyroscopes Noise @ 40 Hz (Standard Deviation)	0.32 deg/sec

Table 15 Sensors Parameters

Also in these simulations the elastic dynamic of the aircraft has been represented with the first two symmetric generalized coordinates $[\eta_1, \eta_2]$ and an elevator deflection is imposed in order to excite structural motions (Figure L).
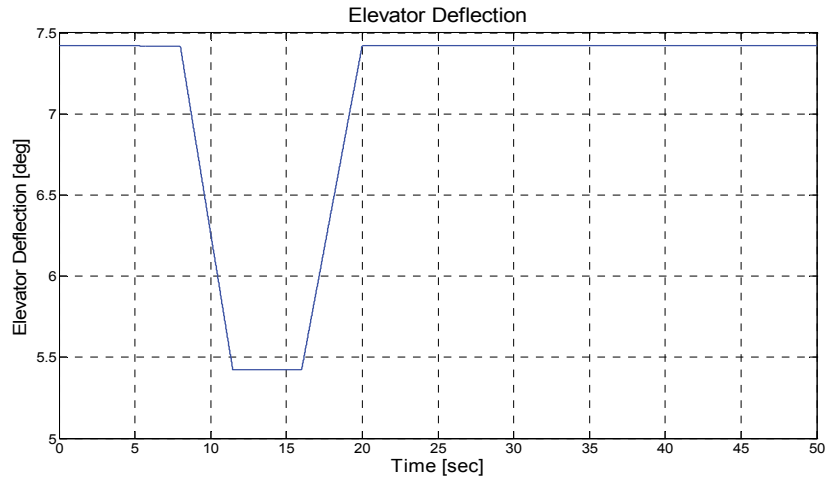
Figure L Elevator Deflection

In Figure LI and Figure LII it is reported the result of the generalized coordinates estimation.
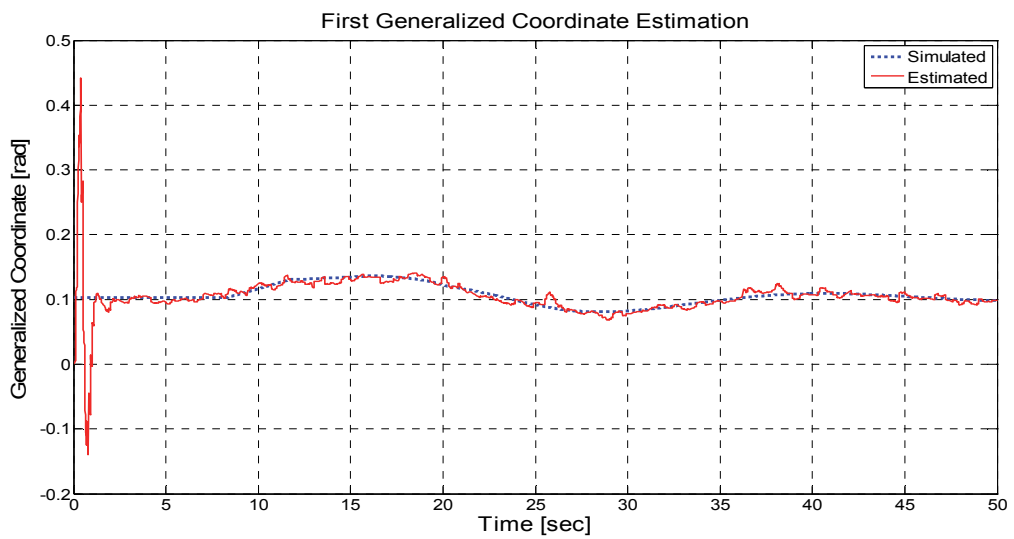
Figure LI First Generalized Coordinate Estimation
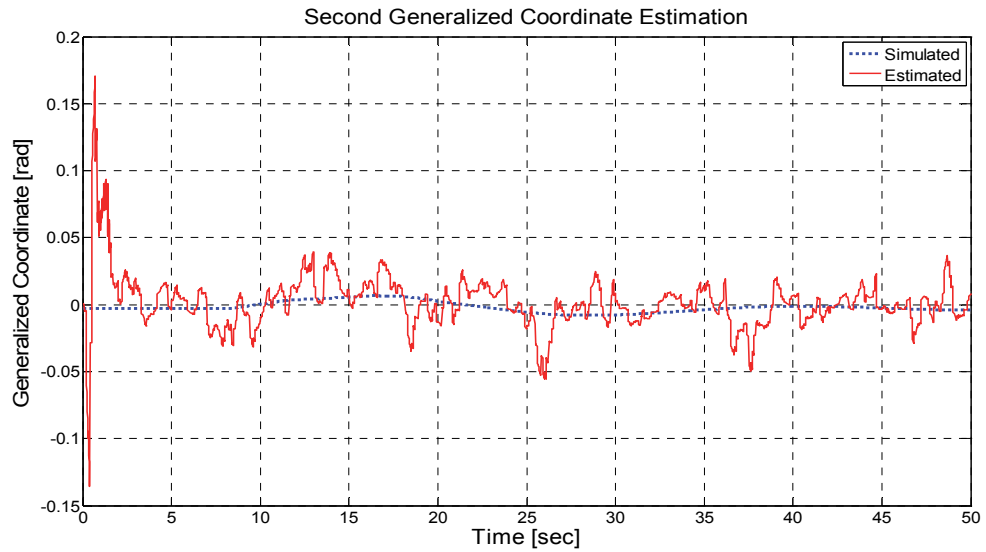
Figure LII Second Generalized Coordinate Estimation

In Figure LIII it is reported the variance (the diagonal elements of the variance matrix estimated by the Kalman Filter) for both the estimated generalized coordinates and their first derivatives. The variance is a means to assess the accuracy of estimation performed by the filter. A regime the variance for the first and the second generalized coordinate is respectively equal to 0.00042 rad^2 and 0.0023 rad^2; while for the relative derivatives is equal to 0.0012 $(rad/sec)^2$ and 0.0078 $(rad/sec)^2$. The first generalized coordinate is estimated with greater accuracy, this is due essentially to its greater observability.
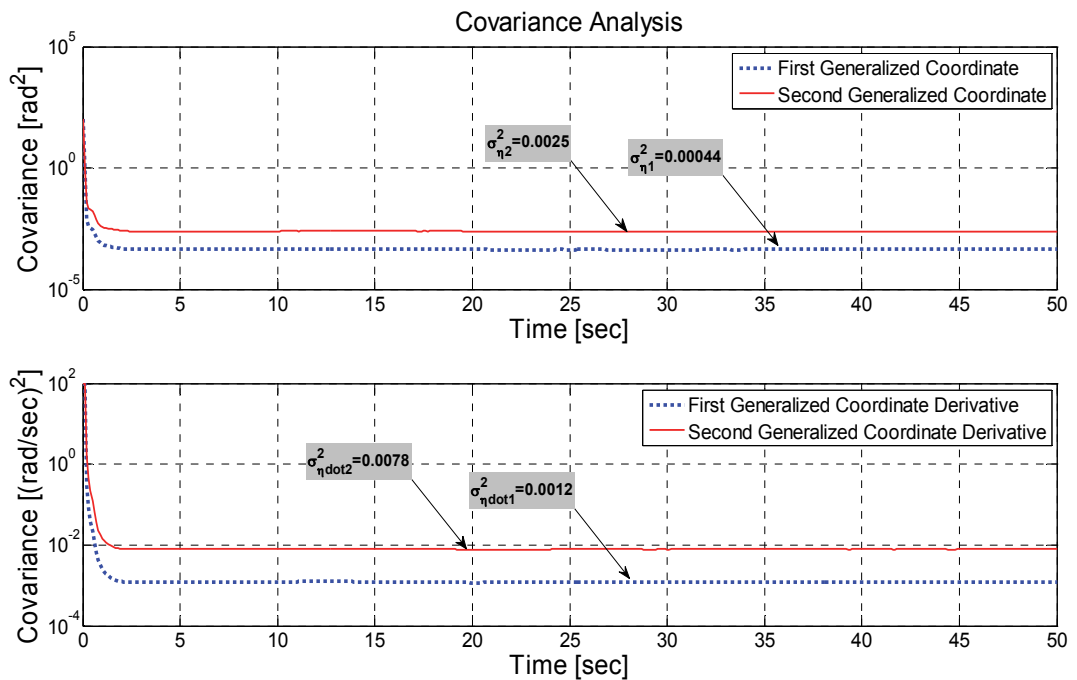
Figure LIII Covariance Analysis

Some simulations, in conditions of failure of the video-based system, have been also carried out. Specifically, Figure LIV and Figure LV illustrate the results of numerical tests in which a

failure of the video system has been simulated (starting from time instant 20 sec up to time instant 30 sec). In absence of observations, the estimation of generalized coordinates is performed using only the prediction step of the EKF. As it is clearly shown in Figure LIV and Figure LV, the estimation diverges because of inaccuracies (noise and bias) of the inertial measurements. After the disappearance of the system failure (at time instant 30 sec) the estimation rapidly converges again towards the true value.
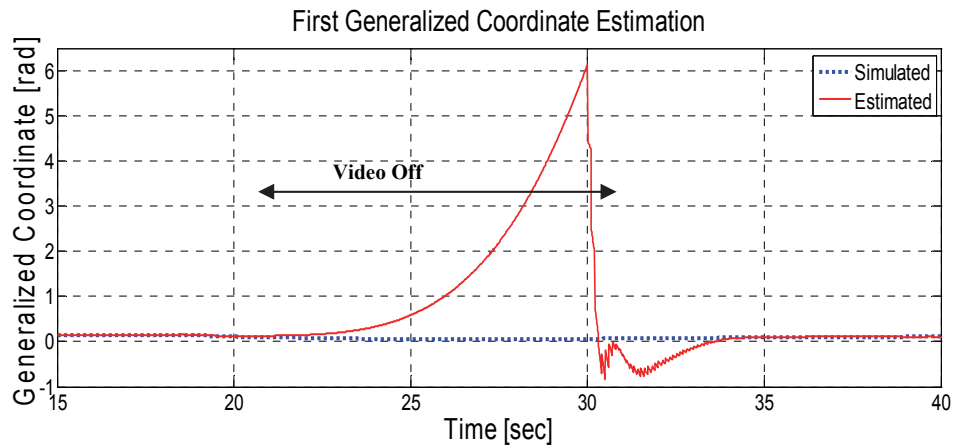
Figure LIV First Generalized Coordinate Estimation with a limited duration failure in the video system
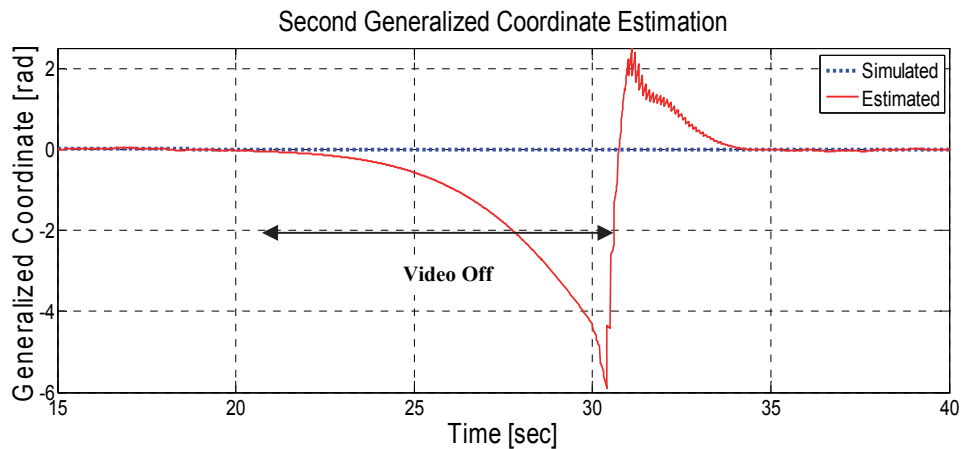
Figure LV Second Generalized Coordinate Estimation with a limited duration failure in the video system

In Figure LVI, Figure LVII and Figure LVIII we have reported the results of LED displacements estimation. This estimation has been performed applying Eq. **(27)** and substituting the generalized coordinates with their estimation. A video-based system composed by one camera, used standalone, cannot provide any information about three dimensional displacements of a generic point, because the number of equations (bidimensional displacements in the image plane) is less than the problem unknowns.

Using only a video-based system, in order to estimate three dimensional displacements, at least two cameras (stereo-vision) have to be included in the setup, with an increase in costs and weights.
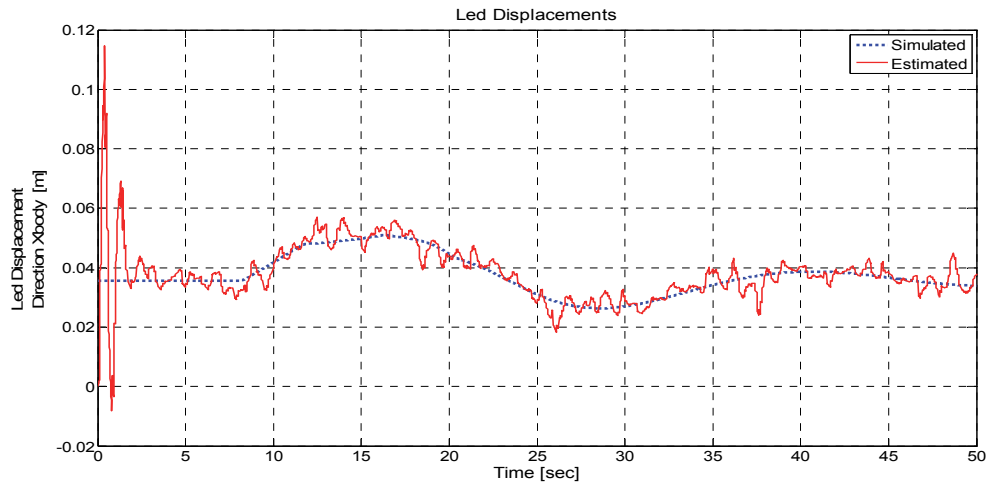
Figure LVI Led Motion Xbody direction
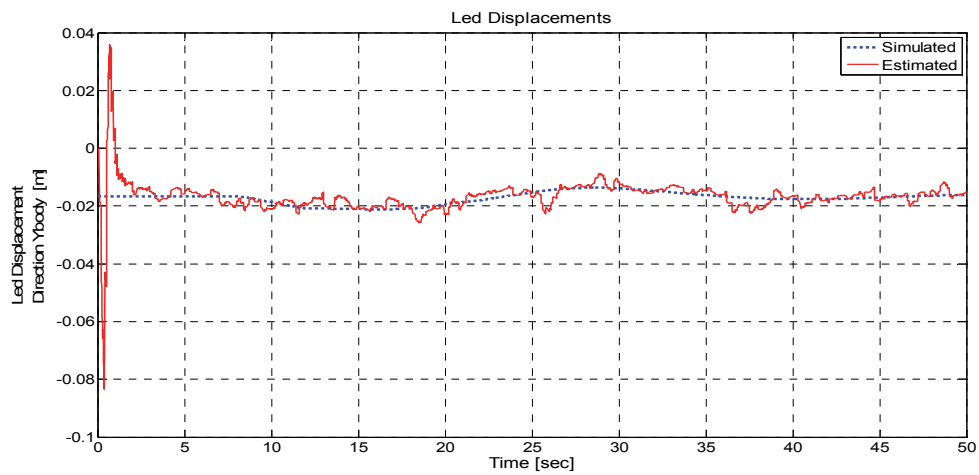
Figure LVII Led Motion Ybody direction
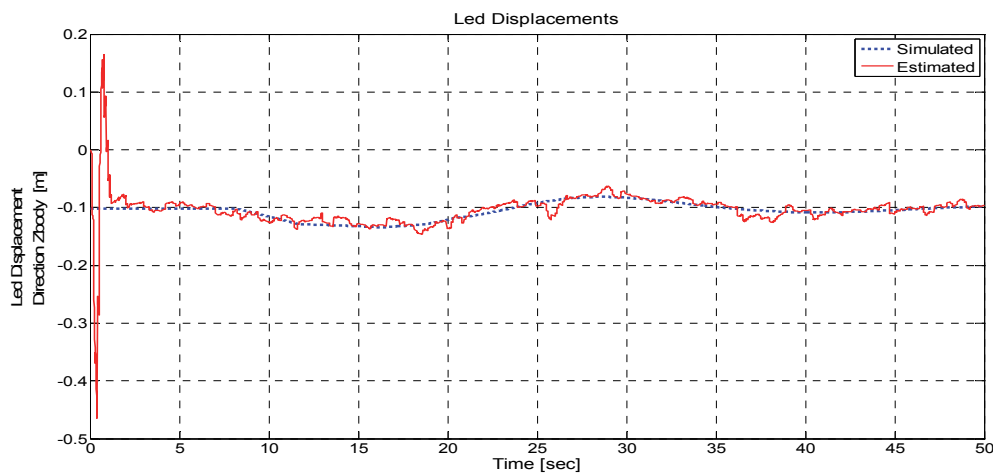
Figure LVIII Led Motion Zbody direction

Applying the technique proposed in [72], we have evaluated the degree of observability of the proposed state variables. Considering that the number of state variables is equal to four, eigenvalues are comprised in the range $[0 \div 4]$.

The smaller eigenvalues is equal to 0.0154, the corresponding eigenvector represents the direction of higher observability, its components are [-0.9207; -0.3523; 0.1610; 0.048]. This eigenvector is direct predominantly along the first state variable, consequently the first generalized coordinate has the greatest observability. This result was expected because of the particular choice of the camera and led installation points, in fact motions of these points are predominantly influenced by the first mode shape. In Figure LIX the eigenvalues of the normalized covariance matrix have been reported, in order to show their rapid convergence.
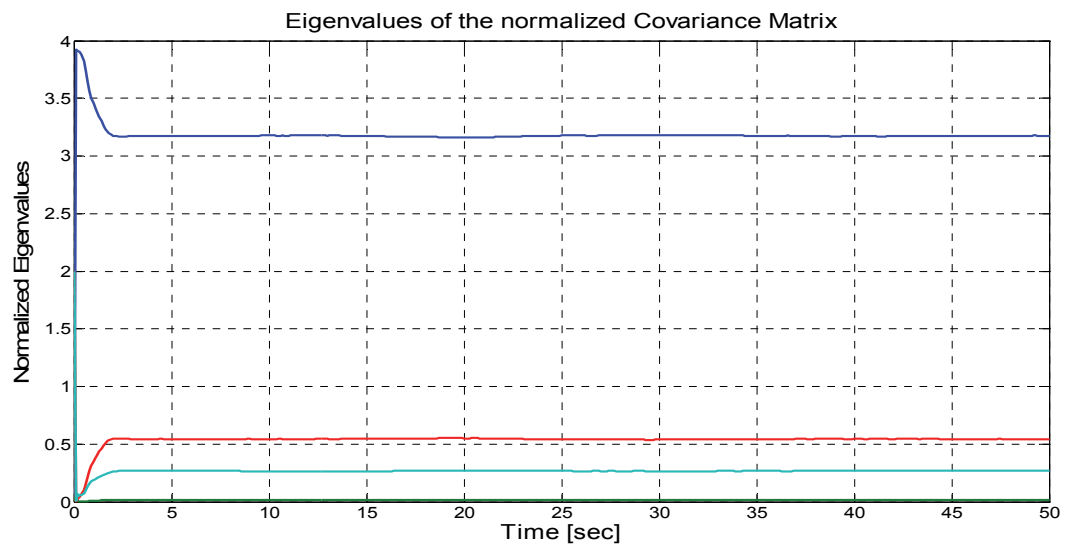
Figure LIX Eigenvalues of the Norm. Covariance Matrix

4.5 Load Alleviation

In this section the numerical validation of the load alleviation system is reported.

To validate the effectiveness of the load alleviation system, it has been simulated the scaled High Altitude Long Endurance UAV in a specific leveled-wing flight condition (true airspeed of 25 m/s and an altitude of 500 m) and affected, after 5 seconds of undisturbed flight, by a wind shear, whose formula and parameters are reported in Eq.(194) and **Table 16**.

$$w_{wind} = A(1 - \cos(\omega t - \omega t_0))$$

(194)

WIND SHEAR PARAMETERS

Parameter	Description	Value
A	Semi-amplitude of wind disturbance	2.5 (m/s)
ω	Angular frequency of disturbance	π (rad/s)
t_0	Time duration of disturbance	5 (s)

Table 16 Wind Shear Parameters
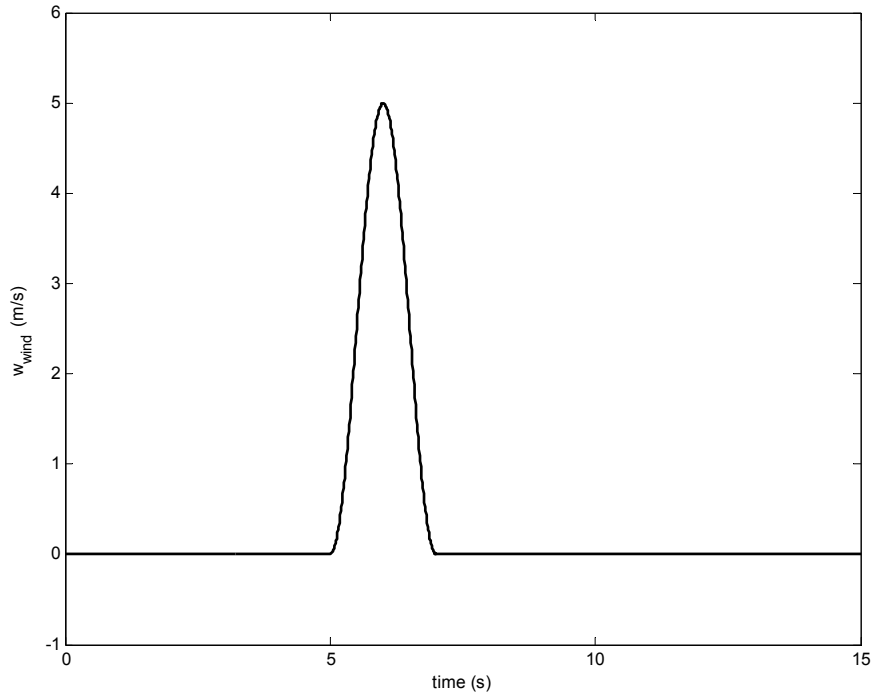
Figure LX The considered wind gust

The LQ regulator has been applied by considering only the first bending mode of the elastic structure, thus considering a simple linearized model of the system as reported in Eq.**(195)**.

$$\begin{bmatrix} \dot{\eta}_1 \\ \ddot{\eta}_1 \end{bmatrix} = \begin{bmatrix} 0 & 1 \\ -67 & -5 \end{bmatrix} \cdot \begin{bmatrix} \eta_1 \\ \dot{\eta}_1 \end{bmatrix} + \begin{bmatrix} 0 & 0 & 0 & 0 & 0 & 0 & 0 & 0 & 0 & 0 \\ -3 & -3 & -2 & -2 & 0.1 & 0.1 & 15 & 15 & 18 & 18 \end{bmatrix} \cdot u_{la}$$

(195)

By choosing the state weighting and control weighting matrices, of the cost function in **(173)**, as two diagonal matrices, whose diagonal values are reported in Eq.**(196)**. The first element of diag_Q is relative to η_1, while the second is referred to its derivative. With reference to diag_R, the early six elements are the weights of the six elevators and the remaining four elements are used to weight the ailerons.

$$diag\_Q = \begin{bmatrix} 0.2 & 0.001 \end{bmatrix};$$

$$diag\_R = \frac{1}{30} \cdot \begin{bmatrix} 1 & 1 & 1 & 1 & 1 & 1 & 2 & 2 & 2 & 2 \end{bmatrix};$$

(196)

it has been obtained a control gain matrix as in Eq. **(196)**.

$$K = 0.1 \cdot \begin{bmatrix} -1.2 & -1.2 & -0.7 & -0.7 & 0.03 & 0.03 & 2.8 & 2.8 & 3.5 & 3.5 \\ -0.2 & -0.2 & -0.1 & -0.1 & 0.006 & 0.006 & 0.57 & 0.57 & 0.7 & 0.7 \end{bmatrix}^T$$

(197)

The control system obtained has been tested in the aforementioned flight condition and three configurations have been compared. The first configuration is the open loop system, that is to say the vehicle flying without a load alleviation system. The second configuration is the vehicle provided with the load alleviation control based on the LQ technique but exploiting an ideal feedback signal set, that is to say the "simulated" generalized coordinate, η_1, and its derivative, $d\eta_1/dt$, of the first bending mode. The third configuration considers the full load alleviation system with the LQ-based control and using the "estimated" data by means of the elastic motion estimator.

In Figure LXI the time histories of the first bending mode are reported. They have been simulated by means of the three configurations above described. It is evident the significant reduction of the peaks of the oscillation, obtained by adopting the load alleviation system. It is, anyway, present a certain oscillation with quite low amplitude while adopting the load alleviation system, this can be referred to the interactions between the control system and the non-linearities of the actuators, but particularly to the equivalent delay represented by the proper dynamics of the Kalman filter, present in the estimator. The last remark is proven by comparing the results of the control with ideal feedback and those of the control with estimated data.
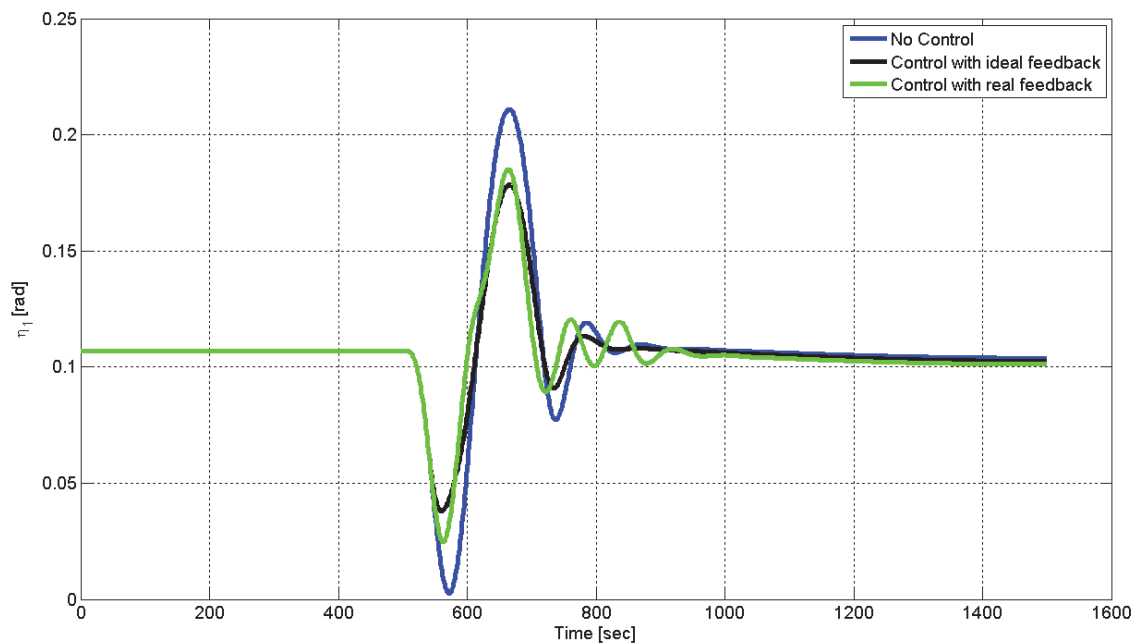
Figure LXI Time history of first bending mode. Comparison between the open loop system, the closed loop with ideal feedback signals and the load alleviation system described in the paper.

For the sake of completeness in Figure LXII are shown the time histories of two surface deflections, where it is evident the effect of the death-zone of the actuators.

The performances of the overall system may be improved by using sensors with better properties in terms of both: accuracy and data rate. Furthermore, a deeper analysis of sensors placement may also lead to an improvement of performances, while estimating the generalized coordinates. This aspect is particularly critic for both the LED and the distributed accelerometers.

To prove the assertion about the sensor properties, it is enough to change the only camera frame rate parameter adjusting it up to 50 Hz instead of 25 Hz.
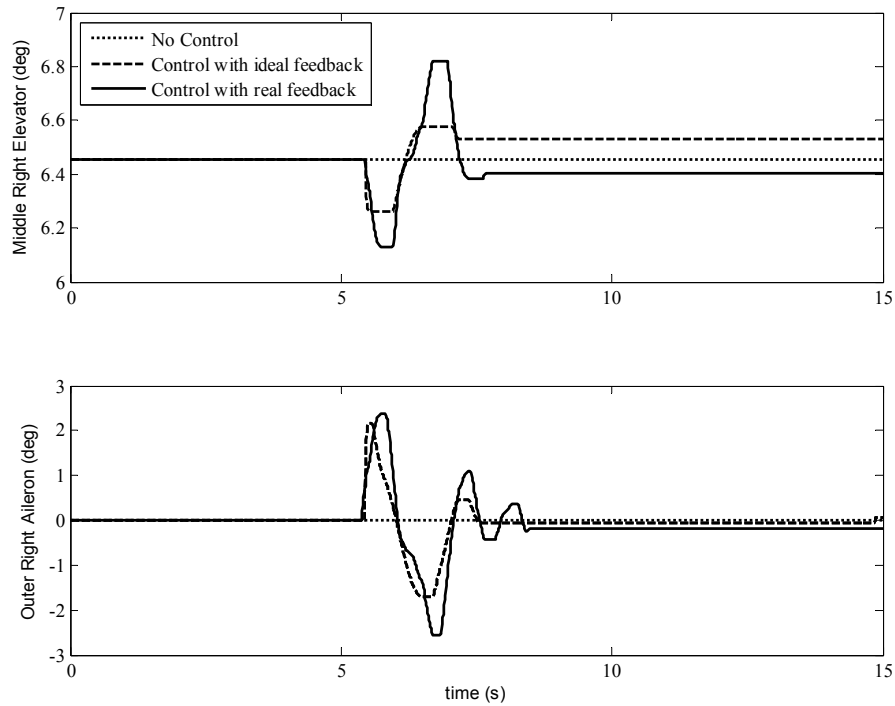
Figure LXII Deflections of the middle right elevator (up) and the outer right aileron (down). Comparison between the open loop system (dotted line), the closed loop with ideal feedback signals (dashed line) and the load alleviation system described in the paper (solid line).

In Figure LXIII comparison is made between the results provided by the overall system considering two different frame rates: 25 Hz and 50 Hz. The slight improvement is due to the reduction of the delay, while estimating the generalized coordinates. Trivially, a reduced delay corresponds to better performances in damping the oscillations of the structure.
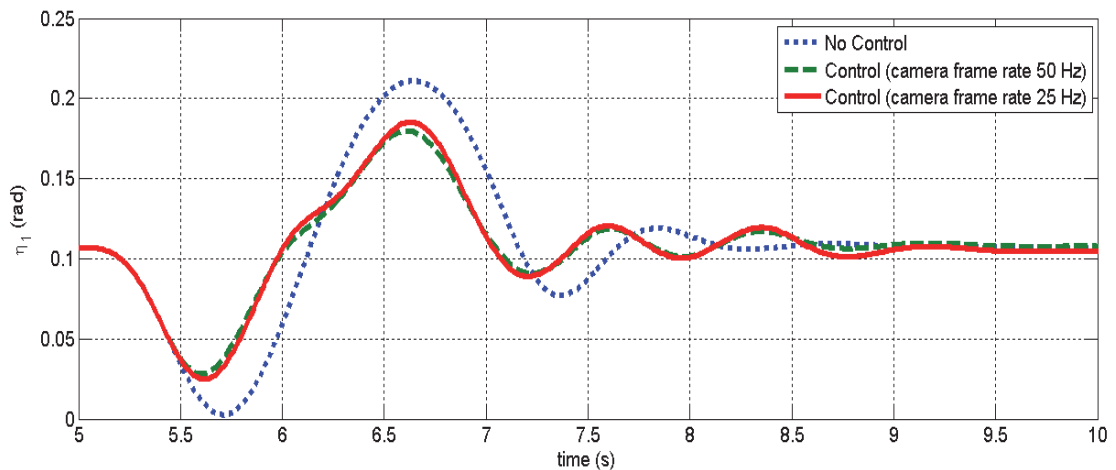
Figure LXIII Time history of first bending mode. Comparison between the open loop system, the closed loop system with a camera frame rate of 25 Hz and the closed loop system with a camera frame rate of 50 Hz.

In the light of the previous consideration, it is possible to design again the control system, to exploit the better estimation. The parameters adopted in the cost function to design the new

control system are reported in Eq. **(198)** and the corresponding results, in terms of control matrix values are shown Eq. **(199)**.

$$diag\_Q = \begin{bmatrix} 0.25 & 10^{-6} \end{bmatrix};$$

$$diag\_R = \frac{1}{30} \cdot \begin{bmatrix} 1 & 1 & 1 & 1 & 1 & 1 & 1.5 & 1.5 & 1.5 & 1.5 \end{bmatrix};$$

(198)

$$K_{new} = 0.1 \cdot \begin{bmatrix} -1.4 & -1.4 & -0.8 & -0.8 & 0.04 & 0.04 & 4.4 & 4.4 & 5.4 & 5.4 \\ -0.2 & -0.2 & -0.1 & -0.1 & 0.005 & 0.005 & 0.62 & 0.62 & 0.7 & 0.7 \end{bmatrix}^T$$

(199)

In Figure LXIV, the variation of the first bending mode obtained using the new control system is reported and compared with previous result. As expected, a better damping of oscillations is obtained, both when the gust is acting and when it is no longer present.
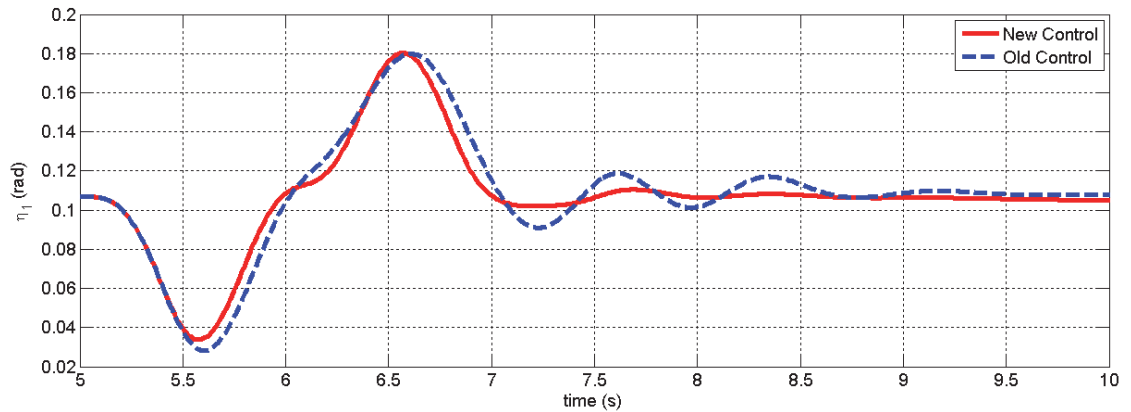
Figure LXIV Comparison between the old control system and the new control system.

5 Conclusions and Future Works

The main results of the research activities conducted during PhD studies, have been summarized in this work.

These activities have concerned the analysis of the influence of flexibility in GN&C area of interest.

Motivation for this work has been principally provided by the PRO.RA program HAPD realized by CIRA with the aim to realize a demonstrator of an HALE aircraft.

Structural flexibility has a great impact on aircrafts having high aspect ratio wings and/or a slender fuselage, such for example HALE aircrafts. Structural deflections are also present on launchers, missiles and other large space structures.

Modern design philosophies are leading towards lighter and lighter structures to the detriment of structural stiffness, consequently also commercial aircrafts suffer of problems related to flexibility.

A fundamental aspect to take into account analyzing structural flexibility is that deflections have a frequencial content in the same band of rigid motions and obviously in the band of sensors used for GN&C purposes.

These "spurious" measurements could lead to instability of the control loop.

In the field of GN&C sensors, a correct modeling of structural displacement is required for navigation systems presenting lever arms between the different components, such as ADGPS, Gyro free INS or Multiple INS.

The navigation system more influenced by this phenomenon is, beyond doubt, the ADGPS based on carrier-phase measurements, which requires a precise knowledge of baselines length.

Moreover, modern aircrafts used as ISR flying platforms, in particular configurations, have sensors completely integrated in their structure. For these applications, the position and/or the exact shape of the sensor (as for example a radar antenna) shall be known with great accuracy because they influence the performances of the sensor.

In the light of the previous considerations, estimation of the aircraft actual shape assumes great importance.

In this thesis, estimation of the aircraft actual shape is based on modal decomposition and on the application of different sets of sensors, whose measurements are combined in an Extended Kalman Filter.

Modal decomposition technique is based on the principle of linear superimposition and consequently its validity is limited to a "little" ratio between structural displacements and a

representative length. The semi wingspan or fuselage length can be considered as representative length, a practical threshold for the proposed ratio is 0.15. A literature review have confirmed that for the most part of actual aircrafts, the ratio between structural deflections and a representative length have a magnitude similar to the proposed threshold, thus modal decomposition can be applied.

Moreover the application of an EKF is based on the application of a linearized system, thus there in not any direct advantage in using a non-linear modeling of flexible phenomena.

The proposed sensor set includes an IMU and several accelerometers positioned along the aircraft (depending on the number and type of generalized coordinates we have to estimate) and, this is an innovative aspect, GPS antennas or a video system composed by a camera and a LED.

The GPS, in standalone operative mode, has a very low accuracy which limits its applicability only to very large motions. GPS can be used for determination of the actual aircraft shape only if used with differential corrections or using carrier phase measurements (this last possibility will be described with greater details later).

The video-system offers greater accuracy which allows estimation of typical structural deflections.

Estimation of aircraft actual shape has been associated with estimation of parameters related to rigid motion (position, velocity and attitude).

This method allows eliminating the influences of flexibility from the estimation of rigid motion parameters. Unfortunately for the examined HAPD aircraft, this influence is not particular evident.

Problems related to load alleviation techniques have been also examined. Specifically, the advantages obtained using an estimation of the shape changes as feedback in a control loop, have been examined.

The proposed system, based on the association of the EKF for actual shape estimation with a proper control law, has highlighted the importance of a correct tuning of the EKF.

A different tuning could be required for the estimation of structural deflections caused by maneuvers or by gusts, because of the different frequency content of the solicitations. The dynamic behavior of the filter has a great influence on the performances of the control law.

The analyzed thematic has great possibility for future developments for both aeronautical and spatial structures but also for civil engineering structures (knowledge of shape changes is required, for example, to control the attitude of blades in wind turbines in order to improve the overall efficiency).

Analyzing the aeronautical field, the next step of this research activity might be the modeling of flexibility phenomena in ADGPS based on carrier phase measurements.

ADGPS already includes several antennas distributed along the aircraft for attitude determination.

Specifically, carrier phase measurements offer great accuracy, allowing application of GPS for estimation of both structural deflections and attitude (beyond position and speed). The possibility to use only GPS measurements or to include additional sensors shall be investigated.

There are some works in literature which concern ADGPS including a modeling of structural flexibility effects, but shape changes are just treated as a source of error to remove within the attitude estimation algorithm.

Another possible improvement consists in the estimation of mode shapes within the estimation filter together with the generalized coordinates.

In this research activity, mode shapes have been considered constant and exactly known. This improvement might provide greater accuracy and, above all, it would provide independency by the structural analyses. Such a kind of estimation algorithm could be used also for Structural Health monitoring, because it is possible to associate changes in mode shapes (which reflect changes in stiffness and mass distribution) with damages in the structure.

In conclusion, the products of the doctorate activity are:

1. an algorithm for estimation of shape-changes associated to estimation of navigation parameters, using navigation sensors;
2. an algorithm for estimation of only the shape-changes using measurements provided by a video-based system.

The innovative aspects covered in these two points are:

- a complete modeling of flexible motions into navigation algorithms;
- coupling between rigid motions and elastic ones;
- mode shapes derived by FEM analysis;
- 3-D modeling of elastic motions;
- GPS or a video-based setup for estimation of flexible motions for aerospace structures;
- application of a video-based system for real time estimation of shape-changes in aerospace applications.

Furthermore, the algorithm for estimation of shape-changes has been associated to a control law for Load Alleviation. This is also an innovative aspect, because these Load Alleviation

algorithms are generally based on the application of global measurements, which refer to rigid motions, as feedback.

Other activities have concerned the experimental determination, through lab-tests, of the error model parameters characterizing inertial sensors and a review of some unconventional navigation systems whose performances are influenced by structural flexibility.

Future developments of this research could include: i) the experimental validation of the proposed methods for mode-shapes estimation and load alleviation, using a suitable test rig (in this case other sensors architectures could be also investigated) and ii) the realization of a system able to estimate with great accuracy both the parameters related to rigid motions and to elastic ones for the guidance, navigation and control of aircrafts or spacecraft, as well as for Structural Health Monitoring.

6　References

[1]. Department of Defense, "Military Critical Technologies List", Aeronautics Technology, June 2009.

[2]. Composite Materials: Testing and Design, *ASTM, 2003*.

[3]. Guendel, "Unsteady aerodynamics for aeroelastic applications using the impulse response method", M.S. Thesis MTI 2000.

[4]. http://www.flightglobal.com/blogs/flightblogger/2008/05/a-closer-look-at-787-wingflex.html

[5]. EU project ACFA2020 http://www.acfa2020.eu/background.html

[6]. Aerospace America – December 2010 Vol.48, No. 11 – The year in review –

[7]. M. Lichter, S. Dubowzky et alii, "Shape, Motion, and Parameter Estimation of Flexible Space Structures using Laser Rangefinders", Robotics: Science and Systems, Cambridge, MA, June 8-11, 2005.

[8]. Amy Bilton, Yoshiyuki Ishijima, Matthew D. Lichter, Steven Dubowsky: Sensor architecture for the robotic control of large flexible space structures. J. Field Robotics 24(4): 297-310 (2007).

[9]. NASA SP 8036 "Effects of Structural Flexibility on Launch Vehicle Control System", February 1970.

[10]. D., McLean, "Automatic Flight Control System",Prentice Hall, 1990

[11]. T.Oertel, J.F.Wagner, "Integrated Motion Measurement for flexible Structures", *Technische Mechanik, band 27, Heft 2, (2007) 94-114.*

[12]. J.F.Wagner, G.Kasties, "Applying the principle of integrated navigation systems to estimating the motion of large vehicles", *Aerospace Science and Technology 2003*.

[13]. Robin L. Cravey, et alii , "Structurally Integrated Antenna Concepts for HALE UAV", NASA/TM-2006-214513.

[14]. Kee, C., Cho, A., Kim, J., No,, H., "1 Antenna, 3 Dimensions, GPS Flight Control in uAV Operations", InsideGNSS March/April 2010.

[15]. Jarrell, J., Gu, Y., Seanor, B., "Aircraft Attitude, position, and Velocity Determination Using Sensor Fusion", AIAA Guidance, Navigation and Control Conference and Exhibit, 18-21 August 2008, Honolulu, Hawaii.

[16]. Farrell, J.A, "Aided Navigation- Gps with High Rate Sensors", McGraw-Hill, 2008, ISBN 978-0-07-149329-1.

[17]. Lu, G., "Development of a GPS Multi-Antenna System for Attitude Determination", PhD Thesis, January 2005, University of Calgary (Alberta, Canada), Department of Geomatics Engineering, UCGE Reports Number 20073.

[18]. Garcia, J.G, Mercarder, P.I, Muravchik, C.H, "Use of GPS Carrier Phase Double Differences", Latin-American Applied Research, 2005, vol. 35, n. 2, pp. 115-120, ISSN 0327-0793.

[19]. Cannon, M.E., Sun, H., Owen, T.E., Meindl, M.A., "Assessment of a non-dedicated GPS receiver system for precise airborne attitude determination", Proceedings of National Technical Meeting, ION GPS 94, Salt Lake City, September 20-23 1994.

[20]. Cohen, C.E., Parkinson, B.W., McNally, B.W., "Flight Tests of Attitude Determination Using GPS Compared Against an Inertial Measurement Unit", Proceedings of National Technical Meeting, ION, 1993, pp. 579-587.

[21]. Sang, H.O., Seok, B.S. et alii, "Design of an Autonomous GPS/INS Navigation System for Guided Bomb with wing adapter kit", Proceedings of the 2004 International Symposium on GNSS/GPS, Sydney (Australia), 6-8 December 2004.

[22]. Wagner, Kasties, "Applying the principle of integrated navigation systems to estimating the motion of large vehicles", Aerospace Science and Technology 8 (2004), pp. 155-166.

[23]. Gebre-Egziabher, D., Hayward, R.C., Powell, J.D., "A Low-Cost GPS/Inertial Attitude Heading Reference System (AHRS) for General Aviation Applications", Proceedings of IEEE Position, Location, Navigation Symposium – PLANS 98, palm Springs, (CA), 1998, pp. 518-525.

[24]. Sturza,M., "Skewed axis inertial sensor geometry for optimal performance", AIAA/IEEE Digital Avionics Systems Conference, pp.128-135

[25]. Waegli, A., Guerrier, S., Skaloud, J., "Redundant MEMS-IMU integrated with GPS for Performance Assessment in Sports," IEEE/ION PLANS 2008, Monterey (CA), 2008, pp. 1260-1268

[26]. Colomina, I., Giménez, M., Rosales, J.J., et alii, "Redundant IMUS for precise trajectory determination", International Archives of Photogrammetry Remote Sensing and Spatial Information Sciences, 2004, Vol. 35, Part. 1, pp 159-1656, ISSN 1682-1750.

[27]. El-Sheimy, N., Niu, X., "The Promise of MEMS to the Navigation Community", InsideGNSS, March/April 2007, pp.46-56.

[28]. Goulart, P.J., "A dynamic based method for accelerometer only navigation of a spinning projectile", Master Science Thesis in Aeronautics and Astronautics, MIT, 2001.

[29]. Analog Devices, iMEMS Accelerometers ADXL 202/210, Technical Datasheet Rev.B, http://www.analog.com/static/imported-files/data_sheets/ADXL202_210.pdf

[30]. Chen, J.-H., Lee, S.-C., DeBra, D.,B., "Gyroscope Free Strapdown Inertial Measurement Unit by Six Linear Accelerometers", AIAA Journal of Guidance, Control and Dynamics, Vol.17, No.2, March-April 1994.

[31]. Hung, C-Y., Fang, C.-M., Lee, S.-C., "A Compensator to Advance Gyro-Free INS Precision", International Journal of Control, Automation, and Systems, vol.4, no. 3, pp.351-358 June 2006.

[32]. Vreeburg, J.P.B, "Analysis of the data from a distributed set of accelerometers, for reconstruction of set geometry and its rigid body motion", NLR, NLR-TP-98343, August 1999.

[33]. Hanson, R., "Using Multiple MEMS IMUs to form a Distributed Inertial Measurement Unit", Master's Thesis, Department of the Air Force Air University, Air Force Institute of Technology, AFIT/GE/ENG/05-06.

[34]. Tan, C.-W., Mostov, K., Varaiya, P., "Feasibility of A Gyroscope-free Inertial Navigation System for Tracking Rigid Body Motion", University of California, Berkley, California PATH Research Report UCB-ITS-PRR-2000-9, May 2000, ISSN 1055-1425.

[35]. Edwan, E., Knedlik, S., Zhang, M., Loffeld, O., "Investigation of dynamic models for angular motion estimation in a Gyro-free IMU", Proceedings of 16th Saint Petersburg International Conference on Integrated Navigation Systems, Saint Petersburg 2009.

[36]. Edwan, E., Knedlik, S., Loffeld, O., "An Extended Kalman Filter for Improving Angular Motion Knowledge in a Multiple Distributed IMU Set", proceedings of Symposium Gyro Technology 2008, Karlsruhe, 2008.

[37]. Qin, L., Zhang, W., Zhang, H., Xu, W., "Attitude Measurement system based on micro-silicon accelerometer array", Elsevier, Chaos, Solitons & Fractals, 29 (2006) 141-147.

[38]. Park, S.,Tan, C-W., "GPS-Aided Gyroscope-Free Inertial Navigation Systems", University of California, Berkley, California PATH Research Report UCB-ITS-PRR-2002-22, June 2002, ISSN 1055-1425

[39]. Bar Shalom et alii, "Estimation with Application to Tracking and Navigation", John Wiley & Sons INC., 2001.

[40]. Noll, Ishmael, Brown et alii, "Technical Findings, Lessons Learned, and Recommendations Resulting from the Helios Prototype Vehicle Mishap", NATO RTO, 2007.

[41]. E.H. Teague, J.P. How, B.W. Parkinson, "Control of Flexible Structures Using GPS: Methods and Experimental Results", Journal of Guidance, Control and Dynamics, Vol. 21, No. 5, September–October 1998.

[42]. G.W. Roberts, X. Meng, A. H. Dodson, "Structural dynamic and deflection monitoring using integrated GPS and Triaxial Accelerometers", Proceedings of ION GPS 2000, 19-22 September, Salt Lake City (UT) USA, pp. 59-68.

[43]. X. Li, C. Rizos et alii, "The complementary characteristics of GPS and accelerometer in monitoring structural deformation", U.S. Institute of Navigation National Tech. Meeting, San Diego, California, 24-26 January, pp. 911-920

[44]. X. Li, C. Rizos et alii, "Full-scale structural monitoring using an integrated GPS and accelerometer system", GPS Solution (2006) 10, pp. 233–247.

[45]. X. Li, "Integration of GPS, Accelerometer and Optical Fiber Sensors for structural deformation monitoring"

[46]. J. A. Behr, K. W. Hudnut, N. E. King, "Monitoring structural deformation at Pacoima Dam, California using GPS", Proceedings of the 11th International Technical Meeting of the Satellite Division of the Institute of Navigation [ION GPS-98; Nashville, TN], pp. 59-68, 1998

[47]. M.R. Kaloop, Hui Li, "Tower Bridge Movement Analysis with GPS and Accelerometer Techniques: Case Study Yonghe Tower Bridge", Information Technology Journal 2009, ISSN1812-5638.

[48]. J.Barnes, et alii, "Structural deformation using Locata", 1st FIG International Symposium on Engineering. University of Nottingham, United Kingdom, 28 June – 1 July 2004

[49]. P.Saltis, C. Ioannidis, "An Automatic Technique for accurate Non-Contact Structural Deformation Measurements", ISPRS Commission V Symposium 'Image Engineering and Vision Metrology', IAPRS Volume XXXVI, Part 5, Dresden 25-27 September 2006.

[50]. A. M. Wahbeh, J.P. Caffrey, S.F.Masri, "A Vision-Based Approach for the direct measurement of displacements in vibrating structures" in Smart Materials and Structures 12 (2003), Institute of Physics Publishing, pp. 785-794

[51]. A. M. Wahbeh, J.P. Caffrey, S.F.Masri, "Direct Measurement of displacements of vibrating structures through Vision-Based Approach" in Emirates Journal for Engineering Research, 9 (2) (2004), 105-110

[52]. J. Morlier, P. Salom, F. Bos, "New image processing tools for structural dynamic monitoring" in Key Engineering Materials (Volume 347) September 2007, Damage Assessment of Structures VII, pp. 239-244.

[53]. T.G.Ryall, C.S. Fraser, "Determination of Structural Modes of vibration using digital photogrammetry", AIAA Journal of Aircraft, Vol.39, No 1 January-February 2002

[54]. Lichter, Dubowsky, Ueno, Mitani, "Shape, Motion, and Parameter Estimation of Flexible Space Structures using Range Images", International Conference on Robotics and Automation, Barcelona, Spain, 2005.

[55]. D.N.C Tse, G.R. Heppler, "Shape Determination for large flexible satellite using stereo vision", AIAA Journal of Spacecraft and Rockets, Vol.2 9, No 1 January-February 1992

[56]. M. Smereka, I. Duleba, "Circular Object Detection Using a Modified Hough Transform", Int. Journal on Applied Mathematics and Computer Science, 2008, Vol. 18, No. 1, pp. 85–91.

[57]. W.C. Hu; "Adaptive Template Block-Based Block Matching for Object Tracking", Inter. Conf. on Intelligent Systems Design and Applications, ISDA 2008, Vol. 1, pp. 61-64.

[58]. S. Denman , C. Fookes , S. Sridharan, "Improved Simultaneous Computation of Motion Detection and Optical Flow for Object Tracking", Digital Image Computing: Techniques and Applications, DICTA 2009, pp. 175-182.

[59]. M. Manikandan, P. Vijayakumar, N. Ramadass, "Motion Estimation Method for Video Compression - an Overview", IFIP International Conference on Wireless and Optical Communications Networks, 2006.

[60]. B. P. Danowsky P. M. Thompson, "Incorporation of Feedback Control into a High-Fidelity Aeroservoelastic Fighter Aircraft Model" Journal of Aircraft Vol. 47, No. 4, July–August 2010

[61]. K. B. Lazarus, E.F. Crawley, C.Y. Lin, "Multivariable Active Lifting Surface Control Using Strain Actuation: Analytical and Experimental Results" Journal of Aircraft Vol. 34, No. 3, May – June 1997

[62]. Y. Matsuzaki, T. Ueda, Y. Miyazawa, H.Matsushitat "Gust Load Alleviation of a Transport-Type Wing: Test and Analysis" Journal of Aircraft Vol. 26, NO. 4

[63]. M. Karpel "Design for Active Flutter Suppression and Gust Alleviation Using State-Space Aeroelastic Modeling" Journal of Aircraft vol. 19, no. 3, march 1982

[64]. D. G. Wilson, D. E. Berg, D. W. Lobitz, J. R. Zayas "Optimized Active Aerodynamic Blade Control for Load Alleviation on Large Wind Turbines" Awea Windpower 2008 Conference & Exhibition, Houston, Texas, June 1-4, 2008

[65]. V. R. Baraniello, M. Cicala, F. Corraro, "An Extension of Integrated Navigation Algorithms to Estimate Elastic Motions of Very Flexible Aircrafts", 2010 IEEE Aerospace Conference, Big Sky Montana USA March 2010.

[66]. V. R. Baraniello, M. Cicala, L. Cicala, "An Algorithm for Real Time Estimation of the Flexible UAV Structural Motions using a Video-based system", Proceedings of 14th International Conference On Information Fusion, Chicago IL US, 5-9 July 2011.

[67]. B. L. Stevens and F. L. Lewis, "Aircraft Control and Simulation", John Wiley & Sons Inc.

[68]. Cicala M., Sollazzo A., CIRA CF 10-0538 "HAPD-Modello di Velivolo Flessibile orientato al controllo II versione".

[69]. Tecvol, Sensor Fusion Document , SISV department CIRA

[70]. Zhang X., Li Y, et alii "Allan Variance Analysis on Error Characters of MEMS Inertial Sensors for an FPGA-based GPS/INS System", International Symposium 2008 on GPS/GNSS.

[71]. Crossbow MicroNav Datasheet

[72]. F. Ham, R. Grover Brown, "Observability, Eigenvalues and Kalman Filtering", IEEE Transactions on Aerospace and Electronic Systems, Vol. AES-19, No. 2 march 1983